University of Windsor
Scholarship at UWindsor

Electronic Theses and Dissertations | Theses, Dissertations, and Major Papers

2002

Characterization of tribological behaviour of graphitic aluminum matrix composites, grey cast iron, and aluminum silicon alloys.

Ahmad Reza. Riahi
University of Windsor

Follow this and additional works at: https://scholar.uwindsor.ca/etd

Recommended Citation

Riahi, Ahmad Reza., "Characterization of tribological behaviour of graphitic aluminum matrix composites, grey cast iron, and aluminum silicon alloys." (2002). *Electronic Theses and Dissertations*. 1411.
https://scholar.uwindsor.ca/etd/1411

This online database contains the full-text of PhD dissertations and Masters' theses of University of Windsor students from 1954 forward. These documents are made available for personal study and research purposes only, in accordance with the Canadian Copyright Act and the Creative Commons license—CC BY-NC-ND (Attribution, Non-Commercial, No Derivative Works). Under this license, works must always be attributed to the copyright holder (original author), cannot be used for any commercial purposes, and may not be altered. Any other use would require the permission of the copyright holder. Students may inquire about withdrawing their dissertation and/or thesis from this database. For additional inquiries, please contact the repository administrator via email (scholarship@uwindsor.ca) or by telephone at 519-253-3000ext. 3208.

INFORMATION TO USERS

This manuscript has been reproduced from the microfilm master. UMI films the text directly from the original or copy submitted. Thus, some thesis and dissertation copies are in typewriter face, while others may be from any type of computer printer.

The quality of this reproduction is dependent upon the quality of the copy submitted. Broken or indistinct print, colored or poor quality illustrations and photographs, print bleedthrough, substandard margins, and improper alignment can adversely affect reproduction.

In the unlikely event that the author did not send UMI a complete manuscript and there are missing pages, these will be noted. Also, if unauthorized copyright material had to be removed, a note will indicate the deletion.

Oversize materials (e.g., maps, drawings, charts) are reproduced by sectioning the original, beginning at the upper left-hand corner and continuing from left to right in equal sections with small overlaps.

ProQuest Information and Learning
300 North Zeeb Road, Ann Arbor, MI 48106-1346 USA
800-521-0600

UMI®

CHARACTERIZATION OF TRIBOLOGICAL BEHAVIOUR OF GRAPHITIC ALUMINUM MATRIX COMPOSITES, GREY CAST IRON, AND ALUMINUM SILICON ALLOYS

BY

AHMAD REZA RIAHI

A DISSERTATION

SUBMITTED TO THE FACULTY OF GRADUATE STUDIES AND RESEARCH THROUGH THE ENGINEERING MATERIALS GRADUATE PROGRAM IN PARTIAL FULFILMENT OF THE REQUIREMENTS FOR THE DEGREE OF DOCTOR OF PHILOSOPHY AT THE UNIVERSITY OF WINDSOR

WINDSOR ONTARIO CANADA

2002

© 2002 REZA RIAHI

National Library of Canada
Acquisitions and Bibliographic Services
395 Wellington Street
Ottawa ON K1A 0N4
Canada

Bibliothèque nationale du Canada
Acquisitions et services bibliographiques
395, rue Wellington
Ottawa ON K1A 0N4
Canada

Your file Votre référence

Our file Notre référence

The author has granted a non-exclusive licence allowing the National Library of Canada to reproduce, loan, distribute or sell copies of this thesis in microform, paper or electronic formats.

L'auteur a accordé une licence non exclusive permettant à la Bibliothèque nationale du Canada de reproduire, prêter, distribuer ou vendre des copies de cette thèse sous la forme de microfiche/film, de reproduction sur papier ou sur format électronique.

The author retains ownership of the copyright in this thesis. Neither the thesis nor substantial extracts from it may be printed or otherwise reproduced without the author's permission.

L'auteur conserve la propriété du droit d'auteur qui protège cette thèse. Ni la thèse ni des extraits substantiels de celle-ci ne doivent être imprimés ou autrement reproduits sans son autorisation.

0-612-75730-7

Canada

ABSTRACT

In recent years a number of aluminum-silicon alloys and some graphitic aluminum matrix composites have been fabricated for potential tribological applications in the automotive industry, in particular for lightweight high efficiency internal combustion engines to replace conventional uses of cast iron.

This study provides a systematic investigation for wear mechanisms in dry sliding of the graphitic aluminum-matrix composites (A356 Al-10%SiC-4%Gr and A356 Al-5%Al_2O_3-3%Gr) developed for cylinder liner applications. Two eutectic Al-Si alloys (modified with rare earth elements) developed for wear resistant engine blocks were also studied. The tribological behavior of grey cast iron (ASTM A30), which is a traditional material for engine components, was also investigated as reference.

For graphitic aluminum matrix composites, a wear mapping approach has been adopted. Three main regimes: ultra mild, mild and severe wear regions were determined in the maps; additionally, a scuffing region was observed. In the ultra mild wear regime the wear resistance was primarily due to the hard particles supporting the load. It was shown that the onset of severe wear in graphitic composites occurred at considerably higher loads compared to A356 aluminum alloy and A356 Al-20% SiC composite. At the onset of severe wear, the surface temperatures and coefficient of friction of the graphitic composites was lower than that of A356 Al-20% SiC. At all testing conditions in the mild wear regime, a protective tribo-layer

was formed, which by increasing the speed and load became more continuous, more compact, smoother, and harder. The tribo-layers were removed at the onset of severe wear.

An experimental wear map of grey cast iron was constructed; it consisted of three wear regimes: ultra mild, mild and severe wear. In the ultra mild regime a compacted fine iron oxide powder formed on the contact. The onset of severe wear was started with local material transfer to the steel counterface, and continued by increasing the roughness of the counterface. In the mild wear regime the oxide layers on the contact surface controlled the wear. Because of the microstructure of grey cast iron, large size debris formed in the mild regimes, which could promote a transition from mild to severe wear at loading conditions close to the upper limit of the mild regime.

The effects of size and morphology of hard phases in eutectic Al-Si alloys on their scuffing and wear resistance was investigated using etching techniques. Scratch tests and sliding wear tests were performed on the Al-Si samples etched to different times. At low loads, the wear rates and scuffing resistance of Al-Si alloys were a strong function of the etching time, surface roughness before etching, and the morphology of the hard phases. In the etched condition, fracture of the hard phases from the roots of the protruded portions of particles caused scuffing; while fracture of the trailing edges of the hard phases controlled the wear rate of the Al-Si alloys.

To My Parents

Mohtaram and Fazlollah Riahi

And

To My Wife

Afsaneh Edrisy

ACKNOWLEDGMENTS

I would like to express my sincere gratitude to Dr. A. T. Alpas for his supervision, interest, encouragement and friendship. Dr. T. Perry is acknowledged for his comments and suggestions as the external examiner.

I would like to extend my thanks to Dr. J. Sokolowski, Dr. D. Watt and Dr. A. Sid-Ahmed for their help and encouragement; Mr. J. W. Robinson, Mr. P. Seguin and Mr. R. Tattersall for their technical assistance; and Mrs. B. L. Denomey for her administrative assistance during my graduate studies. I would like to thank the Technical Support Center of University of Windsor with special appreciation to Mr. Steve Budinsky and Mr. Mark Enns.

The financial support from an MMO-INCO Collaborative Research Grant is gratefully acknowledged. Receipt of an Ontario Graduate Scholarship was very much appreciated.

TABLE OF CONTENTS

CHAPTER 3

MATERIALS AND EXPERIMENTAL METHODS

CHAPTER 4

A356-Al- 10% SiC- 4%Gr AND A356 Al-5%Al_2O_3- 3%Gr COMPOSITES

LIST OF TABLES

LIST OF FIGURES

CHAPTER 1

INTRODUCTION

In recent years a number of aluminum matrix composites have been developed for potential tribological applications in automotive engines, in particular, for lightweight cylinder liners. One of the most important aspects of the tribological performance of cylinder liners, pistons and piston rings is their ability to resist seizure and scuffing during adverse engine running conditions such as lubricant starvation [1]. Wear losses suffered by the aluminum alloy liners during normal engine operation should be sufficiently low to prevent the increase in the clearance between the liner and piston rings that would reduce engine efficiency. Scuffing and seizure problems that may occur during oil starvation periods can be addressed by incorporating solid lubricants, namely graphite, in the composition of Al-Si alloys reinforced by SiC or Al_2O_3 particles [2-4]. The high seizure resistance of graphitic aluminum matrix composites has been attributed to the formation of graphite layers on the contact surfaces. These act as solid lubricants, which reduce metal-to-metal contact between the sliding pairs [3-7]. According to Ames and Alpas [8], under severe loading and sliding speed conditions, graphite served as a temporary safeguard by keeping the initial temperature rise low, therefore allowing the contact surfaces enough time to generate a hard compacted tribo-layer with smooth surface and sufficient thickness (more than 10 μm) to protect the material underneath from excessive subsurface damage. The tribo-layers in graphitic SiC reinforced aluminum matrix

composites consisted of graphite, fractured ceramic particles mixed with aluminum, and iron oxides transferred from the steel counterface.

Aluminum-silicon alloys are another group of materials that have received attention for applications such as engine blocks, engine cylinder heads, and other tribological applications where weight savings are important. Many investigations that have been conducted to identify the effects of silicon content and particle size on the wear and scuffing resistances of these alloys [9-16]. However, most of the investigations were under high loading conditions [17-20]. One of the tribological weaknesses of Al-Si alloys is their low scuffing resistance. It is expected that the size and morphology of silicon particles should affect the wear and scuffing resistance. Understanding the role of etching conditions and surface roughness on the wear and scuffing resistance of Al-Si alloys at low loads helps to identify the role of silicon morphologies in the wear of these alloys.

Grey cast iron is a cheap and readily available material. It is universally used for the manufacturing of piston rings and cylinder liners because of its good friction and wear characteristics. The combination of good mechanical properties and inexpensive manufacturing routes of grey cast iron are unique. The excellent wear resistance of grey cast iron in dry sliding at low loading conditions is attributed to the feeding of the contact surface by graphite flakes and the formation of a graphite film on the contact surface [21-23]. The occurrence of severe wear in cast iron at relatively low loading conditions, related to the graphitic microstructure of grey cast iron needs more investigation.

1.1. OBJECTIVES OF THE THESIS

The main objectives of this work are:

1. To determine the wear mechanisms in dry sliding of graphitic aluminum matrix composites against steel, using the wear map approach.
2. To identify the effects of morphology of hard phases on the tribological behavior of eutectic aluminum-silicon alloys at low loading conditions.
3. To identify the wear mechanisms in dry sliding of ASTM A30 gray cast iron and construct its experimental wear map for use as a reference material.

1.2. ORGANIZATION OF THE THESIS

This thesis is divided into 8 chapters. A literature review on the wear behaviour of the three types of materials investigated is given in Chapter 2. The details of the experimental methods are explained in Chapter 3. Chapter 4 describes the experimental results and includes a discussion of the results of two graphitic aluminum matrix composites, A356 Al- 10% SiC- 4% Gr and A356 Al- 5% Al_2O_3- 3% Gr. The results and the discussion of the experiments on grey cast iron are given in Chapter 5. The results and discussion of the experiments on Al-Si alloys are presented in Chapter 6. Chapter 7 is an overall discussion for all three types of materials investigated, and Chapter 8 is a summary and the conclusions of the thesis.

CHAPTER 2

LITERATURE REVIEW

2.1.METAL MATRIX COMPOSITES

Metal matrix composites, as are known today, have evolved over the past 30 years. The primary support for these composites has come from the aerospace industry for airframe and spacecraft structures. More recently, the automotive, electronic, and leisure industries have started to look seriously at working with these composites. Metal matrix composites can be classified into either continuous fiber composites or discontinuously reinforced composites. The reinforcements have been introduced into matrices of aluminum, magnesium, copper, titanium, titanium aluminides, nickel, nickel aluminides, nickel-based super-alloys, or various alloys of iron. The aluminum matrix composites are among those that have become widely available. Discontinuously reinforced composites have become the most commonly used to date [24].

2.1.1. Applications

Typical applications for aluminum matrix composites, which have received attention recently, have mainly been associated with the automotive industry where lightweight alternatives to steel and cast iron components have been sought. Examples are replacement of cast iron brake discs and internal combustion engine cylinder liners. In the latter application, hybrid composites containing both SiC and graphite particles in Al-

Si alloy matrices have proved to be successful candidate replacement materials, with advantageous low-load wear and overall seizure resistance [25].

2.1.2. Wear of Metal Matrix Composites

Cylinder liners, pistons, and piston rings have to be resistance to scuffing and seizure during lubricant starvation conditions [1]. The wear rate of liners during normal engine operation must be reasonably low to keep engine efficiency high. Scuffing and seizure problems can be improved by adding graphite to composites of Al-Si alloys reinforced by SiC or Al_2O_3 particles [2-4]. Addition of graphite flakes or particles to aluminum alloys increases their resistance to seizure in lubricated [5,6] and dry condition [8,11]. It is reported that the high seizure resistance of graphitic aluminum matrix composites is related to the formation of graphite layers on the contact surfaces, which reduce metal-to-metal contact between the sliding pairs [3-7]. Ames and Alpas [8], showed that under severe loading conditions, graphite served as a temporary safeguard by keeping the initial temperature rise low. This allowed the contact surfaces enough time to generate a hard compacted tribo-layer with a smooth surface and sufficient thickness (>10μm) to protect the material underneath from excessive subsurface damage.

2.1.2.1. Formation of Tribo-layers

The formation of tribo-layers has also been commonly observed in aluminum alloys without the graphite. Shivnath et. al. [27] observed a "mechanically-alloyed" tribo-layer, which was harder than the rest of the material, in dry sliding of hypoeutectic, eutectic, and hypereutectic Al-Si alloys against steel. Razavizadeh and Eyre [28, 29] indicated that this layer contained compacted aluminum oxide particles and was rich in

iron oxide from the counterface steel. Antonionu and Borland [30] observed the presence of a very fine mechanical mixture of Al, Si, and Fe particles in an Al-Si alloy. Tandon and Li [31] reported that iron-aluminum intermetallic phases were formed within the tribo-layers in an Al-Si alloy worn against M2 steel. Yen and Ishihara [32] investigated the effect of humidity on the friction and wear of an Al-Si eutectic alloy and Al-Si based graphitic composites. They reported that by increasing the relative humidity from 70% to 95% the wear rate of the Al-Si alloy decreased by two orders of magnitude due to the in-situ formation of a Fe_2O_3-rich film on the alloy surface.

Jiang et. al. [33] studied the dry sliding wear mechanism of a nickel alloy sliding against the same nickel alloy. They found that the transition from severe to mild wear occurred after a defined sliding distance, and was accompanied by the formation of a compacted layer (tribo-layer) on the contact surface. This layer was formed by transfer and back transfer, and mechanical mixing and compaction of debris. They reported that the transition from severe to mild regimes was more pronounced at elevated temperatures.

Heilmann et. al [34] reported that the material transfer and back transfer could occur several times and eventually produce wear debris. They suggested that the formation of debris could be a result of work-hardening.

Subramanian [35] studied dry sliding of an Al-12.3%Si alloy against a copper counterface at 0.1 m/s with pressures of above 1.0 MPa. He reported that a tribo-layer formed on the worn surfaces. This layer was formed from a mechanical mixture of the Al alloy and copper. He concluded that the tribo-layer formation was a function of loading condition.

Iwai et al. [36] studied an Al 2024 alloy reinforced with SiC_w (w indicates whiskers). He noticed that a tribo-layer was formed after a sliding distance of only 50 m (at 40 N and 0.1 m/s).

Antoniou et al. [37] studied dry sliding of an Al-Si alloy against AISI 4340 steel. They indicated that a finely dispersed amorphous iron oxide formed on the contact surfaces due to the oxidation of the steel counterface.

The formation of tribo-layers in graphitic aluminum matrix composites (e.g. A356 Al-10%SiC-4%Gr and A356 Al-5%Al_2O_3-3%Gr) needs to be studied in detail because they play an important role in controlling the wear transitions and the micro-mechanisms. An effective way to study and predict the formation and removal of tribo-layers and the wear behavior of materials is to develop wear mechanism maps.

2.1.3. Wear Maps

Wear maps help to classify wear information and show the relationship between the different wear processes in dry sliding situations. Wear mechanism maps were first developed by Welsh [38] in a simplified form for steel. Recent efforts at construction of wear maps have included that by Lim and Ashby [39] for steel in dry contact against itself, using the existing information from the literature.

Antoniou and Subramanian [40], developed a wear mechanism map for aluminium-silicon alloys by following the method of Lim and Ashby [39]. They identified the wear mechanisms by direct observation of the worn surfaces of the aluminium alloy samples, the steel counterface, and the wear debris morphology.

Wang et. al. [41] constructed a wear mechanism map for dry sliding of an Al 6061 alloy reinforced with 20% SiC_w. They concluded that a transition from mild to severe wear, and ultimately seizure, occurred by increasing the loading condition. In the mild wear regime the worn surface was relatively smooth and the wear debris was small and brittle; they suggested that oxidation of aluminium was important in this process. In the severe wear regime a delamination wear process was reported.

Liu et. al. [42] constructed a qualitative wear mechanism map for Al alloys using wear data collected from the literature. Reasonable agreement was obtained between observed wear mechanisms and semi-empirical predictions based on Lim and Ashby's equations [39]. Rohatgi et. al. [43] were also involved in constructing wear maps of Al alloys containing various solid lubricant particles such as graphite and hard particles such as zircon.

Another wear map approach was adopted by Kato et al. [44] involving pin on disc wear experiments over a wide variety of loads and speeds for untreated and gas nitrided steel. The characterization of the wear debris produced during tests was used as the primary means for distinguishing between mild and severe wear regimes on load versus speed axes. It was found that gas nitriding not only reduced the steel wear rate, but also expanded the mild wear region toward higher loads and sliding speeds.

Zhang and Alpas [45] studied the wear behavior of a wrought aluminum alloy (6061) as a function of applied load and sliding velocity. They also developed an empirical wear transition map based on load versus sliding speed axes for this aluminum alloy, Al6061 sliding against SAE 52100 steel [45]. The role of the experimentally determined contact surface temperature on the wear transition was studied using

thermocouple probes positioned on the sliding specimens. It was observed that the transition from mild to severe wear arose when the bulk surface temperature T_b exceeded a critical temperature of 123°C, thus providing a practical means by which the onset of severe wear for a given tribo-system can be predicted, using a single bulk temperature measurement for Al alloys sliding against steel.

Wilson and Alpas [46] adopted a similar wear mapping approach whereby the effects of applied load and velocity on the wear behavior of an A356 Al alloy and A356 Al- 20% SiC composite were examined. Contact temperature measurements were also presented in map form and compared with observed wear transitions. The role of SiC particle addition on the wear behavior of A356 Al was discussed. They also researched using a temperature criterion to explain the transition to severe wear [46]. They used experimentally determined load and sliding speed criteria to calculate the critical transition temperature for severe wear in A356 Al by assuming a direct relationship between asperity contact size and debris particle diameter.

Recently, Edrisy et al. [47] constructed the wear map of a plasma transferred wire arc low carbon steel thermal spray coated onto an aluminum alloy in a controlled atmosphere. They depicted four main regimes which were mainly controlled by oxidation at high sliding speeds, and by plastic deformation and fragmentation of iron splats at low loading conditions.

2.1.4. Scuffing

Scuffing is local damage on the contact surface and defined differently by different researchers. Some researchers defined scuffed surfaces as those that were involved in sudden failure and others described them as having grooves, marks of

transferred material, transferred particles and other physical features [45]. A more general definition of scuffing given by Ludema [48] is as follows:

> "A roughening of surfaces by plastic flow whether or not there is material loss or transfer"

In this thesis scuffing is defined as local damage to the sliding surfaces either as a result of material transfer or as a result of scratching.

Of the several known mechanisms of wear, scuffing is among the least understood. Scuffing has been observed in gears, between cams and tappets, and between piston rings and cylinders [49, 50]. It can occur on cold or hot surfaces (cold scuffing and hot scuffing respectively). In the case of piston rings and cylinder liners, scuffing resistance is a function of surface roughness of the cylinder and the materials involved [51, 52].

2.2.ALUMINUM-SILICON ALLOYS

Ever since Al-Si alloys were recognized as tribo-materials in the automotive industry, numerous investigations have been conducted to find out the effects of silicon content and particle size on the wear and scuffing resistance of these alloys [9-16]. However, almost all of these investigations were under loading conditions that were governed by the transition from mild to severe wear [17-20]. Under these high loading conditions the conclusions were that the wear resistance of Al-Si alloys was either not a function of, or at best, a weak function of, the silicon content of the alloy [10, 11, 13 and 53]. Others found the opposite, that it is a function of the silicon content, and in some cases a eutectic composition gave the best wear resistance [12, 16,14, 18 and 53], and in other cases a hyper-eutectic composition gave the best performance [54 - 55]. One of the tribological weaknesses of Al-Si alloys is that they suffer from scuffing during oil

starvation periods. Many authors have studied scuffing under starved lubrication conditions [48, 56-58]; others have investigated scuffing under dry sliding conditions [59-61]. It is expected that the size and morphology of silicon particles should affect the wear and scuffing resistance. Understanding the role of etching conditions and surface roughness on the wear and scuffing resistance of Al-Si alloys at low loads helps to identify the role of silicon morphologies in the wear of these alloys. There is little work about either the role of etching or surface roughness prior to wear tests, or the effect of morphology of the hard phases, on the scuffing and wear resistance of these alloys [62].

2.3. CAST IRON

The relationship between the microstructure and wear behavior of grey cast iron is well established [63]. The excellent wear resistance of grey cast iron in dry sliding at low loading conditions is attributed to the feeding of the contact surface by graphite flakes and formation of a graphite film on the contact surface [21-23]. It is a general belief that a pearlitic structure matrix and an ASTM A type graphite flake provides the optimum wear resistance for grey cast iron [1, 64 and 65].

There has been extensive work on preparing wear maps of steel [39, 44] and new tribological materials such as MMCs and Al-Si alloys [42, 43 and 46], but there is no published wear map for the oldest and cheapest traditional wear resistant material, cast iron. This may be because the optimum tribological conditions for cast iron have been found experimentally during a century of use. But for new applications, or for improving performance, having a wear map is beneficial.

The dry sliding wear of cast iron has been investigated over a wide range of loading conditions. A mild oxidation regime and a severe metallic wear regime were identified

[21, 68-71]. In these studies the mild wear was attributed to graphite film formation [21-23]. Formation of a film that is a mixture of graphite and various forms of iron oxide was also reported [22, 66].

Several researchers related the occurrence of severe wear to the closing of the graphite flakes openings on the contact surface in grey cast iron [21, 23, 65, 67 and 68]. It was reported that the material removal mechanism at low sliding velocity in the severe wear regime is related to either localized fracture at heavily deformed surface layers, or to linkage of cracks in the subsurface undeformed material [69]. The effect of sliding distance at constant loading condition in the transition from mild to severe wear was investigated recently by Lathabai [70].

The literature survey given above shows that extensive work has been done on identification of the dry sliding wear mechanisms of aluminum matrix composites. However, there are still some important topics that have not received close attention: the formation of tribo-layers in the mild wear regime; their role in controlling the wear process; the occurrence of scuffing on the steel counterface because of the presence of the tribo-layers; and finally, removal of tribo-layers at high loads and sliding speeds leading to severe wear. These are among the subjects that need to be studied. The work reported in this thesis aims to shed light on these poorly understood aspects of the wear mechanisms, and to characterize the tribological behavior of these materials more accurately.

This present thesis focuses on the formation of tribo-layers in graphitic aluminum matrix composites, A356 Al-10%SiC-4%Gr and A356 Al-5%Al_2O_3-3%Gr. The wear mechanisms at different loads and velocities were identified and these were plotted in a

wear map format. The formation of tribo-layers and their roles in controlling the wear transitions in the graphitic composites were then discussed in detail.

The role of etching conditions, and surface roughness, on the wear and scuffing resistance of Al-Si alloys at low loads have also been studied in detail and the role of silicon morphologies on the wear of these alloys were investigated.

CHAPTER 3

MATERIALS AND EXPERIMENTAL METHODS

3.1. GRAPHITIC ALUMINUM MATRIX COMPOSITES

Dry sliding wear tests were performed on samples made of an A356 Al-10%SiC-4%Gr composite (commercial name GrANi® 10S:4G) and an A356 Al-5%Al_2O_3-3%Gr composite (commercial name GrANi® 5A:3G). The nominal composition of the A356 Al, which was the matrix alloy for both composites, (in wt pct) was 7 % Si, 0.2 % Mg, 0.11 %Fe, 0.2 %Ti, 0.05 % Mn, 0.05 % Zn, and the balance aluminum. The composites were produced using a molten metal mixing technique (INCO Ltd., ON, Canada). To improve surface wetting during casting the graphite particles were coated with nickel [71]. The microstructures of the A356 Al-10%SiC-4%Gr and A356 Al-5%Al_2O_3-3%Gr composites shown in Figs. 3.1.a and 3.1.b are similar and contain coarse graphite nodules of about 150 μm diameter. The size of the reinforcing ceramic particles, SiC or Al_2O_3, is around 17 μm. The composites also contain about 3 % volume of an intermetallic Al_3Ni phase with a script morphology. These are formed as a result of the reaction between the nickel coating around the graphite particles and the molten aluminum. The details of the microstructural features of the composites are given in Table 3.1(a), and their physical and mechanical properties are listed in Table 3.1(b).

Wear tests were performed using a block-on-ring type wear machine within a load range of 0.4 - 420.0 N and a sliding velocity range of 0.2 - 3.0 m/s. The samples were

machined from the "as received" cast liners into rectangular blocks of 5 mm × 10 mm × 10 mm dimensions. The counterface ring was made of SAE (AISI) 52100 type bearing steel and had an outer diameter of 38 mm. The sliding distance for each test was normally 6000 m for all sliding speeds and loads. The exception was for severe wear conditions where the total sliding distance was limited by the onset of seizure. The mass of each specimen was measured before and after each wear test (with an accuracy of 0.1 mg) and the mass difference was divided by the sliding distance to calculate the wear rate. Mass based wear rates were converted to volumetric wear rates using the density of each material.

The bulk temperature (the temperature 5mm below the contact surface) of each specimen was measured using a commercial chromel-alumel (K type) thermocouple probe with a stainless steel sheath of 0.5 mm outer diameter. The details of the temperature measurement technique are given in reference [45].

The mechanical properties of the composites were determined by performing uniaxial tensile and compression tests using an Instron universal testing machine according to ASTM standards ASTM E 8M-99 [72] and ASTM E209-65 [73] respectively.

3.2. GREY CAST IRON

Dry sliding wear tests were performed on samples made of grey cast iron (ASTM 30). The microstructure of the grey cast iron is shown in Fig. 3.2. The gray cast iron has a pearlitic matrix with average length of 45 μm for graphite flakes and an average distance of 9 μm between graphite flakes. The physical and mechanical properties of the grey cast iron are listed in Table 3.2.

Wear tests were performed using a block-on-ring type wear machine within a load range of 0.4 - 100 N and a sliding velocity range of 0.2 - 3.0 m/s. The samples were machined from the as received cast iron cylinder liners into rectangular blocks of 10 mm × 10 mm × 5 mm dimension. The counterface ring was made of SAE (AISI) 52100 type bearing steel and had an outer diameter of 38 mm. The sliding distance for each test was 4000 m for all sliding speeds and loads, except for the severe wear conditions where the total sliding distance was limited by the onset of catastrophic wear. The mass of each specimen was measured before and after each wear test (with an accuracy of 0.1 mg) and the mass difference was divided by the sliding distance to calculate the wear rate. Mass based wear rates were converted to volumetric wear rates using the density of the material.

The bulk temperature (the temperature 5mm below the contact surface) of the specimen was measured using a commercial chromel-alumel (K type) thermocouple probe with a stainless steel sheath of 0.5 mm outer diameter. The temperature measurement was the same as those described in Section 3.1.

A scanning electron microscope (JEOL LV5800) equipped with energy dispersion spectroscopy (EDS), and an x-ray diffraction system with a Cu tube were used to characterize compositions and morphologies of the worn surfaces, and also the cross sections below the worn surfaces, and the loose debris particles generated during sliding wear of grey cast iron and the graphitic aluminum composites discussed in Section 3.1.

3.3. ALUMINUM-SILICON ALLOYS

3.3.1. Materials

The two eutectic Al-Si alloys with different additives were cast by the GM Research and Development Centre and subsequently cut to coupon size using a wire EDM machine. The alloys were designated as A and B and their compositions are given in Table 3.3. The microstructures of the alloys are shown in Figs. 3.3.a, 3.3.b. The microstructure of Al-Si alloy A (Fig. 3.3.a) contains a silicon phase (dark grey), an $Al_{15}(Mn,Fe)_3Si_2$ phase (rounded grey phase), an Al_3FeSi phase elongated grey phase, and rare earth metal rich phases (light phase). Alloy B has a microstructure (Fig. 3.3.b) containing the same phases as alloy A but the phases have acicular morphology. It also contains a small volume fraction of Mg_2Si phase (small size black phase). The approximate volume fraction of the major phases ($Al_{15}(Fe,Mn)_3Si_2$ and Si), and their average thickness and aspect ratios are presented in Table 3.4. Figs. 3.4.a, and 3.4.b, illustrate the distribution length of the major phases ($Al_{15}(Fe,Mn)_3Si_2$ and Si) in alloys A and B respectively. Comparing these figures show that alloy B has a higher volume fraction of long major phases than alloy A. The micro-hardness of the different phases of the alloys at a 25g load is summarized in Table 3.5. This table indicates that the matrix hardnesses of the two alloys are very close to each other. The densities for the alloys, measured according to ASTM Standard C127-88 [74], were also very close to each other and equal to 2.75 ± 0.05.

Wear tests were performed using a pin-on-disc configuration at 5 N and 0.5 m/s. The aluminum alloy samples tested were in the form of square coupons with dimensions 25 mm × 25 mm × 5 mm.

The material for the counterface pin for the wear tests was AISI type M2 high-speed steel with the following composition in weight percent: 0.8 C, 4.0 Cr, 5.0 Mo, 6.0 W, 2.0 V and the balance Fe. The diameter of the pin was 5.0 mm and the length 25 mm.

3.3.2. Sample Preparation

In order to investigate the effect of etching on wear behavior of the two Al-Si alloys, two different etching solutions were applied to samples polished at various conditions: (1) 10%NaOH to remove thin layers of matrix alloy (shallow etching) and investigate the effect of microstructure morphology on scuffing resistance of the alloys and (2) 50%HCl to remove thick layers of the matrix alloy (dip etching) and investigate the effect of microstructure morphology on the wear rate of the alloys.

3.3.2.1. Etching with 10%NaOH Solution

The scuffing resistance of the Al-Si alloys was sensitive to the roughness of the sliding surface before etching. The 25 mm × 25 mm faces of samples of alloy A and alloy B were ground according to the schedule in Table 3.6. Six samples from each alloy were ground each to a different surface finishes. These were etched by 10%NaOH solution for 7 minutes. An average roughness of R_a = 1.2 μm was obtained as a result of grinding by 240-grit silicon carbide paper, R_a = 1.7 μm by 180-grit, R_a = 1.2 μm by 240-grit, R_a = 0.7 μm by 320-grit, R_a = 0.4 μm by 400-grit, R_a = 0.25 μm by 600-grit silicon carbide paper, and R_a = 0.14 μm was obtained as a result of polishing by 1 μm Al_2O_3 suspension. Scuffing tests were performed to determine the surface roughness that gave the maximum scuffing resistance. Samples with an average roughness of R_a = 0.4 μm presented the highest scuffing resistance and were selected for detailed studies on which further etching

work was performed. A stylus surface profilometer was used to measure the roughness of samples.

Samples that were polished to an average roughness R_a = 0.4 μm, were then etched by a 10% NaOH solution for 1, 4, 7 and 9 minutes at room temperature. After etching, the samples were ultrasonically cleaned in distilled water and then ethanol respectively for 5 minutes each. Fig. 3.5 shows the variation of the roughness of the etched faces of the samples as a function of the etching time.

3.3.2.2.Etching with 50% HCl Solution

In the experiments on etching with 50% HCl solution the 25 mm×25 mm faces of the aluminum alloy samples were ground with 180, 240, 320, 400 and 600-grit silicon carbide paper until the marks caused by the previous grinding were removed. The samples were then polished on a polishing cloth impregnated with 1μm Al_2O_3 suspension. Immediately after polishing, the samples were ultrasonically cleaned in ethanol. Finally, the polished faces were etched by a 50% HCl solution for 30 seconds. If the etching process was started a long time after polishing, a thin passive oxide layer was formed on the polished surface. Consequently, a severe pitting corrosion occurred instead of relatively uniform dissolving of the matrix alloy, which was the intended result.

The etched surface of the sample was lightly rubbed against a clean cotton cloth to remove the majority of the loose particles. Finally, the samples were ultrasonically cleaned in distilled water and ethanol respectively for 5 minutes each and dried.

The same polishing procedure was followed for SEM investigations of the effect of etching time (by 10% NaOH solution) on the surface morphology of the Al-Si alloys.

3.3.2.3. Micro-hardness Measurements

The overall hardness of the Al-Si alloys was calculated by averaging 10 Vickers micro hardness indentations made on the polished (to 0.14 μm) surface of the samples using a normal load of 500 g. The hardness determined in this way was 74.4 ± 1 $kg.mm^{-2}$ for A and 85 ± 5 $kg.mm^{-2}$ for B. The micro-hardness of individual phases and matrix in each alloy was measured using a load of 25 g. In cases where the constituents were cracked, the lengths of the cracks were measured using a SEM in order to calculate their fracture toughness, K_{Ic}. The hardness and fracture toughness of a piece of pure silicon was also measured as a reference.

The hardness of the counterface pin material, AISI M2 high-speed steel, was measured using a load of 500 g, giving a value of 910 ± 5 $kg.mm^{-2}$. Again, this hardness value was the average of 10 measurements.

3.3.2.4. Scratch Tests

Scratch tests were performed on etched samples to observe the resistance of the hard phases to deformation and fracture during single pass sliding indentation motion. These tests were performed on the etched (by 10% NaOH solution) samples using a Vickers diamond indenter with the edge in front. The etched scratch test sample surfaces were prepared by the procedure described in Section 3.3.2.1. Tests were performed under normal loads of 5g, 10g and 25g. During the scratch test the sample stage of the scratch tester was moved linearly at a constant speed of 0.106 mm/s and a data logger recorded the friction force.

3.3.2.5. Wear Rate Measurements

Wear tests were performed on the Al-Si alloy specimens using a pin-on-disc sliding wear machine (Fig. 3.6). The apparatus is comprised of a variable speed rotating

shaft arrangement to which a steel sample holder is attached. A vertical loading system attached to the pin counterface is lowered onto the rotating Al-Si samples to produce a circular wear track of 16 mm average diameter and 5 mm in width.

The wear tests were run up to a constant sliding distance of 5000 m, unless scuffing happened (in the case of caustic etched samples), whereby the test was ended as soon as scuffing started. In this thesis scuffing is defined as local damage to the sliding surfaces either by material transfer or by scratch. Prior to wear testing both the pin and the Al-Si samples were ultrasonically cleaned in acetone, dried, and weighed to $\pm$0.0001 g using an electronic balance. After each test the specimens were cleaned of loose debris using ethanol and after drying weighed to determine the amount of mass change during wear. No lubricant was introduced prior to or during the wear test. The wear rates of the Al-Si alloys were obtained by dividing the mass change due to wear by the total sliding distance of 5000 m. Then, using the density of the material the wear rates were normalized to volumetric wear rates. Since the loading conditions were relatively low (0.5 m/s and 5 N), the temperature rise due to friction was not considered.

CHAPTER 4

A356 Al-10%SiC-4%Gr AND A356 Al-5%Al_2O_3-3%Gr COMPOSITES

4.1.EXPERIMENTAL RESULTS

4.1.1. Wear Regimes and Wear Maps

The wear rate versus load curves at various sliding speeds for the A356 Al-10%SiC-4%Gr composite are shown in Fig. 4.1.a. The wear rates were low and increased slightly with load in the mild wear regime. However a significant increase in the wear rates is noted at high loads where a transition to severe wear occurred for all sliding velocities, except for the lowest test speed of 0.5 m/s. The volume-loss based wear rates underestimate the severity of wear at high loads because heavy plastic deformation of the surfaces and extrusion of the deformed material accounted for most of the damage.

The A356 Al-5%Al_2O_3-3%Gr composite samples show similar wear behaviour. The wear rate vs. load curves for this composite are given in Fig. 4.1.b. The mild wear regime extended over a wide range of loads (5 N to 420 N) and sliding speeds (0.2 m/s to 3.0 m/s) for both composites. In both composites tribo-layers were formed on the contact surfaces during sliding in the mild wear region, as will be discussed in Section 4.2. Tribo-layers are hard layers comprised of broken hard particles and phases within the composite mixed with iron oxide from the steel counterface, compacted on the contact surface. The transition between mild and severe wear coincided with the removal of these tribo-layers.

Figs. 4.1.a and 4.1.b also show that at very low loads and speeds the wear rates decreased by an order of magnitude, revealing that another wear regime i.e., an ultra mild wear regime, existed. The transition loads and velocities between these three wear regimes; namely severe wear, mild wear, and ultra mild wear were determined by visual observations of the changes in the worn surface morphologies. More specifically, by observing formation and removal of tribo-layers during the wear tests. The microstructural and compositional changes of the worn surfaces and the debris that took place during wear transitions were later confirmed by the SEM, EDS, and XRD examinations.

The measured wear rates and the dominant wear mechanisms operating in each wear regime were summarized in a map form with log load versus log sliding speed axes. Figs. 4.2.a and 4.2.b show the wear maps constructed for the A356 Al-10%SiC-4%Gr and the A356 Al-5%Al_2O_3-3%Gr samples respectively. The three major wear regimes, namely, ultra mild, mild and severe wear regimes are depicted on each map. The same wear regimes were previously observed in the non-graphitic aluminum matrix composites [46]. The maps also showed a sub-regime of scuffing, which manifested itself as damage inflicted to the counterface by the tribo-layers. Many features of the wear maps of these two composites are similar: The location of transition boundaries and the wear rates in each regime are comparable. However, the transition to severe wear occurs at higher loads and speeds in the SiC reinforced composite by compared to the Al_2O_3 containing composite. The transition to the severe wear in the A356 Al-10%SiC-4%Gr occurs at 320 N for the tests at 0.8 m/s, 260 N at 1.2 m/s, 220 N at 2.0 m/s and 120 N at 3.0 m/s. For the

A356 Al-5%Al_2O_3-3%Gr transition loads are 300 N at 0.8 m/s, 200 N, 1.2 m/s, 150 N at 2 m/s and 100 N at 3.0 m/s.

The wear maps indicated that the wear rates for A356 Al-10%SiC-4%Gr composite in the ultra mild regime ranged between 1×10^{-7} and 9×10^{-6} mm^3/m (see the plot in the insert of Fig. 4.1.a). In the mild wear regime, the wear rates were an order of magnitude higher, i.e., in the range of 1×10^{-5} to 27×10^{-3} mm^3/m. In the severe wear regime the wear rates could be as much as five times greater than those in the mild wear regime (130×10^{-3} mm^3/m to 158×10^{-3} mm^3/m). In the severe wear regime, wear rates were not only high but also show a drastic increase with the sliding distance; shortly after the removal of the tribo-layers the composites seize against the steel counterface. The observations made above were also valid for the A356 Al-5%Al_2O_3-3%Gr except that the wear rates were about one order of magnitude higher in the ultra mild regime, and at sliding speeds above 1.2 m/s the severe wear occurred at loads 30% lower than those of the A356 Al-10%SiC-4%Gr.

4.1.2. Quantitative Analysis of the Properties of Tribo-layers

As shown in Figures. 4.3.a, the area of the wear track covered by the tribo-layer in the A356 Al-10%SiC-4%Gr composite increased with the load and the sliding speed. In the A356 Al-10%SiC-4%Gr composite, at 10 N and 0.5 m/s, 40% of the worn surface was covered with tribo-layers (in the case of A356 Al-5%Al_2O_3-3%Gr it was 35%). The worn surfaces of both composites were entirely covered by the tribo-layers at 10 N and 2.0 m/s. Quantitative analyses were performed at other loads and speeds. As a result of

these analyses, a diagram which shows the percentage of the total worn area covered by the tribo-layers as a function of these two variables has been constructed (Fig. 4.3.a).

The average thickness of the tribo-layers is a function of the load and speed also. The increase in the average thickness of tribo-layers in the A356 Al-10%SiC-4%Gr with the applied load at a speed of 0.8 m/s is shown in Fig. 4.3.b.

The hardness of the tribo-layers increased with load and sliding speed (Fig. 4.3.c); even when the applied load and the sliding speed were low (just above the ultra-mild to mild wear boundary) the average micro-hardness of tribo-layers was considerably higher than that of the bulk material (e.g. HV_{1000g} = 83 kg/mm^2 for A356 Al-10%SiC-4%Gr). In A356 Al-10%SiC-4%Gr the hardness of the tribo-layer was 380 kg/mm^2 at 10 N and 2.0 m/s and was 350 kg/mm^2 for A356 Al-5%Al_2O_3-3%Gr. By increasing the applied load to 275 N at the same speed the hardness of the tribo-layer reached 780 kg/mm^2 and 750 kg/mm^2 for A356 Al-10%SiC-4%Gr and A356 Al-5%Al_2O_3-3%Gr respectively.

The concentration of iron oxide within the top 10% of the thickness of the tribo-layer (measured using EDS) increased by increasing the load and the sliding speed (Fig. 4.3.d), but the rate of increase was higher at high loading conditions.

4.2.DISCUSSION

4.2.1. Formation and Removal of Tribo-layers

Fig. 4.4 shows the surface morphologies of the A356 Al-10%SiC-4%Gr composite in the three wear regimes. In the ultra mild wear regime, the worn surfaces of the A356 Al-10%SiC-4%Gr (as well as those of A356 Al-5%Al_2O_3-3%Gr composites) were covered by continuous layers of reddish iron oxide, possibly $Fe_2O_3.H_2O$ (Fig. 4.4.a). The steel

counterface ring in sliding contact with A356 Al-10%SiC-4%Gr exhibited long parallel grooves (Fig. 4.5) indicative of the abrasive effect of the SiC particles in the composite. Zhang and Alpas [75] have shown that ultra mild wear in metal matrix composites is due to the load supporting effect of the ceramic reinforcing particles at very low loads. Similar wear processes were observed in the ultra mild wear regimes of the A356 Al-5%Al_2O_3-3%Gr composite and non graphitic Al-Al_2O_3 and Al-SiC composites [46, 75], implying that the graphite does not play a significant role in this regime. There is no significant difference between the wear rates (nor the transition loads to mild wear) of the graphitic and non-graphitic versions of the A356-SiC composites [46].

The reason that graphite does not play a significant role in the ultra mild wear regime can be explained as follows: As mentioned above, SiC particles (and Al_2O_3 particles in the case of A356 Al-5%Al_2O_3-3%Gr) are the load supporting constituents. These hard particles are in contact with the counterface, and scratch the steel counterface and produce iron oxide rich debris particles (0.5 to 1.5 μm in diameter). The ratio of surface area to volume of the debris is very high (>5 m^2/m^3), so that it is immediately oxidized. The oxidized debris fills the areas between the protruded ceramic particles and in some areas it becomes compacted. Therefore, there is no chance for graphite to become exposed to the counterface, and the behaviour is the same for graphitic and non-graphitic composites.

The mild wear rates in both A356 Al-10%SiC-4%Gr and A356 Al-5%Al_2O_3-3%Gr were primarily controlled by formation of the tribo-layers, which are mechanically mixed layers of oxide on the contact surfaces (Figs 4.4.b and 4.4.c). The tribo-layers contained fractured SiC, $NiAl_3$, and Si particles mixed with aluminum oxide and iron oxide debris from the counterface. The top surfaces of the tribo-layers were covered with the iron

oxide films (Fig. 4.6.a and 4.6.b). Mechanically mixed and oxidized tribo-layers were formed as soon as the transition to mild wear was realized. However, when the applied loads and sliding velocities were modest, the tribo-layers were thin (about 5 μm) and not continuous throughout the wear tracks as shown in Fig. 4.4.b, (which is a A356 Al-10%SiC-4%Gr sample tested at 0.5 m/s and 10 N). Under these conditions, approximately 40% of the contact area was covered with the tribo-layers. Increasing the sliding speed and the load increased the proportion of the contact surface area covered by the tribo-layers. For example, at a sliding speed of 2 m/s and a load of 150 N, for the same material, the wear track was entirely covered by the tribo-layers with smooth surfaces (Fig. 4.3.c). In the severe wear regime, the tribo-layers were removed from the contact surfaces. Fig. 4.4.d shows the severe deformation at the worn surface of A356 Al-10%SiC-4%Gr at 300 N and 2.0 m/s.

Although a layer of compacted oxide powder covered the contact surface in the ultra mild wear regime, it isn't an actual load supporting area like the tribo-layers in the mild wear regime. Therefore the compacted oxide layer in the ultra mild wear regime is not considered a tribo-layer.

4.2.2. Microstructures of Tribo-layers

Tribo-layers on the surfaces of the A356 Al-10%SiC-4%Gr composites included fragments of fractured SiC particles (Al_2O_3 in the case of A356 Al-5%Al_2O_3-3%Gr) and $NiAl_3$ intermetallic particles mixed with iron and aluminum oxides as shown in Fig. 4.7. This micrograph is a cross sectional SEM back-scattered image of a typical tribo-layer. The mechanically mixed tribo-layer was quite thick and had an average dimension of about 50 μm in this section. Two important microstructural features of the tribo-layers in

graphitic composites, beside the comminuted (fractured and fragmented) ceramic and intermetallic particles were:

i) iron oxide layers at the contact surfaces and

ii) graphite films within the tribo-layers.

Iron oxide layers at the contact surfaces were formed as a result of the transfer of iron from the counterface. An iron oxide layer was always present on the top surface of the tribo-layer, but its thickness was non-uniform, and the concentration of the oxide usually decreased when moving away from the surface. At low loads and speeds oxide layers as thin as 0.5 μm form, but could reach a uniform thickness of 4-5 μm at high loads and speeds, Fig. 4.6.a. Fig. 4.6.b shows the EDS spectrum of the iron oxide layer.

The formation of lamellar graphite veins within the tribo-layers was another distinct microstructural aspect of the tribo-layers in worn A356 Al-10%SiC-4%Gr and A356 Al-5%Al_2O_3-3%Gr composites. The morphology of the graphite layers can be seen in Fig. 4.8.a. As shown in this micrograph, the graphite layers appear to have been formed as a result of shearing of graphite nodules located just below the contact surfaces. The graphite layers were typically formed at depths of 20-100 μm, where the magnitude of subsurface strains was extremely high [76], and were of the order of 2-11 (Fig. 4.8.a). The films "squeezed out" of the graphite nodules elongated in the direction of shear by enormous distances, normally 0.5-1.0 mm, as shown in Fig. 4.8.a. A high magnification micrograph of the tribo-layer is given in Fig. 4.8.b. This shows a lamellar structure formed by several graphite layers running parallel to each other, at a depth of about 40-60 μm below the contact surface. The typical thickness of a graphite film was 1-5 μm

(Fig. 4.8.b). It can be suggested that these graphite layers reduce the shear stresses transferred to the bulk material underneath the tribo-layer. They usually demarcate the boundary between highly deformed tribo-layers and relatively damage free bulk material beneath them. On the other hand, the graphite films are the "weak-links" in the tribo-layers: occasionally they cause the delamination of the tribo-layers, but in this case the exposed graphite films provide low friction surfaces. Most damage within the tribo-layers is concentrated between the iron oxide layers on the top and the graphite layers; as shown in Fig. 4.8.b, the size of the Al_3Ni particles was reduced to about 2 μm. Similarly, ceramic particles (in this case SiC) were comminuted to a variety of sizes, the smallest ones were around 5 μm.

A schematic description of the general features of the microstructure of the tribo-layer in a graphitic metal matrix composite is given in Fig. 4.9.

4.2.3. Delamination of Tribo-layers

As mentioned before, tribo-layers form as a result of accumulation and compaction of the by-products of the wear process. The parts of the tribo-layer that are on the top of the graphite layers have two different morphologies as described below:

(a) Tribo-layers with one free end (Fig. 4.10). The tribo-layer may slide parallel to the sliding direction over the graphite layers for distances longer than 1 mm in length (Fig. 4.10). In this case, delamination of the tribo-layer may be due to the high strains (up to 10) in the sliding direction.

(b) In the second type of tribo-layers, the two ends of the tribo-layer on the top of the graphite layer are attached to rest of the tribo-layer (Fig. 4.11.a to 4.11c).

The top part of the tribo-layer is rich in iron oxide so the internal compressive stresses are higher in the topmost part of the tribo-layer than the lower part. Therefore the tribo-layer on the top of the graphite is similar to a blister (Fig. 4.12). When an asperity comes in contact with this type of the tribo-layer it can cause deflecting (buckling) of the tribo-layer as a result of the friction force (which acts as a compressive force on the tribo-layer Fig. 4.12). Assuming that normal and shear forces (friction force) applied by the asperity are constant, when the length of the tribo-layer on the top of the graphite film reaches a critical length the tribo-layer fractures. It is worth mentioning that within the range of graphite particle size in the graphitic composites (70-170 μm), the critical length of the tribo-layer is independent of graphite particle size.

The following simplified assumptions (using the Euler buckling concept [77]) help to calculate the critical length for buckling and collapsing of the tribo-layer under the friction force. The assumptions are two-dimensional stresses, uniform cross-sectional area of the tribo-layer, and no spread of graphite film during graphite film formation (the width of the tribo-layer is equal to the average size of the initial graphite inclusion) See Appendix I for details.

At the applied load P, the critical length L_{cr} at which the tribo-layer buckles is:

$$L_{cr} = \pi\sqrt{\frac{E_{tr} I}{P}} \qquad (4.1)$$

In Equation 4.1 E_{tr} is the modulus of elasticity of tribo-layer and I is the second moment of the cross section area of the tribo-layer. For a rectangular cross-section of the tribo-

layer, $I = wt^3/12$ where w is the width of the tribo-layer and t is the thickness of the tribo-layer. The average diameter of the graphite particles is $w = 10^{-4}$ m, the thickness of the tribo-layer (at 50 N and 3 m/s) is $t = 3 \times 10^{-5}$ m. Therefore $I = 2.25 \times 10^{-19}$.

The maximum modulus of elasticity E_{tr} of the tribo-layer (ignoring the voids and micro-cracks) can be estimated by considering the volume fraction of the constituents of the tribo-layer. Using the inverse law of mixtures, the modulus of the tribo-layer, E_{tr}, is [78]:

$$E_{tr} \approx \frac{1}{\left(\frac{V_{cx}}{E_{Ox}} + \frac{V_{SiC}}{E_{SiC}} + \frac{V_{Si}}{E_{Si}} + \frac{V_{Al}}{E_{Al}}\right)} \qquad (4.2)$$

$E_{ox} \approx 250$ GPa [79], $E_{SiC} = 440$ GPa [78], $E_{Si} = 107$ GPa [82], $E_{Al} = 69$ GPa [78], $V_{Ox} = 0.71$, $V_{SiC} = 0.11$, $V_{Si} = 0.06$, $V_{Al} = 0.12$, The volume fractions were determined by an image analysis method. Substituting these values in Eq. (4.2), $E_{tr} \approx 185.5$ GPa.

P can be estimated from the measured friction force and by estimating the real contact area of each asperity and the number of asperities in contact per unit area. The number of asperities in contact can be estimated from the following Equation [39, 80]:

$$N = \left(\frac{r_o}{r_a}\right)^2 \times \frac{F}{A_n H_o}\left(1 - \frac{F}{A_n H_o}\right) + 1$$

Where N is the number of asperities in contact, r_o is the equivalent radius of the contact surface (m) (the radius of a circular area equal to the nominal contact area), r_a is the radius

of a unit asperity (m), F is the normal load (N) on the sliding interface, A_n is the nominal contact area (m^2), and H_o is room temperature hardness of the steel ring (N/m^2).

At an applied load of 50 N for the geometry of the block-on-ring configuration, the equivalent radius of the contact surface r_o is 3.60×10^{-3} m. Assuming the radius of an asperity r_a is equal to 10^{-5} m [39, 80], and the hardness of the steel ring H_o is 8×10^9 N/m^2, the number of asperities in contact across the contact area is N = 20.

Therefore, the force per unit asperity in contact is $F_1 = 50/20 = 2.5$ N and

$P = F_1\mu = (2.5)(0.5) = 1.25$ N

Substituting the values of *E*, *I*, and *P* in eq. (4.8),

$$L_{cr} = \pi\sqrt{\frac{(1.85\times10^{11})(2.25\times10^{-19})}{1.25}} = 0.574\times10^{-3}\,\text{m} = 0.574\,\text{mm}$$

This is in good agreement with experimental results. SEM observation of the debris shows that the maximum length of the delaminated tribo-layer is less than 0.2 mm (Fig. 4.13.a). Assuming that the buckling divided the tribo-layer into at least 2 to 4 pieces (Fig. 4.13.b and 4.13.c); the original length must have been about 0.7 mm. So, the layers up to 0.7 mm were stable, and if the test was continued the length of the tribo-layers on the top of graphite layers could grow to the critical length and then buckle and delamination of those tribo-layers could occur.

In Equation (4.8), P increases by increasing the load (assuming an almost constant coefficient of friction μ) and E and I are strong functions of the loading conditions. E_{tr} depends on the composition of the tribo-layer (Eq. 4.9) and therefore varies with the

loading condition. By increasing the load and sliding velocity, E_{tr} increases because the tribo-layer becomes richer with iron oxide and I increases as the thickness cubed (Fig.4.14). Therefore, EI/P remains almost constant; then eq. (4.8) predicts that the critical length L_{cr} of graphite film required for delamination of the tribo-layer is nearly constant by increasing the load and sliding speed (Fig. 4.14). This is in good agreement with experimental results. Figs. 4.11.a to 4.11.c show that for the loads of 20 N, 50 N and 150N, at a sliding speed of 2m/s, the lengths of the graphite layers remain constant and equal to about 0.7 mm. The maximum length of graphite film is important, because it confirms that graphite layers longer than a maximum length, as detected by metallographic techniques are unstable and collapse.

The buckling of the tribo-layer on the top of the graphite layer gives an idea for modifying the classic theory of delamination. In the cases where a crack grows underneath the contact surface, the question is always the following:

"How does the crack grow toward the contact surface and delamination occur?" Because the high hydrostatic pressure does not let the crack grow through the layers that are very close to the contact surface, the buckling of the cracked part of the contact surface is an answer in many situations. But, in the calculation of the critical length of the crack for delamination, two other points should be considered. First, the material on the top of the crack is usually continuous in the sliding direction and second, the width of the material on the top of the crack is not necessarily uniform. Therefore, in estimating the force P and the value I, these factors should be considered.

If the distance between two subsequent asperities is d, for delamination of the tribo-layer in graphitic composites the following condition is necessary:

$$d > L_{cr} \qquad (4.3)$$

This means that if an asperity is on top of the tribo-layer (the tribo-layer on top of the graphite layer), the other asperity is not able to delaminate the tribo-layer. This is a random situation that can happen for a given tribo-layer on the top of a graphite layer after several revolutions of the counterface steel ring.

4.2.4. Role of Tribo-layers on Scuffing

Formation of the tribo-layer increased the surface hardness significantly, and played an important role in delaying the mild to severe wear transition in metal matrix composites. However, a negative aspect of the tribo-layers was the scuffing damage that they inflicted on the counterface materials. Scuffing of the counterface occurred in the mild wear regime of the composites (see wear maps in Fig. 4.2), when the tribo-layers covered most of the contact surfaces.

Scuffing could readily be identified from the appearance of the worn steel counterface ring and manifested itself in the form of dark spots, elongated in the sliding direction (up to 3 mm) and protruded (up to 100 μm) from the ring surface. In aluminum alloys, local material transfer to the counterface occurs as the result of localized heating of the contact surfaces during sliding [81]. It was shown that, at high sliding speeds, friction induced heating is high enough to increase the temperature of the asperities to that necessary to initiate local welding of aluminum to steel [81]. In the case of these composites, the abrasive wear action of the delaminated pieces of tribo-layer and

fractured hard intermetallic and ceramic particles in the tribo-layers initiated scuffing. Hard particles of SiC (or Al_2O_3), Al_3Ni, or fragments of iron oxide detached from the tribo-layers in the A356 Al-10%SiC-4%Gr and A356 Al-5%Al_2O_3-3%Gr may act as either two body or three body abrasives against the steel counterface. The hard particles cut longitudinal grooves on the contact surface of the counterface and may occasionally become entrapped at the front end of a groove (Figs. 4.15.a to 4.15.c). The entrapped hard particles act in turn as abrasive elements to the tribo-layer and can remove some parts of the tribo-layer and collect material on the steel counterface. The contact surface temperatures easily reach 300 °C at sliding speeds above 1.2 m/s greatly reducing the shear strength of aluminum [82] and thus facilitating the transfer of the softened material to the counterface. Fig. 4.16.a is a backscattered SEM micrograph that shows the initial stage of aluminum transfer (which is confirmed by the EDS analysis) from the A356 Al-10%SiC-4%Gr to the contact surface of the steel ring. The transferred aluminum particles first accumulated at the tip of the hard asperity or in a groove on the surface of steel, then piled up as their width increased and formed a transferred material island, whose lengths exceed 3mm in Fig. 4.16.b.

4.2.5 Variation of Temperature with Loading Conditions

Fig. 4.17 shows the variation of the measured bulk temperature and calculated tribo-layer temperature at various loading conditions for A356 Al-10%SiC-4%Gr. The temperature variation was similar for A356 Al-5%Al_2O_3-3%Gr. The details of the calculations are explained in Appendix II. Fig. 4.17 shows that at low sliding speeds (e.g. 0.5 m/s) the temperature increased by increasing the load. But it is important to note that at this speed the maximum temperature attained was 120°C (at the maximum test load of

400N). This is likely too low to have an effect on mechanical properties of the composite, and the difference between the temperature of the bulk material and that of the tribo-layer was small (e.g. 20°C). At medium loads (e.g., 50 N) the temperature of the composite increased by increasing the sliding speed (maximum 180°C at 3 m/s). But it is important to note that the difference between the temperature of the bulk material and that of the tribo-layer increased by increasing the sliding speed (e.g. 45°). Knowing the individual thermal conductivities of A356 aluminum alloy, SiC, Gr, and iron oxide and their volume fraction in the bulk material and in the tribo-layer (e.g., at 50 N and 3m/s), the thermal conductivity of the bulk material and the tribo-layer can be calculated. The calculated thermal conductivity of the tribo-layer was significantly lower than that of the bulk material; 25.9 W/K.m.s compared with 140 W/K.m.s for the bulk material (A356 Al-10%SiC-4%Gr). (For more information refer to Appendix II). Therefore, at high sliding speeds, when the rate of heat generation is high, the tribo-layers act as thermal barriers and heat builds up within the tribo-layer increasing the temperature of the tribo-layer relative to the bulk material.

The higher temperature of the tribo-layer has some consequences on the wear behavior of the composite. As the temperature of the tribo-layer increases the counterface becomes more oxidized. This produces more iron oxide debris and makes the tribo-layer richer in iron oxide and decreases the thermal conductivity of the tribo-layer even more. Consequently, the hardness of the tribo-layer increases and becomes more abrasive to the steel counterface and again produces more iron oxide debris and makes the tribo-layer richer in iron oxide. This self-propagation action toward increasing the temperature and iron concentration of the tribo-layer accelerates with increasing the sliding speed. This

becomes even more pronounced by increasing the load at high sliding speeds. At the critical load for the transition from mild to severe wear (e.g. 290 N at 2 m/s), the temperature of the bulk material reaches ≈ 310°C, which is not high enough to reduce the strength of the material below the tribo-layer. Fig. 4.18 shows the yield strength of the composites vs temperature. But when the tribo-layer temperature reaches ≈450°C that reduces the strength of the bulk composite material in contact with the tribo-layer enough for the tribo-layer to slip. Fig. 4.18 indicates that at ≈450°C the yield strength of the A356 Al-10%SiC-4%Gr composite reaches 15 MPa. The measured coefficient of friction at the critical loading condition for the transition from mild to severe wear (2m/s and 275 N) was 0.4; therefore the friction force is 110 N. The nominal contact area was equal to 3 x 10^{-5} m^2 (assuming that the nominal contact area is equal to the interface area of the tribo-layer and the bulk material). Then the shear stress developed by the friction force is 3.67 MPa and the compressive stress due to the applied load of 275 N is –9.2 MPa. Assuming a plane stress condition at the interface of the bulk material and the tribo-layer, the state of stress at the interface is:

$$\begin{vmatrix} 0 & 3.67 \\ 3.67 & -9.2 \end{vmatrix}$$

Therefore the principal stresses are $\sigma_1 \approx 1.26$ MPa and $\sigma_2 \approx -10.46$ MPa, using the Tresca yield criteria [83]:

$$(\sigma_1 - \sigma_2) = 2K = Y$$

where K is shear yield strength and Y is tensile yield strength. Substituting the values, Y ≈ 11.72 MPa. Taking into account thermal and frictional fluctuations during the wear test,

this is in good agreement with the measured yield strength of the composite at ≈ 450°C and explains why the tribo-layer slipped (no longer supported by) over the softened material.

4.2.6. Role of Tribo-layers on Transition to Severe Wear Regime

In the graphitic composites, the transition to severe wear was accompanied by a significant decrease of the hardnesses of the worn surfaces, compared to those reached in the mild wear, where the tribo-layers were present (Fig. 4.3.c). As discussed in Section 4.1.2, at high speed and high load conditions the hardness of the tribo-layer (850 kg/mm^2) was almost ten times higher than the original bulk hardness of the unworn surfaces (91 kg/mm^2). In severe wear, the hardness of the worn surface was still two times higher than the original hardness (i.e. 200 kg/mm^2 at 300 N and 2 m/s) but clearly, the surfaces have lost the hardness and hence, the load supporting capacity provided by the tribo-layers. It is well established that in aluminum alloys and aluminum matrix composites the transition to severe wear is controlled by a critical temperature criterion [8, 46, 84, and 85]. The transition temperatures from mild to severe wear measured for the unreinforced A356 alloy [46], A356 Al-20% SiC [46], A356 Al-10%SiC-4%Gr and A356 Al-5%Al_2O_3-3%Gr composites are given in Table 4.1. Fig. 4.19 shows the comparison of simplified wear maps of A356 Al-10%SiC-4%Gr, A356 Al-20% SiC, and A356 alloy. It shows that by adding silicon carbide to A356 alloy, its resistance to severe wear increases. Adding graphite to the composite makes it superior to the others.

4.2.7. Comparison of Mild to Severe Wear Transition Behavior of Graphitic and Non-graphitic Composites

Mechanically mixed layers containing fractured hard particles were found on the worn surfaces of other aluminum based materials, Al-Si alloys and non-graphitic metal matrix composites, when they rubbed against the bearing steel [46]. However, in the composites without graphite the layers were completely removed at loads lower than those found on the A356 Al-10%SiC-4%Gr composites.

Although the critical transition temperatures for both graphitic and non-graphitic types of composites are similar, (e.g., A356 Al-20%SiC is 601 K and A356 Al-10%SiC-4%Gr is 583 K), higher loads and speeds needed to be applied to reach to the critical transition temperature in A356 Al-10%SiC-4%Gr and A356 Al-5%Al_2O_3-3%Gr compared to non-graphitic composites. In Fig. 4.19, the mild to severe wear transition boundary of the A356 Al-10%SiC-4%Gr and A356 Al-5%Al_2O_3-3%Gr composites are compared with those of the A356 Al-20% SiC composite and the unreinforced A356 alloy. The graphitic composites are clearly superior to the others in delaying the transition to severe wear and hence provide the best seizure resistance against the steel. Fig. 4.20 shows the change in bulk friction induced temperature rises and coefficients of friction of A356 Al-20%SiC and A356 Al-10%SiC-4%Gr composites as a function of load at a constant speed of 2.0 m/s. The figure shows that at the same load and sliding speed conditions the bulk temperature and the coefficient of friction of the A356 Al-10%SiC-4%Gr composite is always lower than that of the A356 Al-20%SiC composite. For example at 150 N, the bulk temperature and the coefficient of friction of A356 Al-10%SiC-4%Gr composite are 548 K and 0.43 respectively compared to 653 K and 0.72

respectively for A356 Al-20%SiC composite. The coefficient of friction of A356 Al-10%SiC-4%Gr decreases with increasing load while the coefficient of friction increases with increasing the load for A356 Al-20%SiC. Without graphite, the energy produced per unit time due to the friction force, and consequently the bulk temperature, increases faster for A356 Al-20%SiC as the load is increased. The coefficient of friction of the graphitic composite is lower because of the solid lubrication action of graphite, which can be attributed to delamination of the tribo-layer or exposure of graphite to the counterface. The lower coefficient of friction in graphitic composites also reduces the shear stresses transmitted to the bulk material underneath the tribo-layer, which is another possible reason that the mild wear regime extends to higher loads and velocities without the removal of the tribo-layer.

It can be concluded that the graphitic composites are well suited to applications where seizure resistance is important, such as, cylinder liners in internal combustion engines. It should be considered that at high sliding speeds (e.g. 1.2 m/s) they cause scuffing on the counterface.

CHAPTER 5

GREY CAST IRON

5.1. Introduction

Grey cast iron is an inexpensive and readily available material. It is universally used for the manufacturing of piston rings and cylinder liners. The combination of good mechanical properties, economical manufacturing route, and good friction and wear characteristics of grey cast iron are unique.

The excellent wear resistance of grey cast iron in dry sliding at low loading conditions is attributed to the feeding of the contact surface by graphite flakes and formation of a graphite film on the contact surface [21-23]. It is generally accepted that a pearlitic structure of the matrix and an ASTM A type graphite flake provides the best wear resistance for grey cast iron in engine cylinder bore applications [1, 64 and 65].

There has been extensive work on constructing wear maps for steels [39, 44], Al-Si alloys [27, 46], and new tribological materials such as metal matrix composites (MMCs) and coatings [66]. Surprisingly, however there is no published wear map for cast iron, which is one of the oldest and cheapest tribological materials. This may be partly because the conditions under which cast iron is used in tribological applications have been established by trial and error over a century. However, the advantages of constructing a wear map for cast iron are numerous: A knowledge of wear regimes and the conditions that lead transitions from one regime to another can be considered as essential information that can be used in finding new wear applications for cast iron. Another advantage of the wear map of cast iron is to provide a bench mark to assess the

wear resistances of new tribological materials such as lightweight aluminum matrix composites that are being developed for automotive applications. In this section experimental work performed in order to construct a wear map for ASTM A 30 type grey cast iron with a pearlitic matrix is described. Specific wear mechanisms which have not been previously reported are discussed.

5.2. EXPERIMENTAL RESULTS

5.2.1. Wear Regimes and Wear Map

The wear rate versus load curves at various sliding speeds for grey cast iron chosen are shown in Fig. 5.1. The mild wear regime extended over a wide range of loads (1.0 N to 60 N) and sliding speeds (0.2 m/s to 3.0 m/s). More exactly, mild wear was observed to occur under the following conditions: At 0.2 m/s between 1 N and 32 N; at 0.5 m/s between 1 N and 30 N; at 0.8 m/s between 1 N and 12 N; at 1.2 m/s between 1 N and 8 N; at 2 m/s between 1 N and 5 N; and at 3 m/s between 2 N and 4.5 N. In the mild wear regime wear rates increased with the load, approximately from 1×10^{-5} mm^3/m, to 10^{-4} mm^3/m. The wear rates of the grey cast iron in the mild wear regime increased linearly by increasing the load from 1 N to 5 N (Fig. 5.1) and obeyed the Archard wear Equation [86].

$$W = K\left(\frac{P}{H}\right) \qquad (5.1)$$

where W is volumetric wear rate in mm^3/m, P is the applied load in kg and H the hardness of cast iron in kg/mm^2. K is the wear coefficient. By substituting the values of W, and P from Fig. 5.1 the value of K can be calculated as 5.02×10^{-3} for the mild wear regime.

A sharp increase in the wear rates appeared at high loads where severe wear occurred. The transition from mild to the severe wear occurred at 37.5 N for the tests at 0.5 m/s, 16.0 N at 1.2 m/s, 10.0 N at 2.0 m/s and 6.5 N at 3.0 m/s. The transition to severe wear was accompanied with material transfer from the surface of cast the iron to the steel ring.

Fig. 5.1 shows that at low loads below 1.0 N wear rates decreased by an order of magnitude compared to the wear rates in the mild wear regime, revealing that another wear regime; i.e., an ultra mild wear regime existed (at 0.2 and 0.5 m/s from 0.2 N to 1 N). In the ultra mild wear regime the value of K (in eq 5.1) was 5.02×10^{-2}.

The transition loads and velocities between these three wear regimes, ultra mild wear, mild wear and severe wear, were determined by visual observations of the changes in the worn surface morphologies during the wear tests and changes in the slope of the wear rate-load curves (Fig. 5.1). Details of the microstructural and compositional changes of the worn surfaces and the debris that took place during wear transitions were studied by SEM and EDS examinations.

The measured wear rates for the A30 type cast iron and the main wear mechanisms operating in each wear regime were summarized on a diagram with log load versus log sliding speed axes. Fig. 5.2 shows the wear map constructed for the cast iron. The three major wear regimes; namely, ultra mild, mild and severe wear regimes are depicted on this map. The wear map indicates that the transition to ultra mild wear was not sensitive to test speeds and occurred at loads below 1 N, where wear rates dropped about an order of magnitude relative to the mild regime. Wear rates in the ultra mild wear regime were about 8×10^{-7} mm^3/m to 9×10^{-7} mm^3/m. In the mild wear regime, the wear

rates were initially about an order of magnitude higher; i.e., in the range of 1×10^{-5} mm^3/m, then increased to 10^{-4} mm^3/m by increasing the load and the sliding speed. In the severe wear regime the wear rates were up to three orders of magnitude greater than those in the mild wear regime (e.g 10^{-1} mm^3/m to 3.2×10^{-1} mm^3/m). There was no tribo-layer in the mild wear regime.

Referring to the wear map of grey cast iron (Fig. 5.2), transition loads P_{tr} from mild to severe and ultra mild to mild wear regimes were approximately linear functions of the sliding speed (in logarithmic scale). Therefore, the Equation that can predict the loads required for the transitions at a given sliding velocity is:

$$\log P_{tr} = C_1 \log V + C_2 \qquad (5.2)$$

Where P_{tr} is the transition load in N, V is the sliding velocity in m/s, and C_1 and C_2 are constants that can be determined from the experimental data. $C_1 = -0.954$ and $C_2 = 1.287$ for the transition between mild and severe regimes and $C_1 = -0.27$ and $C_2 = -0.39$ for the transition between ultra mild and mild regimes.

$$\log P_{tr} = C_1 \log V + \log C_3 \qquad (5.3)$$

where $\log C_3 = C_2$ then, for $C_1 = -1$,

$$P = \frac{C_3}{V} \Rightarrow pV = C_3$$

multiplying both sides by coefficient of friction μ,

$$\mu PV = \mu C_3 \approx \text{cons.} \qquad (5.4)$$

where C_3=19.36

in Equation (5.4), μPV is the rate of shear energy input and for small variations of friction this is almost constant. Therefore the transition from mild to severe wear occurs at a constant power input.

Because of the type of microstructure of grey cast iron, large size debris was formed in the mild and ultra mild wear regimes which could cause scuffing on the contact surfaces or promote the occurrence of severe wear. Fig. 5.3.a shows the morphology formed as a result of failed necks and removal of a large piece of debris on the cross section of the sample in the mild wear regime. Fig. 5.3.b shows the morphology formed as a result of failed necks during the polished process of the surface (similar to the ultra mild regime) and removal of a large piece of debris.

5.3. DISCUSSION

5.3.1. Micromechanisms of Wear

As indicated in Chapter 3, the wear regimes depicted in the wear map (Fig. 5.2) were based on the wear rate information as well as on the metallographic and compositional studies of the worn surfaces that were used to shed light on the microscopic aspects of the wear mechanisms in each of the wear regimes. These are discussed in the following sections.

5.3.2. Ultra Mild Wear Regime

In the ultra mild wear regime, the worn surfaces of cast iron exhibited no significant evidence for plastic deformation and were covered by compacted continuous layers of reddish iron oxide powder. Fig. 5.4.a shows the worn surface of cast iron (at 0.2 N and 0.2 m/s) covered by a compacted fine powder of iron oxide.

Similar iron oxide layers were formed on the surface of the 52100 steel counterface ring in contact with the cast iron samples. The steel counterface exhibited a continuous reddish strip of iron oxide, indicating that the cast iron was separated from the steel ring by an oxide layer. Metal to metal contact between the cast iron samples and the steel ring was largely prevented except the initial stages of wear.

5.3.3. Mild Wear Regime

The mild wear rates in cast iron were primarily controlled by surface oxidation. However, when the applied loads and sliding velocities were modest, the oxide films were thin (a fraction of micrometer) and not continuous throughout the wear tracks, as is shown in Fig. 5.4.b. Under these conditions (2 N, 0.3 m/s) approximately 40% of the contact area was covered with a dark oxide film. The regions between the oxide films consisted of compacted fine reddish iron oxide powder. Increasing the sliding speed and the load increased the proportion of the contact surface area covered by the oxide film. For example, at a sliding speed of 2.0 m/s and a load of 5.0 N, 80 % of the wear track was covered by the dark oxide film (Fig. 5.4.c).

Because of the type of microstructure of grey cast iron, there are some special mechanisms of formation of large size debris, up to 50 μm in length and up to 15 μm in thickness, in mild wear regime. The importance of these large debris becomes more pronounced at loading conditions close to the upper limit of the mild wear regime. As Fig. 3.2 shows, the microstructure of grey cast iron contains some rosette grouped graphite flakes. When these groups are randomly arranged on the contact surface, they form weak points and collapse easily (Fig. 5.5). The result is the formation of large metallic pieces, up to 50 μm in length, which cannot oxidize quickly. They either leave

the system as loose debris or are entrapped in the interface and act as third body objects. Another mechanism that produces large metallic debris in the mild wear regime is the fracture of tiny metallic necks. Tiny necks are formed either during surface preparation before the test or during the wear test. They form because of the presence of the graphite flakes. Fig. 5.6.a schematically shows how graphite flakes cause formation of tiny necks on the surface. It shows that the tiny neck is connected to the bulk material through a tiny metallic neck. The direction of the splat can be either in the sliding direction (Fig. 5.6.a) or in the reverse direction. If they are in the sliding direction, the necks may fail by tensile stress developed within the neck resulting from the friction force (Fig. 5.6.a to 5.6.c). When they are in the reverse direction the necks may fail due to the bending of the splat over the neck as a result of impact of an asperity on the counterface (Fig. 5.7). Fig. 5.3.a. shows the morphology formed as a result of failed necks on a cross section of the sample from the mild wear regime. Fig. 5.3.b shows the morphology formed as a result of failed necks on a polished surface (similar to the ultra mild regime).

In all cases mentioned above, large size debris can be entrapped in the interface of the rubbing surfaces. At high loading conditions, the temperature and pressure of the particle are high enough to cause welding of the particles to the counterface (Fig. 5.8) and provide the necessary condition for transition to severe wear. At loading conditions not high enough for transition to severe wear, the collapsed pieces cause scuffing of the surfaces by scratching the contact surfaces and local material transfer to the counterface

The large size debris forms mostly in the initial stages of the rubbing process. Thus for practical purposes, it is very important to eliminate the sources of these types of debris. These include elimination of the rosette-grouped structure and decreasing the

graphite flake lengths, which should be achieved by conducting the appropriate heat treatment.

In the severe wear regime, oxide films were removed from the contact surfaces as well as iron debris. For this condition the contact surface was continuously removed and there was no opportunity for growing a stable oxide film.

5.3.4. Transition from Mild to Severe Wear Regime

In grey cast iron, the transition to severe wear was accompanied by a significant increase in the roughness of both worn surfaces of the cast iron and of the steel ring. Fig. 5.9 shows the severe deformation at the worn surface of the grey cast iron at 15.0 N and 2.0 m/s. Unlike the aluminum based materials, the transition from mild to severe wear of grey cast iron doesn't happen at a critical bulk temperature (Fig. 5.10). Fig 5.10 shows the variation of the temperature versus the load at the onset of severe wear at different sliding speeds. It shows that at low sliding speeds the rate of heat generation due to friction is low, so the temperature is low (60 °C at 0.2 m/s). The temperature increases by increasing the sliding speed up to 0.8 m/s (rate of heat generation increases). Above 0.8 m/s the temperature decrease as the sliding speed increases, because the contribution of a high deformation rate mode of wear (discussed in the following paragraphs) increases by increasing the sliding speed. In grey cast iron, the transition to severe wear occurred when the flash temperature of the asperities was high enough for local material transfer to the steel counterface. The flash temperature calculations are explained in Appendix III. The material transfer occurred by local welding of asperities or of the large size cast iron debris within the interfaces, when their temperature is high enough. In any case, the cooling rate of the transferred material was high and the hardness of the transferred

material increased up to 5 times that of the bulk material (measured by a micro-hardness method, VHN > 900 kg/mm^2). The material transfer was the starting point of an auto-activated catastrophic wear process. The roughness of the counterface increased from 0.12 μm to about 4 μm. The hard asperities on the counterface were formed by transferred cast iron and in turn welded easily to other cast iron asperities on the contact surface of the cast iron block at high flash temperatures. As soon as welding took place, the temperature of the junction which was greater than 800°C (refer to Appendix III) dropped to the bulk temperature which was measured in all cases to be less than 100°C (Fig. 5.10). The hardness of the junction and the material around it increased to several times that of the bulk material. By continuing the test, failure occurred either at the junction or at the root of the cast iron asperity that is usually adjacent to a graphite flake (stress concentration site). The transferred material grew up to a maximum height of 10 μm on the counterface.

In the early stages of the sliding process, normally for sliding distances less then 5.0 m, the local material transfer process would repeat itself and material transferred to the counterface covered the entire surface of the counterface (Fig. 5.11). The locally transferred material grew up to 10 μm height, 40 μm length and 20 μm width (Fig.5.8). By continuing the test, material transfer, growth and fracture processes progressed in steady state form, where the wear rate was very high but constant. The process could be considered as a high rate forming process where the wear rate was very high (typically 0.2 mm^3/m), but the bulk temperature not very high (e.g. maximum 80 °C at 50 N and 1.2 m/s).

The roughened contact surface of the counterface induced severe plastic deformation on the contact surface of the cast iron. Assuming that an asperity on the contact surface of grey cast iron ideally has a square shape as shown in Fig. 5.12, which is not far from true referring to Fig. 5.4.d. When such an asperity on the steel ring makes contact with a cast iron asperity at a speed of V, the lower strength cast iron asperity (non-hardened material) deforms in the sliding direction. The shear strain rate γ at which the cast iron asperity deforms at each contact is:

$$\dot{\gamma} = \frac{V}{h} \tag{5.5}$$

where h is the height of the cast iron asperity. At a sliding speed 2.0 m/s (2×10^6 μm/s), for a cast iron asperity with $h \approx 2.0$ μm, the shear strain rate is, $\gamma \approx 10^6$ s^{-1}. Therefore, this type of wear process can be classified as a high strain rate deformation processes [87]. It is worth mentioning that the strain rate during a standard Charpy impact test is 10^3 s^{-1} [87]. When local material transfer to the counterface occurred, the very high rate of deformation imposed on the asperities could cause brittle fracture behavior for the cast iron asperities. The presence of graphite flakes, which are locations of stress concentration, increases the possibility of brittle fracture. The sharp edges of the large debris in the severe regime in the micrograph in Fig. 5.13 indicate the brittle fracture in this regime. At these high strain rates, the heat generated during plastic deformation of asperity does not have enough time to dissipate heat to the bulk cast iron. Fig. 5.14 shows the trend of temperature increase by increasing the load at 1.2 m/s. It shows that as soon as severe wear occurred at 1.2 m/s, the bulk temperature dropped from 70 °C to 55 °C. The coefficient of friction in severe wear can be considered to have two components; one

related to the shear force required to fracture the asperities (high deformation rate process), $\mu_{hdr,}$ and the other, is due to the force for non-fracture type interactions of the asperities $\mu_{non\text{-}fr}$.

$$\mu = \mu_{hdr} + \mu_{non\text{-}fr} \tag{5.6}$$

Hardness measurements of the debris in the severe wear regime showed that the hardness of about 25 %vol. of the debris was more than 800 kg/mm^2 and that of the rest was ≈500 kg/mm^2. This indicates that both of mechanisms of debris formation, junction formation, growth and fracture or fracture from the root of the cast iron asperities, described above are active. The hard particles have passed a high temperature and subsequent quench cycle (e.g. a micro-welding process). The particles with lower hardness have failed by the high deformation rate process.

CHAPTER 6

ALUMINUM-SILICON ALLOYS

6.1. Introduction

The scuffing resistances of two eutectic Al-Si alloys with different second phase particle morphologies were investigated after treating their surfaces by chemical etching and mechanical polishing to create different surface topographies. The compositions of the alloys were modified during casting using rare earth elements. Alloy A had the following composition (atomic %): 12.0% Si, 1.0% Fe, 1.0% Cu, 0.1-0.2% Mg, 0.2-0.3%Mn, 0.2-0.3% Zn, 0.2-0.3% La, 0.3-0.4% Ce, < 0.05% Pr, 0.05% Ni, and the balance Al. Alloy B had the same composition but a higher Ni (0.8-0.9 at.% Ni) content. Both alloys were prepared in sand moulds and cooled at different rates after casting (see Chapter 3 for experimental details).

In this chapter the effects of surface modification by chemical etching and mechanical polishing on the scuffing resistances of eutectic Al-Si alloys under light loading conditions are reported. It was shown that at constant load and speed, the sliding distance to scuffing increased with etching time and initial surface roughness up to a certain point, then the onset of scuffing became less sensitive to surface conditions. Second phase particles with small aspect ratios contributed to the delay of the start of scuffing.

6.2 EXPERIMENTAL RESULTS

6.2.1. Etching Results

6.2.1.1. Caustic Etching

6.2.1.1.1. The Effect of The Roughness of The Sliding Surface Before Etching

When a 10% NaOH solution was used as the etchant, the scuffing resistance of the Al-Si alloys was sensitive to their initial surface roughness. In order to study the effect of surface roughness, samples were polished to different roughnesses between 0.14 and 1.2 μm and then etched for a constant time of 7 minutes. Fig. 6.1 shows that when the surface roughness (R_a) of the alloys is low, they exhibit scuffing at short sliding distances, e.g., 200 m for $R_a = 0.14$ μm for alloy A. The sliding distance to the scuffing onset increased with R_a up to about 0.4 μm. For R_a values above 0.4 μm the scuffing resistance became relatively independent of the surface roughness.

The onset of scuffing was detected by measuring the electrical resistance between the pin and the disc. The electrical resistance between the steel pin and Al-Si samples during sliding, prior to scuffing, varied between 20-40 Ω; but when scuffing initiated the electrical resistance dropped to values in the range 0.2-0.7 Ω . Fig. 6.2 illustrates the effect of scuffing on the M2 tool steel counterface worn against sample B.

6.2.1.1.2. The Effect of Etching Time on the Surface Morphology

The surface morphologies of the Al-Si alloys changed with the etching time when etched by a 10% NaOH solution. Figs. 6.3.a to 6.3.d show the change of the morphology of alloy A when etched at room temperature for 1, 4, 7, and 9 min. The dissolution rates of the matrices of the alloys A and B were different. Using the same etchant (10% NaOH

solution), the two alloys had different responses to etching at equal time. Figs. 6.3.e to 6.3.h show the effect of etching time on the surface morphology of alloy B.

The etching solution attacked all the hard phases (except silicon) in addition to the matrix alloy, but with a lower dissolution rate than the matrix. Therefore, when the alloys were etched long etching times (e.g. 7 and 9 minutes), the hard phases (except silicon) were dissolved severely. This effect is evident in Fig. 6.3.h, in which alloy B was etched for 9 minutes. It shows that some of the phases were almost totally dissolved leaving cavities on the surface.

6.2.1.2. The Effect of Acidic Etching on Surface Morphology

The typical surface morphology of sample B etched using 50% HCl for 0.5 minutes is shown in the SEM micrograph taken at a 60° tilt angle (Fig. 6.4). The EDS microanalyses of the etched surfaces of each alloy showed that the area fraction of the silicon phase relative to that of the polished surface increased several times (≈4 times). The average surface roughness R_a before etching was the same for the three alloys and equal to 0.14±0.03 μm, while after etching it was 6.90 ± 0.3 μm for alloy A and 7.15 ± 0.2 μm for alloy B.

6.2.2. Scratch Test Results

As described in Section 2.4, scratch tests were performed on etched surfaces of the Al-Si samples under low normal loads. Fig. 6.5 shows the SEM micrograph of the caustic etched alloy A scratched by a single pass of the Vickers pyramid diamond indenter under a normal load of 10 g. The figure shows that the resistance of phases with different geometry to deformation and fracture during single pass scratch tests are

different. When the ratio of particle width (W_p) to the width of the contact area of the indenter (W_c) is (Wp/Wc) ≅ 1/10, particles on the surface fractured at their root where they were held by the matrix material. For (Wp/Wc) ≅ 1, the particles were more resistant to fracture ("b" in Fig. 6.5) and carried the applied load with less damage.

6.2.3. Wear Test Results

6.2.3.1. Caustic Etched Samples

6.2.3.1.1. Al-Si Alloys As Disc Samples

The wear rates of alloys A and B at a sliding velocity of 0.5 m/s and a load of 5N are shown in Fig. 6.6.a. The sliding surfaces were initially etched by 10% NaOH solution for 7 minutes at room temperature. Fig. 6.6.a shows that alloy A has a lower wear rate (2×10^{-4} mm^3/m) than alloy B (5×10^{-4} mm^3/m). Alloy A could withstand the scheduled sliding distance of 5000 m without scuffing and ploughing while alloy B experienced scuffing at 100m. As a result of scuffing, the etched surface was scratched and ploughed. Figs. 6.6.b and 6.6.c show the scratched surface of alloy B due to scuffing after 500 m sliding distance and non-scratched respectively.

6.2.3.1.2. Al-Si Alloys As Pin Samples

In another series of tests, at the same etching and loading conditions as above, the pin material was made from the Al-Si alloys etched by a 10% NaOH solution for 7 minutes and the disc material from M2 tool steel; Fig. 6.7.a shows the results. The wear rate of alloy B was lower and equal to 4×10^{-4} mm^3/m while that of alloy A was equal to 4.5×10^{-4} mm^3/m. During the test, the etched layer of the pin material was removed. Fig. 6.7.b shows the worn surface of the pin made of alloy A after 5000 m sliding distance. In

Fig. 6.7.b the protruded hard particles are all removed and the wear is in the mild wear regime.

6.2.3.2. Acidic Etched Samples (Al-Si Alloys As Disc Samples)

Fig. 6.8 illustrates the wear rates of Al-Si alloys at the same loading conditions as above but etched by 50% HCl for 0.5 minutes against M2 tool steel. It shows that alloy A had a lower wear rate than alloy B. The etched surfaces of both alloys could withstand the 5000 m sliding distance. The electrical resistance between the pin and the disc remained high ($\approx$15 Ω) with little fluctuations. There wasn't any sign of scuffing on the worn surface of the pins for any of the alloys.

6.2.3.3. As Polished Samples

Fig. 6.9 shows that for the "as polished condition" alloy A has better wear resistance than alloy B. Scuffing and scratching started as soon as the tests were started for both alloys. The electrical resistance between the pin and the disc remained very low (<0.2 Ω) and almost constant in all cases.

6.3. DISCUSSION

Table 3.5 shows that the average hardness of the matrix of both alloys is approximately the same (42 kg/mm^2). Since the weight percent of the main alloying element, silicon, is almost the same in both alloys, the morphology, size, distribution, and fracture toughness of the phases makes their wear and scratch resistance different.

Using a fracture mechanics approach, the wear resistance of the alloys at low loading conditions can be mathematically related to the fracture toughness and the morphology of the hard phases.

6.3.1. Loading and Fracture of The Hard Phases

The resistance of the hard phases to fracture as a result of sliding contact with a hard asperity, or in a specific case a pyramid diamond indenter, can be mathematically related to the morphology of the hard phases. So a simplified model was considered that a Vickers diamond indenter under the normal load P (Fig. 6.10.a) scratched the Al-Si alloy. The Vickers indenter moves under the normal load P along the direction of the diagonal in contact with the matrix alloy, as shown in Fig. 6.10.a. Then it scratches the matrix and pushes a wedge or prow of deforming material ahead. In case of the etched alloy, the hard phases are protruded, so the hard and sharp edge of the indenter directly contacts the hard phase's edge and induces tremendously high stresses at the contact point (Fig. 6.10.a).

6.3.2. Etched Surface

Fig. 6.10.a shows the side view of the scratch system model consisting of a ductile aluminum matrix (m), a hard silicon phase (ph) protruded from the matrix, and a pyramid indenter (i) with the aspect angle 2α. The hard phases geometry is ideally assumed to be in a slab shape with thickness t, height h_t, and width l_1, where $h_t >> h_{ph.}$ The top view of the model in Fig. 6.10.a with the applied forces is presented in Fig. 6.10.b, while it is detached from the matrix.

When the indenter touches the edge of the hard phase, it imposes two types of destructive stresses to the hard phase:

(a) Tensile stress is developed as a result of a bending moment acting normal to the plane m-n in Fig. 6.10.b (point load-continuous support on edge of a cantilever), which should be a maximum at point k. In the real condition the hard phase is supported by the ends and tensile stresses also develop at points T_1 and T_2, but are not as high as that at point k (Fig. 6.10.c). Tensile stresses also develop along the height h_t (similar to a cantilever, because of the bending moment acting normal to the axis $Q\text{-}Q_1$ in Fig. 6.10.a) and is a maximum at k_1.

(b) Very high compressive stress is developed because of the singularity about the sharp indenter edge. A tensile stress also develops consequently under the deformed area at the contact point during unloading.

6.3.2.1. Effect of Tensile Stress Due to Bending Moment

Depending on the height h_{ph} of the protruded part of the hard phase, if the thickness (t) of the hard phase is less than a critical value (t_c), before considerable deformation and damage occurs at the contact edge, the hard phase will break at point k (Fig. 6.10.b) or k_1 (Fig. 6.10.a). The following calculations show that the maximum tensile stress occurs at point k_1.

Assuming the length of the hard phase $L \geq 2B$ where 2B is the width of the groove in the matrix material. Using the flexure formula [77] and assuming that the hard phase material is detached from the surface and supported from one end, the estimated maximum tensile stress at point k in Fig. 6.10.b, $(\sigma_{max})_k$ is:

$$\left(\sigma_{max}\right)_k = \frac{3F_x L}{2h_{ph}t^2} \qquad (6.1)$$

Simplifying the calculations by ignoring the elastic deflection of the matrix, the shear stress, and the elastic deflection of the hard phase in the direction normal to the scratch path, the maximum tensile stress at point k_1 in Fig. 6.10.a, $(\sigma_{max})_{k1}$ is:

$$\left(\sigma_{max}\right)_{k1} = \frac{6 F_x h_{ph}}{L t^2} \qquad (6.2)$$

dividing Eq. (6.1) by Eq. (6.2):

$$\frac{\left(\sigma_{max}\right)_k}{\left(\sigma_{max}\right)_{k1}} = \left(\frac{1}{2h_{ph}}\right)^2 \qquad (6.3)$$

since the Vickers hardness $H_v = \frac{1.8P}{(2B)^2}$ (6.4)

where P is normal load (N) and 2B is the width of the groove on matrix (m).

then $L \geq 2B = \sqrt{\frac{1.8P}{H_v}}$ (6.5)

substituting Eq. (6.5) in to Eq. (6.3):

$$\frac{\left(\sigma_{max}\right)_k}{\left(\sigma_{max}\right)_{k1}} = \frac{1.8P}{4\left(H_v\right)_m \left(h_{hp}\right)^2} \qquad (6.6)$$

in the present experiments (e.g. for alloy A etched for 7 min, by using 10 % NaOH), h_{ph} $\approx 7.5 \times 10^{-6}$ m, $H_v \approx 4.5 \times 10^2$ MPa, and P = 0.05 N. Substituting in Eq. (6.6):

$$\left(\sigma_{max}\right)_k = 0.88 \left(\sigma_{max}\right)_{k1} \qquad (6.7)$$

Since in Fig. 6.10.b, the hard phase is detached from the matrix for simplification in calculations, the calculated value of $(\sigma_{max})_k$ is far above the maximum stress that can be developed at point k in Fig. 6.10.b in real condition. Therefore,

$$(\sigma_{max})_{k1} > (\sigma_{max})_k \qquad (6.8)$$

So fracture starts as a result of the tensile stress developed at point k_1 in Fig. 6.10.a. Then using eqs. (6.2) and (6.5), for P = 0.1 N (the applied load in scratch test), $h_{ph} = 7.5 \times 10^{-6}$ m, $F_x = 0.012$ N (for $\mu = 0.12$ in scratch test), $t \approx 4 \times 10^{-6}$ m, and $H_v = 4.5 \times 10^2$ MPa (measured by microhardness), $(\sigma_{max})_{k1} = 1.7$ GPa. However at the given stress $(\sigma_{max})_{k1}$, the failure of a hard phase depends on the fracture toughness of phase, K_{Ic} [87, 88]. For a semi-circular crack,

$$K_{IC} = 0.71\sigma\sqrt{\pi.c} \qquad (6.9)$$

The K_{Ic} of the hard phases was measured by the micro-hardness method, as described in Section 3.3.2.3, the micro-hardness was performed at 25 g load. Then the diameters, 2c, of the semi-circular cracks (median cracks), that reached the surface of the hard phases after indentation were measured using a SEM. The relation between the critical stress intensity factor K_{Ic}, the applied normal load P, the crack size c (for a semi-circular crack), and indenter tip angle 2α for a crack formed by indentation [89-91] is:

$$K_{IC} = \frac{P}{\left[(\pi.c)^{\frac{3}{2}}(\tan\alpha)\right]} \qquad (6.10)$$

Fig. 6.11 shows the median cracks along the diagonals of the indentation made by Vickers indenter at a normal load of 25g on the $(Fe,Mn)_3Al_{15}Si_2$ phase in alloy A. The calculated K_{Ic} values for the major hard phases using the measured crack lengths and Eq.

6.10, are given in Table 6.1. It shows that the fracture toughness of the intermetallic phase containing Al, Fe and Mn was the highest and that of silicon was the lowest.

Using the average measured $K_{Ic} \approx 0.35$ MPa.$\sqrt{m}$ (Table 6.1), and setting $\sigma = (\sigma_{max})_{kI}$ in Eq. (6.9), the critical crack size required for crack growth in a hard phase due to bending is $c = 1.5x10^{-8}$ m. This is much smaller than the statistically existing surface flaws on the hard phases. So the tensile stress σ_{max} is high enough to initiate crack growth from very small cracks.

Combining eqs. (6.2), (6.4), and (6.9) and setting t as t_c, the critical thickness of the phase is:

$$t_c = \sqrt{\left[\left(\frac{4.2 F_x h_{ph}}{K_{Ic}}\right)\sqrt{\frac{\pi.c(H_v)_m}{1.8P}}\right]} \qquad (6.11)$$

Eq. (6.11) shows that for a given matrix hardness $(H_v)_m$, applied load P, and crack size c, the critical thickness t_c of the hard phase is directly proportional to the square root of the tangential force F_x, the height h_{Si}, and the critical stress intensity K_{Ic} of the hard phase. Therefore, assuming that K_{Ic}, h_{ph} and $(H_v)_m$ of the silicon and Al-Si-Fe-Mn phases (the majority of the phases) and the applied normal load are the same, for the two alloys the fracture of the phases is a function of their critical thickness (t_c).

Using experimental data for the $Al_{15}(Fe\text{-}Mn)_3Si_2$ phase, P = 0.25 N, F_x = 0.03 N, $h_{ph} = 5 \times 10^{-6}$ $c = 0.015 \times 10^{-6}$ m, $K_{Ic} = 0.35$ MPa($m^{1/2}$) [Table 6.1], $H_v = 4.5 \times 10^8$ MPa/m^2 (Table 3.5), the critical thickness is $t_c = 3.5 \times 10^{-6}$ m.

6.3.2.2. *The Effect of High Stress Due to Contact by the Sharp Indenter Edge*

The indenter on the top of a hard phase leads to the formation of lateral cracks. In this case, grooving of the matrix by the tip of indenter ceases and the frictional force on the hard phase is F_T. When the indenter is on the top of the hard phase, it may causes elastic deformation of the hard phase at low applied loads (Fig. 6.12.a), or it may indent the hard phase with some degree of plastic deformation at higher applied loads and it leaves behind a groove (Fig. 6.5). Usually scratching is accompanied by the formation of several cracks normal to the grooving direction (Fig. 6.12.b)

At loads low enough to have only elastic interaction on the top of the hard phase, the plastic deformation was concentrated at the particle edges. This is because of the large stresses caused during the initial contact of the indenter that causes localised plastic deformation. As the indenter moves forward on the particle the contact area increases consequently the stresses decrease to values below the particle yield strength.

If the load is high enough for grooving of the top of the hard phase, the extent of the damage is a function of the thickness of the hard phase and the critical stress intensity factor (K_{Ic}) of the hard phase material.

When the indenter scratches the hard phase a series of half penny cracks form normal to the direction of the indenter movement. The size of these cracks is a function of K_{Ic} of the hard phase material and the applied load, assuming frictionless indentation [92,93]:

$$K_{Ic} = \left(\frac{2P}{B_1 \cdot \pi^{\frac{1}{2}}}\right)\left(\frac{c}{c^2 \cdot \left(\frac{B}{2}\right)^2}\right)^{\frac{1}{2}} \sin\alpha \qquad (6.12)$$

Where $2B_1$ is the width of the groove, 2c the length of the halfpenny crack, and α the indenter tip angle, in this case 68°. In one pass, scratch test cracks do not separate the phase into pieces, but in several passes or in a reverse pass they may.

6.3.3. Loading During Sliding Contact

During the wear test in the etched condition, the contact of the alloy with the counterface asperities was provided only through the hard phases. It is reasonable to assume that under low loads during wear tests the asperity-to-asperity contact is similar to the scratch test at a low loading condition. Therefore, the fracture mechanism of the hard phases can be similar to that of the scratch test.

If each hard phase were assumed to be an asperity, during the wear test the possibility of fracture of the hard phases can be estimated by considering the counterface diameter, the number of hard phases per unit area, the applied load, and the coefficient of friction.

After a short run-in period, the real contact area of pin was roughly about one tenth of the apparent contact area [92]. The hard phases covered an average of 17% of the total surface area of the specimen; so, since the cross sectional area of the pin was equal to 19.6 mm^2, the apparent area of contact was $\approx$ 3.33 mm^2. From Table 3.4 the number of hard phases per mm^2 is 704 for alloy A, and 933 for alloy B. Therefore, the number of hard phases N in contact with the pin counterface is:

$$N_A \approx 260 \times 3.33 \times 0.1 \approx 87$$

$$N_B \approx 329 \times 3.33 \times 0.1 \approx 109$$

The measured friction force during the wear tet of the alloys A and B at 0.5 m/s, and 5N was 2.5N and 3N respectively. Therefore, the average friction force per hard phase, during the wear test was:

$$F_{xA} = 2.5/87 \approx 0.028 \text{ N} \quad (6.13)$$

$$F_{xB} = 3/109 \approx 0.027 \text{ N} \quad (6.14)$$

These forces are comparable with the force applied during the scratch test. So, 5N is roughly the upper limit of load in order to keep the hard phases as the main load supporting areas (staying in the ultra mild wear regime). Above this load, the hard phases fracture and the effects of hard phase morphology on wear and scuffing resistance vanishes. Although eqs. (6.13) and (6.14) indicate that the friction force per individual hard phase is lower for alloy B (because of the higher number of hard phases in alloy B), the force per unit area of the phases is almost the same for all alloys.

As a result of the sliding contact of a hard asperity on the top of a hard phase, cracks form easier close to the "trailing" edges where asperity leaves the phase, Fig. 6.13.a. Very high tensile stresses develop at trailing edges due to the normal load and the frictional force exerted by the sliding asperities of the counterface when they leave the hard phase, Fig. 6.13.b. Although the friction force per hard phase is almost similar for the two alloys and the rate of failure at the edges of the same phases is almost the same for different alloys, the higher number of hard phases in alloy B increases the total rate of hard phase removal due to failure of the trailing edges. This is especially pronounced when the alloy is etched and the matrix doesn't support the highly stressed trailing edges of the hard phases. Fig. 6.14.a is a SEM micrograph of the worn surface of alloy B tested at 5N and 0.5 m/s. The size of the debris is a fraction of a micron (Fig. 6.14.b). EDS

microanalysis (Fig. 6.14.c) shows that the debris consist mainly from silicon rich phases. Fig. 6.14.a shows that a crack is formed at the middle part of the hard phase. At long sliding distances, crack formation and growth in the hard phases by a fatigue-controlled mechanism is very probable.

Another type of failure of hard phases that contributes to the wear rate is lateral crack formation as a result of the sliding of an asperity on a hard phase. Lateral cracks form during the unloading period of an indentation process on a brittle material (or any contact process that causes plastic deformation in brittle materials). In the case of Al-Si alloys the $Al_{15}(Fe,Mn)_3Si_2$ was more sensitive to lateral cracks than the other phases. Fig. 6.15.a shows a lateral crack formed on an $Al_{15}(Fe,Mn)_3Si_2$ phase as a result of an indentation process (under 25 g normal load). When a hard asperity or an indenter slides on a hard phase, lateral cracks are formed in the sliding track. So the lateral cracks produce small size pieces of hard phases. This process is pronounced at the trailing edges. Fig. 6.15.b shows that the lateral crack caused chipping of a part of a silicon phase at the trailing edge during a scratch test under 5 g normal load. For the same reason as that explained above, lateral cracks are more effective in increasing the wear rate in alloy B than alloy A.

Fracture of the hard phases with small aspect ratios due to bending stresses, leaves large broken pieces behind, which is the main cause of scuffing (local material transfer) on the pin counterface.

6.3.4. Scuffing

As a result of scuffing, local material transfer occurred to the counterface and the worn surface was scratched. The effect of the surface condition on scuffing of the Al-Si alloys and the signs of the occurrence of scuffing were mentioned in Sections 6.1.1.1.1 and 6.1.3.2.

The fracture of a large piece of the hard phase can be the cause of scuffing. If the surface is rough enough, the fractured piece can be entrapped in the micro-valleys on the disc contact surface, without causing major damage. When the surface isn't rough, the hard sharp particle can be pushed ahead of the pin. By impacting with other hard phases the particle breaks more large pieces of hard phases.

6.3.5. Differences in Wear Rates by Different Test Configurations

Fig. 6.16 shows the wear rate of the two Al-Si alloys tested by using different configurations of sample and counterface. It indicates that the differences in the resulting wear rates and surface damages of samples tested under different testing methods is considerable. The difference between the results of the tests for which the pin was made of Al-Si alloys and those for which the disc was made of Al-Si, can be explained as follows.

(a) The distribution of pressure at the contact area of a flat pin with a flat surface is shown in Fig. 6.17 [92]. When the pin is made of M2 steel, the concentrated load on the contact edge of the pin makes the loading condition more severe for the Al-Si alloy compared to average contact pressure on the basis of the apparent cross-sectional area be considered. Then the hard phases are overloaded when they

come in contact with the edge of the steel pin especially at the beginning of the test when a few hard phases are in contact with the pin.

(b) When the pin is made of Al-Si alloys, the stress distribution at the edge of the pin isn't as sharp as for the steel pin. In addition, the surface of the alloy experiences more rubbing contact than when it is in the form of a disc. The contact area of the pin is ≈ 0.11 times of the area of the wear track on the disc. Therefore, the actual distance that each point at the middle of the wear track of the samples tested in the disc configuration experiences after the wear test is $(5000) \times (0.11) = 550$ m. On the other hand, The actual sliding distance is 5000m when the pin is made from the Al-Si alloy. This comparison explains the reason why when the pin type test samples were made of Al-Si alloy the etched layer was removed after about 800m sliding distance. Scuffing did not happen for this type of specimen configuration, because overloading at the edge of the pin was unlikely and if a piece of a hard phase was broken, there was no sharp and hard edge like the edge of the steel pin to push the particle ahead against the alloy. The broken particle either scratched the steel disc or left a relatively smooth steel disc wear track by centrifugal force.

CHAPTER 7

OVERALL DISCUSSION

7.1. METAL MATRIX COMPOSITES

When the structure of a metal matrix composite consists of a ductile matrix and hard brittle phases, tribo-layers of the types described in Section 4.2.1 form on the contact surface during dry sliding of the composite against a hard counterface. If the counterface is softer than the hard particles in the composite, then the material transferred from the counterface becomes a part of the tribo-layer (Fig. 4.6.a). In the case of a steel counterface, iron oxide was introduced to the top of the tribo-layer and increased the hardness of the tribo-layer (Fig. 4.4.c). Formation of tribo-layers on the contact surface is usually beneficial for delaying the occurrence of severe wear. Fig. 7.2 shows the effect of tribo-layer formation in the mild wear regime as a result of additives such as hard particle (SiC) and graphite particle to A356 aluminum alloy. By adding 20% SiC particle to the A356 Al alloy formation of tribo-layers in the mild wear regime extends this area to a load 5 times higher than that of the matrix alloy. Adding graphite reduces the coefficient of friction and bulk temperature, therefore teribo-layers are stable at higher loads and sliding speeds. Then by adding graphitic to the aluminum matrix composite reinforced with 10% SiC extends the mild wear regime to the loads up to three times that of the non-graphitic composite. On the other hand tribo layers are usually abrasive to the

counterface. Tribo-layers are not stable for a long sliding distance. They continuously destroy and renew so that in the steady state condition for a constant loading condition the thickness of the tribo-layer remains constant. The delamination of tribo-layers under certain conditions including long sliding distances and high sliding speeds causes scuffing of the counterface (Section 4.2.4). Low thermal conductivity of the tribo-layers is beneficial for the tribological performance of the aluminum-based composites in service (e.g. in cylinder liner). It not only plays a role in initiating a self-hardening mechanism for the tribo-layers (Section 4.2.5), but also makes the tribo-layers act as a thermal barrier which reduces the heat loss through the cylinder wall. Consequently the efficiency of the engine can be improved.

A parameter that can be effective in the ultra mild wear regime in dry sliding conditions is the morphology of the hard particles. Angular particles scratch the counterface during the sliding contact. Rounded or spherical particles should induce the minimum damage to the counterface. But conventional surface preparation methods provide broken hard particles on the surface, which are not beneficial. So a special final finish process (e.g., brushing in presence of running water or using a water jet to remove the broken loose particles from the surface) is required to remove the broken hard particles from the contact surface before the sliding process.

Since the hard particles are the load supporting constituents in the ultra mild wear regime, it is reasonable to suggest that by simply increasing the volume percent of hard particles in aluminum matrix composites, and the silicon content in Al-Si alloys, the possibility of contact can be increased. Consequently the transition boundary of ultra mild to mild wear is extended to higher loads. Taking into account the elastic deflection

of the stiff hard particles compared to the deflection of the less stiff matrix material under the applied load, it is the modulus of elasticity of matrix material that determines the number of hard particles in contact in the ultra mild wear regime. As the load increases the matrix material beneath the particles in contact elastically deflects more and increases the chance that other hard particles will come in contact with the counterface.

One of the simplest classical equations that is widely being used in wear investigations is the Archard equation (Section 5.2). This equation is based on the hardness of the material and the applied load. If the hardness is high, the real area of contact is low, and so is the wear rate. But this can only be true if the material is homogenous and single phase. In the case of MMCs and materials containing hard second phases, the overall hardness doesn't have a direct contribution in wear. It is the hardness and modulus of elasticity of the matrix material that determines the real area of contact (in the ultra mild wear regime). In the mild wear regime the contact surfaces of MMCs are usually covered by tribo-layers. The nature and properties of the tribo-layers are functions of the loading condition. Then considering the hardness of the tribo-layers, the Archard equation can be approximated by introducing a variable hardness in the equation, so that the hardness is a function of applied load and sliding speed. For example in the case of A356 Al-10%SiC-4%Gr at 0.8 m/s and in the load range 5 to 100 N, Fig. 4.4.c, the hardness of the tribo-layer, H_v (kg/mm^2) changes with load P (kg) as:

$$H_V = CP + C_l \qquad (7.1)$$

Where C = 57.8 and C_l = 132.2. The Archard equation in the mild regime (in the load range 5 to 100 N in Fig. 4.1.a) is:

$$W = k\left(\frac{p}{H_v}\right) = k\left(\frac{P}{57.8P + 148.2}\right) \qquad (7.2)$$

where W is the wear rate in mm^3/m and k = 0.168 at a sliding speed of 0.8 m/s. At different sliding speeds the constants C and C_1 in Eq. 7.1 and k in Eq.7.2 are different. e.g. at 2 m/s C = 49, C_1 = 311 and k = 0.3 and at 3 m/s C = 18 and C_1 = 622 and k = 0.54.

7.2. CAST IRON

As Fig. 5.2 shows that the wear map of grey cast iron in dry sliding consists of three main wear regimes, ultra mild, mild, and severe wear regimes. In the mild wear of grey cast iron, the wear rate is low and characterized by the formation of fine oxidized debris. During mild wear the special type of microstructure of grey cast iron leads to the formation of some large size debris (Section 5.2.3). These large size pieces of cast iron remain metallic for a long time during sliding contact and can be harmful at loading conditions close to severe wear regime. If they do not leave the system, they cause scuffing and facilitate the transition to severe wear.

Unlike aluminum based materials in which the transition from mild to severe occurs at a critical bulk temperature, there is no bulk temperature criteria for transition from mild to severe wear in grey cast iron (Section 5.2.4). Instead the transition to severe wear in grey cast iron occurred when the flash temperature of the asperities was high enough for local material transfer to the steel counterface.

When severe wear occurred in grey cast iron, it was catastrophic for all loading conditions. It began with increasing the roughness of the counterface and continued with

a very high wear rate of the cast iron (Section 5.2.4). It was interesting to observe that the severe wear was an high rate deformation process and the temperature rise reached a maximum of 80°C.

In the ultra mild and mild wear regimes grey cast iron had a very good wear resistance and its wear behavior was almost linear and predictable. The transition to severe wear occurred at lower loading conditions compared to the MMCs. Fig. 7.1 shows that at all sliding speeds, the transition to severe wear for A356 Al-10% SiC-4% Gr occurs at loads about 20 times higher than that of cast iron. Therefore, dry sliding tests in this work clearly show that MMCs are less sensitive to oil starvation (in combustion engines) than cast iron.

7.3. ALUMINUM-SILICON ALLOYS

The morphology, size, and distribution of hard phases (Si, Al-Si-Fe, and Al-Si-Fe-Mn phases) in Al-Si alloys have great effects on their wear and scuffing resistance. The effects become more significant when the properly etched samples are tested at low loading conditions (Section 6.1.1). Under these conditions, the fracture of hard phases controls the wear and scuffing resistance of the alloys. As a result of the contact of hard particles with counterface asperities, there are several modes of fracture.

If the fractured parts of the hard phases are large, they can cause local damage as they are pushed in the wear track by the pressure of the counterface. This type of fracture occurs as the result of bending the protruded parts of the particles, which fracture from their root (Section 6.2.3.1). This type of fracture has a determinental effect on the scuffing resistance of the alloy. The higher the number of thin and long phases (low

aspect ratio phases), such as in alloy B, the higher the probability of fracture as a result of bending. This leads to a decrease in the scuffing resistance of the alloy (Fig 6.5).

If the fractured pieces are very small, they don't cause local damage. This type of fracture is the result of the fracture of the trailing edges or chipping of the hard phases. This is attributed to the formation of lateral cracks during sliding contact of an asperity with the hard phase (Section 6.3). This type of fracture does not seem to affect the scuffing resistance of the alloys but has a negative role on the wear rate. The higher the number of the hard particles, as in alloy B, the higher the number of contacts per unit time. This generates a larger number of small broken particles, consequently the wear rate increases.

The effect of an etching condition on the wear and scuffing resistance of the alloys was discussed in Section 6.3. It was shown that a surface finish that was given to the alloys by manual polishing (r_a = 0.4 mm) prior to the caustic etching and an optimum etching time of 7 min provided the best tribological behaviour for the Al-Si alloys.

Using an acidic etchant, a deep etching process provided a superior tribological resistance. This observation contradicts with theoretical analysis of the fracture of the hard phases as a result of bending treated in Section 6.2.3.1. The very low wear rate of the alloys in the case of acidic etching was because of the formation of porous surfaces. The fractured particles were not exposed as hard constituents because they could be entrapped in the depressions and micro valleys of rough and porous surfaces. Therefore they were not active as third body elements. Consequently the weight loss remained very low.

CHAPTER 8

SUMMARY AND CONCLUSIONS

Sliding wear of the graphitic aluminum matrix composites A356 Al-10%SiC-4%Gr and A356 Al-5%Al_2O_3-3%Gr and grey cast iron worn against the SAE 52100 type bearing steel, were investigated under a broad range of loading and sliding speed conditions. The wear rates were measured and the micro-mechanisms responsible for them were identified. The results were summarized in the form of wear mechanism maps.

The effect of hard phase morphology, size, etching time, and surface roughness before etching on wear and scuffing resistance of eutectic Al-Si alloys was investigated using scratch test, pin-on-disc configuration wear tests, and failure analysis of the hard phases.

The main results can be summarized as follows:

1) Mild wear in the graphitic composites was primarily controlled by the formation of the tribo-layers or mechanically mixed and oxidized surface layers on the contact surfaces. The mechanically mixed layers contained fractured SiC (or Al_2O_3), Al_3Ni and Si particles mixed with aluminum. Increasing the sliding speed and the load increased the proportion of the contact surface area covered by the tribo-layers. The hardnesses of the tribo-layers reached about 800 kg/mm^2, more than eight times higher compared to that of the unworn composite.

2) Two important aspects of the tribo-layers in graphitic composites were:

i) The presence of iron oxide layers at the contact surfaces that were significantly thicker and more compact than those formed in non graphitic composites tested under the same conditions;

ii) The formation of lamellar graphite films within the tribo-layers. Graphite films formed as a result of shearing of graphite nodules located just below the contact surfaces, typically at depths of 20-100 μm. The graphite films usually demarcated the boundary between the highly deformed tribo-layers and the relatively damage free bulk material beneath them.

3) At sliding speeds above 1.2 m/s, the steel counterface was subjected to scuffing or local material transfer from the composite. This was mainly attributed to the roughening of the surface of the counterface by the abrasive action of the hard constituents of the tribo-layers and frictional heating induced softening of aluminum.

4) In the severe wear regime the tribo-layers were removed and the hardness of the worn surfaces was greatly reduced.

5) Graphitic composites displayed a transition from mild to severe wear at load and sliding speed combinations, which are higher than those of the unreinforced A356 aluminum alloy and the non-graphitic A356 Al-20% SiC composites.

6) The graphite films within the tribo-layers could grow up to an almost constant critical length and then delaminate because of buckling of the tribo-layer on the top of the graphite layer.

7) The boundary of transition from mild to severe and ultra mild to mild regime of grey cast iron could be predicted from a linear equation in the form of

$$\text{Log}(P) = C_1 \text{Log}(V) + C_2$$

where P is the applied load in kg, V is the sliding speed in m/s, and C_1 and C_2 are constants.

8) Transition from mild to severe in grey cast iron occurs at constant shear energy input.

9) The severe wear of grey cast iron started with increasing the roughness of the counterface due to local welding and material transfer and continued with a very high wear rate of the grey cast iron.

10) Because of the type of microstructure of grey cast iron, there are some special mechanisms of formation of large size debris in mild wear regime which cause either scuffing at low loading conditions or transition to severe wear at loading conditions close to the upper limit of the mild wear regime.

11) The wear rate of Al-Si alloys in the ultra mild wear regime is a strong function of the etching time of the alloy.

12) The wear rate of Al-Si alloys in the ultra mild wear regime is a strong function of the surface roughness before etching.

13) Scuffing resistance of Al-Si alloys was a strong function of the surface roughness before etching and the etching time.

14) Wear and scuffing resistance of Al-Si alloys in the ultra mild wear regime was a strong function of the morphology of the hard phases. In the etched samples, fracture of the hard phases from the roots of the protruded phases caused scuffing of the Al-Si alloys.

15) In the etched samples, fracture of the hard phases from the trailing edges of the hard phases was controlling the wear rate of the Al-Si alloys.

ORIGINAL CONTRIBUTIONS OF THE THESIS IN TRIBOLOGY

For Graphitic Aluminum Matrix Composites

- Characterizing the tribo-layers and identifying their role on tribological behavior of graphitic composites.
- Identifying the scuffing effect on the counterface in dry sliding of aluminum matrix composites in the mild wear regime.
- Suggesting the mechanism of buckling in delamination of tribo-layers in graphitic composites.
- Constructing the experimental wear maps of graphitic composites.

For Gray Cast Iron

- Constructing the experimental wear map of grey cast iron.
- Identifying the mechanism of transition from mild to severe wear in dry sliding of grey cast iron.
- Identifying the mechanism of formation of large size debris and their role in tribological behavior of grey cast iron.

For Aluminum-Silicon Alloys

- Advancing a new method of investigation which is a combination of scratch and wear tests.

- Identifying the effects of roughness and etching time on the wear rate and scuffing resistance of Al-Si alloys.
- Identifying the effect of silicon and hard particles morphology on scuffing resistance and wear rate of Al-Si alloys.

APPENDIX I

The Euler buckling formula can be derived [77] from free body diagram of an element of the tribo-layer constrained from both ends as shown in Fig. A.1. An element of the tribo-layer loaded by the point force P equal to the force applied by an asperity in contact with the tribo-layer is presented in Fig. A.2.

From the equilibrium condition, $\Sigma Fy = 0$, then

$$V(X) = V(X + \Delta X) \text{ or } \frac{\partial v}{\partial x} \qquad (A.1)$$

V is the force in the y direction as a function of X. From the equilibrium condition, $\Sigma M = 0$ (M is the moment as a function of X),

$$M(X+\Delta X) - M(X) = V(X)\Delta X - P\Delta v$$

dividing both sides by x and taking the limit as $\Delta x \rightarrow 0$ then

$$\frac{\partial M}{\partial x} = V - P\frac{\partial v}{\partial x} \qquad (A.2)$$

Differentiating eq. (A.1), using eq. (A.2) and the flexure formula [77] $\frac{\partial^2 v}{\partial x^2} = \frac{M}{EI}$

where E is modulus of elasticity of the tribo-layer and I is the moment of inertia on the cross section of the tribo-layer:

$$\frac{\partial^2}{\partial x^2}\left(\frac{\partial^2 v}{\partial x^2} + \left(\frac{P}{EI}\right)V(X)\right) = 0 \qquad (A.3)$$

Assuming EI is constant, Eq. (A.3) is the differential equation for the analysis of the elastic buckling of a slender column.

Integrating Eq. (A.3) twice gives:

$$\frac{\partial^2 v}{\partial x^2}+\left(\frac{P}{EI}\right)V(X)=k_1+k_2 \qquad (A.4)$$

where k_1 and k_2 are integration constants. The general solution to the equation (A.4) is:

$$V(X)=A\sin\omega s+B\cos\omega c+C_1x+C_2 \qquad (A.5)$$

where A, B, C_1 and C_2 are constants of integration and $\omega^2=\frac{P}{EI}$,

Differentiating Eq. (A.5) twice gives:

$$\frac{\partial^2 v}{\partial x^2}=\frac{M(X)}{EI}=-\omega^2(A\sin\omega s+B\cos\omega c)$$

assuming a pin-connection at the end of the tribo-layer is not too far from true by considering the tribo-layer as a very brittle material with plenty of defects such as cracks. Applying the boundary conditions:

$$M(0)=0 \quad \text{and} \quad M(L)=0$$

$$v(0)=0 \quad \text{and} \quad v(L)=0 \qquad (A.6)$$

from the first condition

$$M(0)=0=A\sin 0+B\cos 0 \quad \therefore B=0$$

the second condition requires that

$$M(L)=0=A\sin\omega L$$

Therefore either A = 0 or

$$\frac{\partial^2 v}{\partial x^2} = \frac{M(X)}{EI} = -\omega^2(A\sin\omega s + B\cos\omega c) \qquad (A.7)$$

where n = 1, 2, 3,……

from the third condition

$$v(0) = 0 = C_2$$

and applying the forth condition

$$v(L) = 0 = A \sin \omega L + C_1 L$$

since A sin ωL = 0, then $C_1 = 0$

Therefore, the critical load P_{cr} which causes buckling of the tribo-layer with the length L into a half sine wave is:

$$P_{cr} = \pi^2 \frac{EL}{L^2} \qquad (A.8)$$

APPENDIX II

In this appendix the method used to calculate the temperature of the tribo-layer of A356 Al-10%SiC-4%Gr worn against SAE 52100 steel is described. The iron oxide content of the top 20 μm of the tribo-layer (Fig. 4.4.d) and a 3 μm iron oxide layer on the topmost part of the tribo-layer are taken into account to calculate thermal conductivity of the tribo-layer in various load and sliding speeds. The measured bulk temperature 5 mm below the contact surface is considered as T_o in Equation B1.

The average surface temperature T_b (bulk temperature) is denoted as "tr" (tribo-layer) and "c" (counterface) in sliding contact is given [39] as:

$$T_b = T_0 + \frac{Fv\mu}{A_n}\left(\frac{k_{eq}}{l_{sb}} + \frac{k_c}{l_{cb}}\right)^{-1} \qquad (B.1)$$

Where T_b is the average surface temperature (K) reached if the frictional heat is injected uniformly across the nominal contact area A_n (m^2). T_0 is the temperature (K) of a point away from the contact surface to which heat flows; k_{eq} is the equivalent thermal conductivity of the sample and k_c is thermal conductivity of the counterface (W/(m.K); l_{sb} and l_{cb} are the equivalent linear heat diffusion distances (m) defined as:

$$l_{sb} = l_s + \frac{A_n k_{eq}}{A_i h_i} \qquad (B.2)$$

And

$$l_{cb} = \frac{r_0}{\sqrt{\pi}} \tan^{-1}\left(\frac{2\pi a_c}{r_0 v}\right)^{\frac{1}{2}} \qquad \text{(B.3)}$$

Where A_i is the contact area (m^2) of the heat sink; h_i is the heat transfer coefficient between the sample and the holder ($W/(m^2.K)$), a_c is the thermal diffusivity of the counterface, and r_o is the length of contact (m)(considered equal to $\sqrt{(A_n/\pi)}$.

For the block on ring testing geometry used for temperature calculations:

$A_n = 5 \times 10^{-5}\ m^2$

$l_{sb} = l_s = 5 \times 10^{-3}\ m$

In eq. (1), k_{eq} is equivalent thermal conductivity of sample. It is calculated on the basis of thermal conductivity of constituents of the composite and their volume fraction, considering a tribo-layer on the contact surface and using the rule of mixtures.

$k_{SiC} = 12.9\ w/m.K^{-1}$ [78]

$k_{A356} = 163\ w/m.K^{-1}$ [64]

$k_{Gr} = 23.8\ w/m.K^{-1}$ [78]

$k_{ox} = 3.2\ w/m.K^{-1}$ [39]

Example:

At 50 N and 3 m/s, for $\mu = 0.5$, $A_n = 5 \times 10^{-5}\ m^2$, $k_{eq} = 136$ W/(m.K), $k_c = 45$ W/(m.K), $l_{sb} = 5 \times 10^{-3}$ m, $l_{cb} = 0.01$ m, and $T_o = 453$ K, T_b is 498 K = 225 °C.

APPENDIX III

In this appendix the method used to calculate the flash temperature of cast iron worn against SAE 52100 steel and the assumptions are described. The measured bulk temperature 5 mm below the contact surface is considered as T_o in eq. (C.1). The number of asperities in contact is assumed to be 10 [76]

The flash temperature of a cast iron asperity T_{casf} is denoted in sliding contact is given as [39]:

$$T_f = T_0 + \frac{Fv\mu}{A_r}\left(\frac{k_{cas}}{l_{casf}} + \frac{k_s}{l_s}\right)^{-1} \qquad (C.1)$$

F = the applied load (10 N)

v = sliding velocity (2 m/s)

μ = coefficient of friction

A_r = real contact area (7.8×10^{-10} m^2)

L_{casf} and l_s = equivalent linear heat diffusion distances for cast iron and SAE 52100 steel (m)

k_{cas} = thermal conductivity of cast iron (55 $W/m.K^{-1}$) [94]

k_s = thermal conductivity of steel (45 $W/m.K^{-1}$) [39]

$$\frac{A_r}{A_n} = \frac{F}{F_s} \qquad (C.2)$$

F_s = seizure load (N)

$$l_{casf} = \frac{r_j}{\pi^{\frac{1}{2}}} \tan^{-1}\left(\frac{n2\pi a_{cas}}{r_j v}\right)^{\frac{1}{2}} \tag{C.3}$$

where:

r_j = radius of contact junction (m)

a_{cas} = thermal diffusivity of cast iron (1.59×10^{-5} m^2/s) [94]

$$l_{sf} = \frac{r_j}{\pi^{\frac{1}{2}}} \tan^{-1}\left(\frac{n2\pi a_s}{r_j v}\right)^{\frac{1}{2}} \tag{C.4}$$

a_s = thermal diffusivity of SAE 52100 steel (1.2×10^{-5} m^2/s) [39]

$$r_j = r_o\left(\left(1-\frac{F}{F_s}\right)\left(\frac{r_o}{r_a}\right)^2+1\right)^{\frac{-1}{2}} \tag{C.5}$$

r_o = the length of contact (considered equal to $\sqrt{(A_n/\pi)}$.

r_a = radius of a single asperity junction (5×10^{-6} m)

$$F_s = \frac{A_n H_o}{\left(1+12\mu^2\right)^{\frac{1}{2}}} \tag{C.6}$$

$$T'_b = T_b - \frac{A_r}{A_n}\left(T_b - T_o\right) \tag{C.7}$$

Example:

At 10N and 2 m/s for $\mu = 0.5$, $A_r = 7.8 \times 10^{-10}$, $l_{casf} = 5 \times 10^{-6}$ m, $l_{sf} = 9 \times 10^{-6}$ m, $k_{cas} = 55$ W/(m.K), $K_s = 45$ W/(m.K) and $T_b = 353$ K, the flash temperature $T_f = 1154$ K = 881 °C

REFERENCES

[1] ASM Handbook, Vol. 18, Friction, Lubrication and Wear Technology, 10th ed, ASM International, Metals Park, OH, 1992. pp. 553-562.

[2] Gibson, P.R.; Clegg A.J. and Das, A.A.; Mater. Sci. & Techn., Vol. 1, pp. 559-567, 1985.

[3] Prasad, S.V. and Rohatgi, P.K.; Journal of Metals, no.11, pp. 22-26, 1987.

[4] Rohatgi, P.K.; Ray, S. and Liu, Y.; International Mater. Reviews, Vol. 37, no. 3, pp. 129-148, 1992.

[5] Das, S.; Prasad, S.V. and Ramachandran, T.R.; Mater. Sc. and Eng., A138, pp. 123-132, 1991.

[6] Das, S. and Prasad, S.V.; Wear, 133, pp. 173-187, 1989.

[7] Prasad, S.V. and McConnel, B.D.; Wear of Materials, ASME, pp. 149-157, 1991.

[8] Ames, W. and Alpas, A.T.; Metall. and Mater. Trans. A, Vol. 26A, pp. 85-98, 1995.

[9] Okayabashi, K. and Kawamoto, M.; Bull. of the Univ. of Osaka, Prefecture A, Vol. 17, pp. 199-216, 1968.

[10] Shivanath, R.; Sengupta, P.K. and Eyre, T.S.; ASME IntI. Conf. on Wear of Mater, pp. 186-192, 1977.

[11] Clegg, A. J. and Das, A. A.; Wear, Vol. 43, pp. 367-373, 1977.

[12] Sarker, A. D. and Clark, J.; Wear, Vol. 31, pp. 331-339, 1975.

[13] Pramila Bai, B. N.; Biswas, S. K. and Kumtekar, N. N.; Wear, Vol. 87, pp. 237-249, 1983.

[14] Jasim, K. M.; Wear, Vol. 98, pp. 183-190, 1984.

[15] Andrews, J. B.; Senoviratne, M. V.; Zior, K. P. and Jett, T. R.; The American Society of Mechanical Engineers, pp. 180-185, 1985.

[16] Jasim, K. M. and Dwarakadasa, E. S.; Wear, Vol. 119, pp. 119-130, 1987.

[17] Perrin, C. and Rainforth, W. M.; Wear, 203-204, pp. 171-179, 1997.

[18] Tandon, K. N. and Li, X. Y.; Scripta Materialia, Vol. 38, no. 1, pp. 7-13, 1998.

[19] Li, X. Y. and Tandon, K. N.; Wear, 225-229, pp. 640-648, 1999.

[20] Yen, B. K. and Ishihara, T.; Wear, Vol. 198, pp. 169-175, 1996.

[21] Takeuchi, E.; Wear, Vol. 11, pp. 201-211, 1968.

[22] Montgomery, R. S.; Wear. Vol. 14, pp. 99-105, 1969.

[23] Sugishita, J. and Fujiyoshi, S.; Wear, Vol. 66, pp. 209-221, 1981.

[24] Everett, P. K. and Arsenault, R. J.; Metal Matrix Composites: Processing and Interfaces, Academic Press Inc., pp. 1-2, 1991.

[25] Boudina, A.; Riahi, A. R. and Alpas, A. T.; Tribological design of Graphitic Metal Matrix Composite Cylinder liner Materials, Part I Lubricated , Report to INCO , Feb. 12, , 2001.

[26] Rohatgi, P.K.; Liu, Y. and Barr, T.L.; Metall. Trans. A, Vol. 22A, pp. 1435-1441, 1991.

[27] Shivanath, R.; Sengupta, P.K. and Eyre, T.S.; Br. Foundryman, Vol. 70 pp. 349-356, 1977.

[28] Razavizadeh, K. and Eyre, T.S.; Wear, Vol. 79, no. 3, pp. 325-333, 1982.

[29] Razavizadeh, K. and Eyre, T.S.; Wear, Vol. 87, no. 3, pp. 261-271, 1983.

[30] Antoniou, R. and Borland, D.W.; Mater. Sc. and Eng., Vol. 93, pp. 57-72, 1987.

[31] Tandon, K.N. and Li, X.Y.; Scripta Materialia, Vol. 38, no. 1, pp. 7-13, 1998.

[32] Yen, B.K. and Ishihara, T.; Wear, Vol. 198, pp. 169-175, 1996.

[33] Jiang, J.; Stott, F. H. and Stack, M. M.; Wear, 181-183, pp. 20-31, 1995.

[34] Heilmann, P.; Don, J.; Sun, T. C.; Rigney, D. A. and Glaeser, W. A.; Wear, Vol. 91, pp. 171-190, 1983.

[35] Subramanian, C.; Wear, Vol. 161, pp. 53-60, 1993.

[36] Iwai, Y.; Yoneda, H. and Honda, T.; Wear, 181-183, pp. 594-602, 1995.

[37] Antoniou, R. A.; Brown, L. R. and Cashion, J. D.; Acta Metall. Mater., Vol. 42, pp. 3545-3553, 1994.

[38] Welsh, N.C.; J. of Appl. Phys., Vol. 28, no.9, pp. 960- 968, 1957.

[39] Lim, S.; Ashby, M. B.; Acta Metallurgica, Vol. 35, pp. 1- 24, 1987.

[40] Atoniou, R and Subramanian, C.; Vol. 22, pp. 809-814, 1988.

[41] Wang, D. Z.; Peng, H. X.; Liu, J. and Yao, C. K.; Wear, Vol. 184, pp. 187-192, 1995.

[42] Liu, Y.; Asthana. R. and Rohatgi, P.K.; J. Materials Sci., Vol. 26. pp. 99- 102, 1991.

[43] Rohatgi, P.K.; Liu, Y.; Asthana. R.; in Rohatgi, P.K.; Blau, P.I.; Yust, C.S. (Eds.), ASM, pp. 69- 80, 1990,

[44] Kato, H.; Eyre, T. S. and Ralph, B; Acta Metall. Mater., Vol. 42, no. 5, pp. 1703-1713, 1994.

[45] Zhang, J. and Alpas, A.T.; Acta Mater. Vol. 45, pp. 513- 528, 1997.

[46] Wilson, S. and Alpas, A.T.; Wear, Vol. 212, pp. 41- 49, 1997.

[47] Edrisy, A.; Perry, T.; Cheng, Y. T. and Alpas, A. T.; Wear, Sep. 2001.

[48] Ludema, K.C.; Wear, Vol. 100, pp. 315- 331, 1984.

[49] Dyson, A.; Tribology International, April, pp. 77-87, 1975.

[50] Dyson, A.; Tribology International, June, pp. 117-122, 1975.

[51] Galligan, J.; Torrance, A. A. and Liraut, G.; Wear, Vol. 236, pp. 199-209, 1999.

[52] Galligan, J.; Torrance, A. A. and Liraut, G.; Wear, Vol. 236, pp. 210-220, 1999.

[53] Sarkar, A. D. and Clarke, J.; Wear, Vol. 61, pp. 157-167, 1980.

[54] Jacobsen, E. G.; Society of Automotive Engineers, Inc. pp. 29-34, 1983.

[55] Renninger, G.; Abendroth, D. and Bolien M.; Society of Automotive Engineers Inc., pp. 9-15, 1983.

[56] Yoon, H. K.; Sheiretov, T. K. and Cusano, C.; Wear, Vol. 237, pp.163-175, 2000.

[57] Cavatorta, M. P. and Cusano, C.; Wear, Vol. 242, pp. 133-139, 2000.

[58] Lee, Y. Z. and Kim, B. J.; Wear, Vol. 232, pp.116-121, 1999.

[59] Sheiretov, T. K.; Yoon, H. K. and Cusano, C.; Tribology Transactions, Vol. 41, no. 4, pp. 435-446, 1998.

[60] Somi Reddy, A.; Pramila Bai, A. B.; Murthy, K. S. S. and Biswas, S. K.; Wear, Vol. 171, pp. 115-127, 1994.

[61] Jasim, K. M. and Dwarakadasa, E. S.; Journal of Materials Science Letters (UK), Vol. 11, no. 7, pp. 421-423, 1992.

[62] Barber, G. C.; Mathews, J. J. and Jafry, S.; Lubrication Eng., Vol. 47, pp. 423-430, 1991.

[63] Eyre, T. S.; Met. Technol., Vol. 11, no. 3, pp. 81-90, May 1984.

[64] Metals Handbook, vol. I, Properties and Selection: Irons and Steels, 9th edn, ASM, Metals Park, OH, pp. 25-26, 1987.

[65] Leech, P. W. and Borland, D. W.; Wear, Vol. 85, pp. 257-266, 1983.

[66] Eyre, T. S.; Iles, R. F. and Gasson, D. W.; Wear, Vol. 13, pp. 229-245, 1969.

[67] Montgomery, R. S.; Wear, Vol. 13, pp. 337, 1969.

[68] Rhee, S. K. and DuCharme, R. T.; Wear, Vol. 23, pp. 271, 1973.

[69] Leech, P. W., and Borland, D. W.; Mater. Sci. Eng., Vol. 66, pp. 167-177, 1984.

[70] Lathabai, S.; Scripta materialia, Vol. 38, no. 10, pp. 1557-1562, 1998.

[71] *Stephenson, T. F. and Bell, J. A. E.; in Canadian Institute of Mining, Metallurgy* and Petroleum (Canada) R.A.L Drew and Mostaghaci, H., Eds., CIM, Montreal; pp. 51-60, 1993.

[72] Annual Book of ASTM Standards, Metals-Mechanical Testing; ASTM E 8M-99, Vol. 03.01, 1999.

[73] Annual Book of ASTM Standards, Metals-Mechanical Testing; ASTM E209-65, Vol. 03.01, 1999.

[74] Annual Book of ASTM Standards, Physical Properties, Vol. 04.02, ASTM C127-01, 2000.

[75] Zang, J. and Alpas, A. T.; Mater. Sci. Eng., Vol. A 161, pp. 237, 1993.

[76] Moore, M. A. and Douthwaite, R. M.; Metall. Trans. A, Vol. 7, pp. 1833, 1976.

[77] Eisenberg, M. A.; Introduction to Mechanics of solids, Addison Willey Publishing Company, Inc., 1980.

[78] Ashby, F. and Jones, R. H.; Engineering Materials, Butterworth-Heinemann, pp. 62-64, 1997.

[79] Quinn, T. F. J. and Winer, W. O.; Wear, Vol. 102, no. 1-2, 67-80, 1985.

[80] Wilson, S. and Alpas, A. T.; Wear, Vol. 225-229, part I, pp. 440- 449, 1999.

[81] Singh, J. and Alpas, A. T.; Metall. Mater. Trans A, Vol. 27, pp. 3135, 1996.

[82] Rowe, G. W.; Principles of Industrial Metalworking Processes, Edward Arnold, pp. 35-48, 1977.

[83] Martin, A.; Martinez, M. A. and Ilorca, J.; Wear, Vol. 193, pp. 169-179, 1996.

[84] Reddy, A. S.; Pramila Bia, B. N.; Murthy, K. S. S. and Biswas, S. K.; Wear, Vol. 17, pp. 115-127, 1994.

[85] Wilson, S. and Alpas, A. T.; Wear, Vol. 196, no. 1-2, pp. 270-278, 1996.

[86] Eyre, T. S. and Maynard, D.; Wear, Vol. 18, pp. 301, 1971.

[87] Dieter, G. E.; Mechanical Metallurgy, McGraw-Hill, 1986.

[88] Hertzberg, R. W., Deformation and Fracture Mecanics of Engineering Materials, Second Ed., John Wiley & Sons, pp. 303-306, 1983.

[89] Paris, P. C. and Sih, G. C.; Amer. Soc. Mater. Spec. Tech. Publ. Vol. 381, pp. 30-42, 1965.

[90] Lawn, B. R. and Fuller, E. R.; J. Mater. Sci., Vol. 10, pp. 2016-2024, 1975.

[91] Williams, J. A.; Tribology International, Vol. 29, no. 8, pp. 675-694, 1996.

[92] Zum Gahr, K. H.; Microstructure and Wear of Materials, Tribology Series, Vol. 10, Elsevier, Amsterdam, 1987.

[93] Sugita, T. and Hasegawa, T.; J. Mater. Sci., Vol. 13, pp. 1471-1479, 1978.

[94] Kreith, F., Principles of Heat Transfer, Third Ed. Happer & Rew Publishers, pp. 634, 1973.

Table 3.1.a

Material Properties	A356 Al-10%SiC-4%Gr	A356 Al-5%Al_2O_3-3%Gr
Graphite nodule length And width (μm)	138 ± 25 80±15	170 ± 30 70±12
SiC average diameter (μm)	16 ± 2	N/A
Al_2O_3 average diameter (μm)	N/A	17± 2
Al_3Ni morphology	Script	Script
Al_3Ni Volume%	3	3
Al_3Ni length and width	8±2 2±0.5	9±2 1.7±0.5

Table 3.1.b

Material / Properties	A356 Al-10%SiC-4%Gr	A356 Al-5%Al_2O_3-3%Gr
Vickers Hardness (kg_{1000g}/mm^2)	91.1 ± 5.4	99.6 ± 2.7
Density (Mg/m^3)	2.74	2.77
Tensile strength (MPa) at 298 K	109.6	107.8
Percent elongation	3	2.5
Compressive flow stress (MPa) at $\varepsilon = 0.02$ and 298 K	180.4	190.3

Table 3.2

Material	Hardness at 25g (kg/mm^2)	Density (g/mm^3)	Tensile Strength (MPa)	Type (ASTM, AFS)
Gray Cast Iron	**251 ± 10**	**7.3 ± 0.3**	**248**	**A30**

Table 3.3

	Alloy A Atomic%	Alloy B Atomic%
Si	~12.0	~12.0
Fe	1.0	1.0
Cu	1.0	1.0
Mg	0.1 to 0.2	0.1 to 0.2
Mn	0.2 to 0.3	0.2 to 0.3
Zn	0.2 to 0.3	0.2 to 0.3
La	0.2 to 0.3	0.2 to 0.3
Ce	0.3 to 0.4	0.3 to 0.4
Pr	<0.05	<0.05
Ni	<0.01	0.8 to 0.9
Ti, V, Cr, Ga, Zr, Cd, Sn, Sb, Pb, Bi	<0.1	<0.1

Table 3.4

	Sample A	Sample B
Average aspect ratio of silicon phase	2.59	2.74
Average aspect ratio of $Al_{15}(Fe, Mn)_3Si_2$ phase	2.93	3.21
Max. length of silicon phase μm	118.88	136.99
Average thickness of silicon phase μm	5.41	4.27
Max. length of $Al_{15}(Fe, Mn)_3Si_2$ phase μm	122.13	538.44
Average thickness of $Al_{15}(Fe, Mn)_3Si_2$ phase μm	4.88	3.22
Average area% of silicon phase	11.89	12.38
Average %area of $Al_{15}(Fe, Mn)_3Si_2$ phase	5.13	6.34
Average % area of total phases	17.02	18.72
Average # of silicon phase/mm^2	170	282
Average # of $Al_{15}(Fe, Mn)_3Si_2$ phase/mm^2	90	47
Average # of total particles/mm^2	260	329

Table. 3.5

Phase	Hardness at 25g Load (kg/mm^2)		
	Alloy-A	**Alloy-B**	**Ref. Pure Silicon**
Matrix	40.5 ± 1	40.9±1	--
Overall at 500g Load	74.4±3	74.3±2.9	--
Silicon	957±36	941±34	936±38
$(Fe,Mn)_3Si_2Al_{15}$ round	662±20	647±28	--
$(Fe,Mn)_3Si_2Al_{15}$ long	498±40	502±44	--

Table. 3.6

Sample	1	2	3	4	5	6
Silicon Carbide Grinding Paper	180	180 and 240	180, 240 and 320	180, 240, 320, and 400	180, 240, 320, 400, and 600	180, 240, 320, 400, 600, and polished with 1mm Al_2O_3 Suspension
The obtained roughness Ra (μm)	1.7	1.2	0.7	0.4	0.25	0.14

Table 4.1

Material	A356 Al alloy	A356 Al-20%SiC	A356 Al-10%SiC-4%Gr	A356 Al-5%Al_2O_3-3%Gr
Critical Transition Temperature (K)	398±5	601±10	583±10	553±9

Table. 6.1

Phase	Critical Stress Intensity Factor K_{Ic} (Mpa.$\sqrt{m}$)		
	Alloy-A	Alloy-B	Pure Silicon
Silicon	0.3±0.42	0.57±0.045	0.41±0.052
$(Fe,Mn)_3Si_2Al_{15}$ round	0.4±0.04	0.32±0.092	--
$(Fe,Mn)_3Si_2Al_{15}$ long	0.2±0.05	0.24±0.08	--

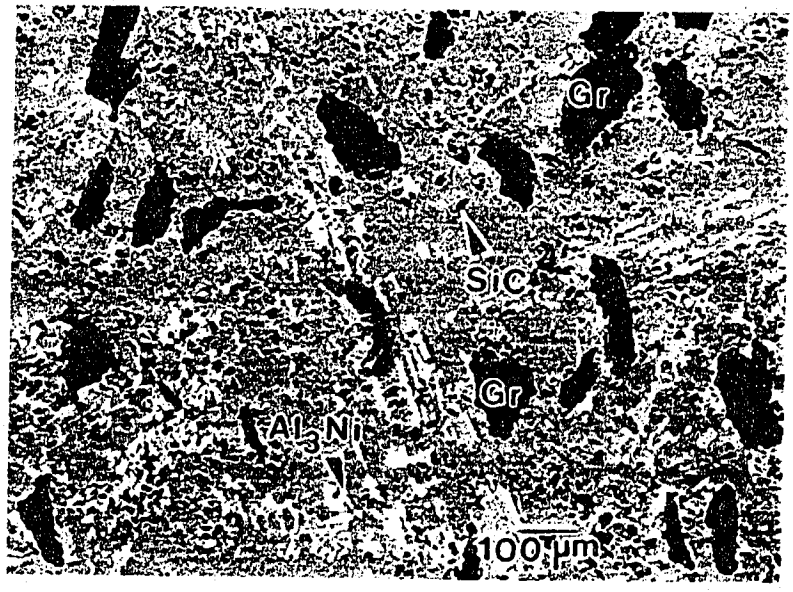

Fig. 3.1. (a) Microstructure of A356 Al-10%SiC-4%Gr (back scattered SEM), the microstructure shows the graphite particles (dark constituents), the SiC particulates and the Al_3Ni phase (light constituents) in the A356 Al matrix.

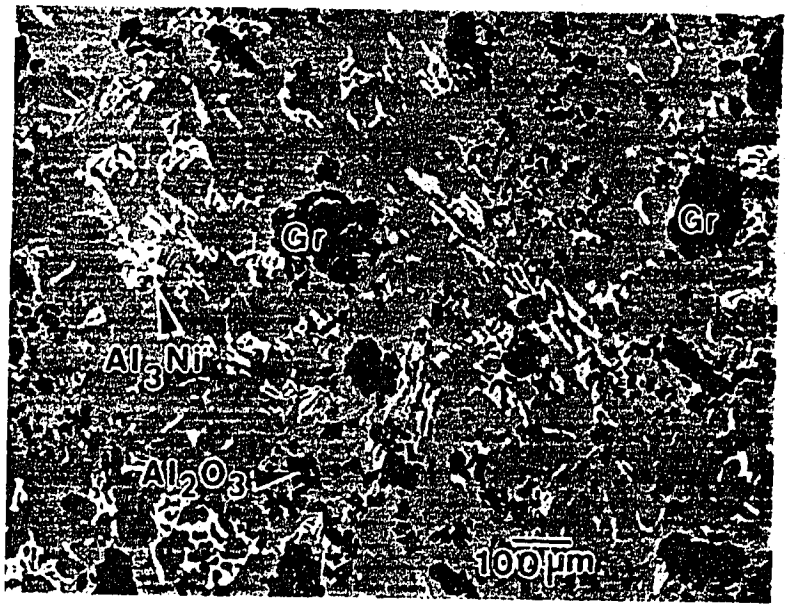

Fig. 3.1. (b) Microstructure of A356 Al-5%Al_2O_3-3%Gr (back scattered SEM), it shows the same constituents as (a) but Al_2O_3 particulates replace SiC particulates.

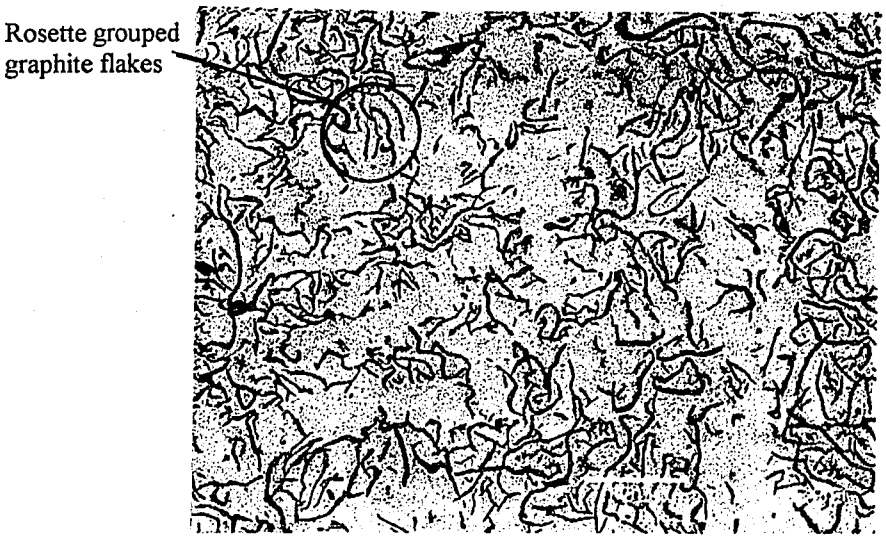

Fig. 3.2. Microstructure of grey cast iron with type A of graphite distribution.

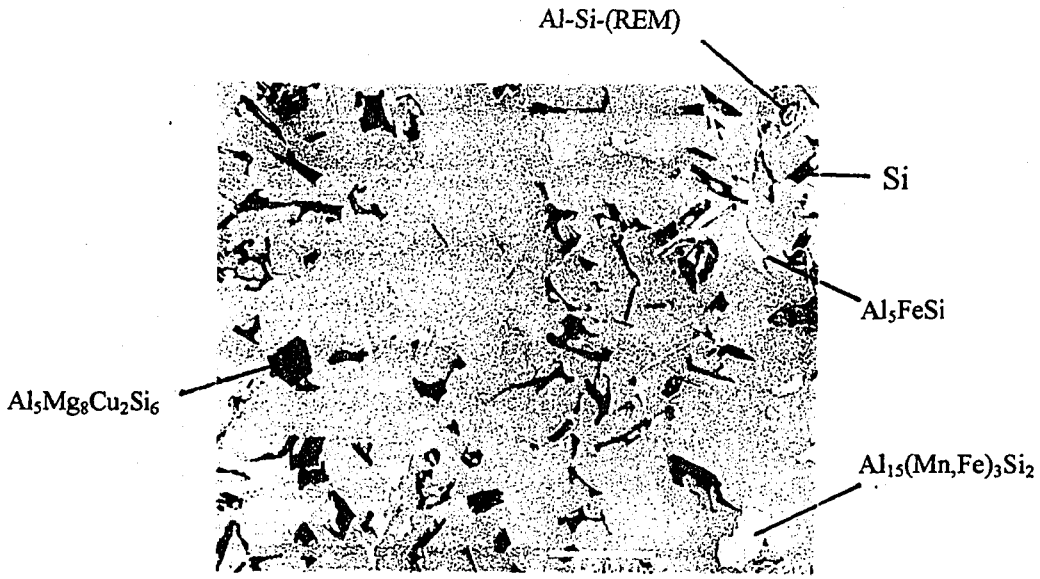

(a)

Fig. 3.3. (a) Microstructure of Al-Si alloy A which contains silicon phases (dark grey), $Al_{15}(Mn, Fe)_3Si_2$ phase (round grey phase), Al_5FeSi phase (elongated light grey phase), rare metal rich phases (light phase).

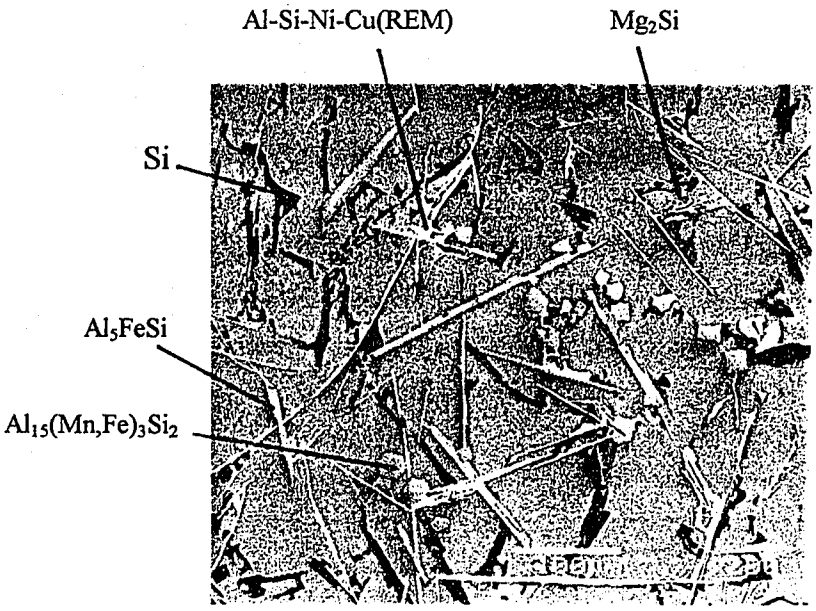

(b)

Fig. 3.3. (b) Microstructure of alloy B which contains the same phases as alloy A but with acicular shape, it also contains a small volume fraction of Mg_2Si (small black phase).

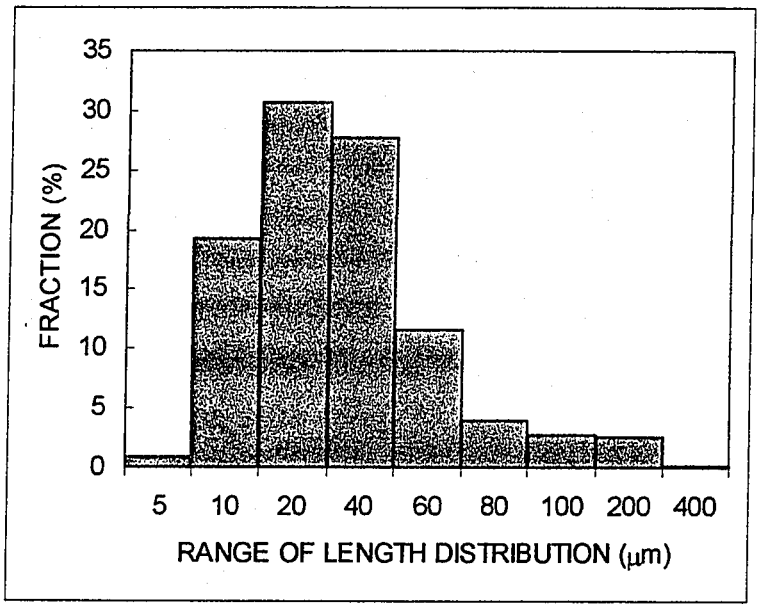

Fig. 3.4. (a) Distribution of length of hard phases in alloy A

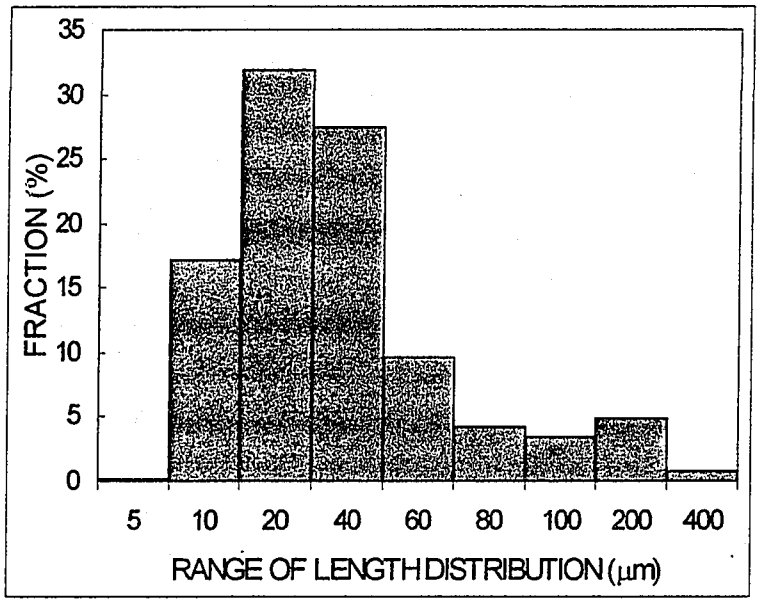

Fig. 3.4. (b) Distribution of length of hard phases in alloy B

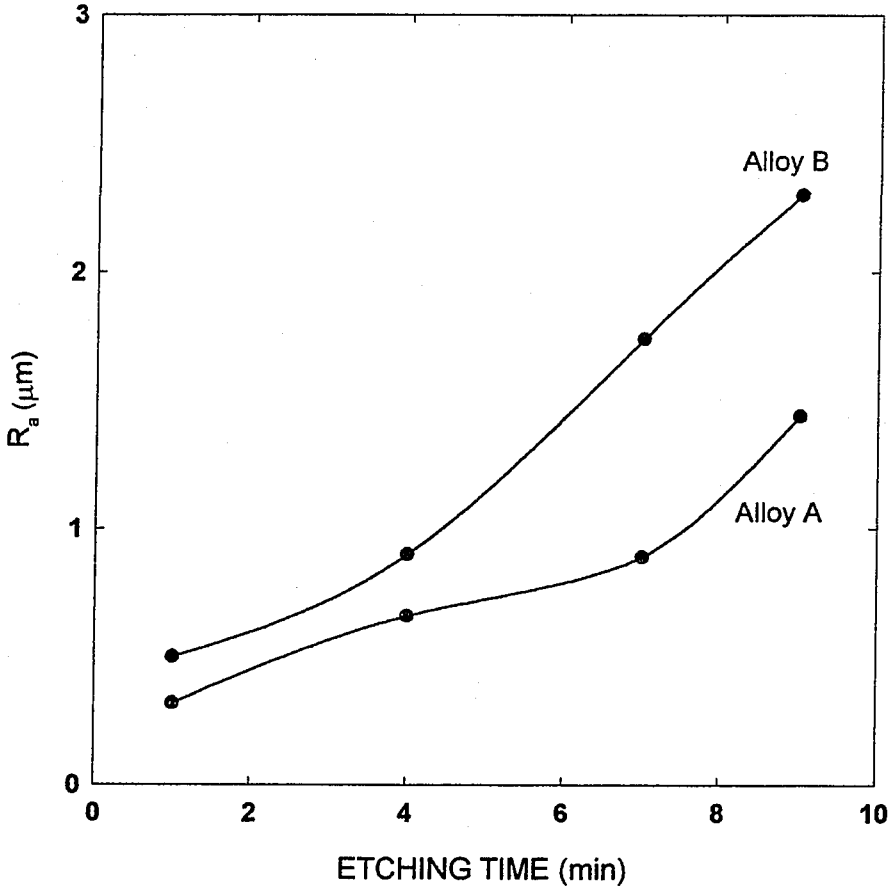

Fig. 3.5. The variation of the roughness of the etched faces of alloys A and B as a function of the etching time.

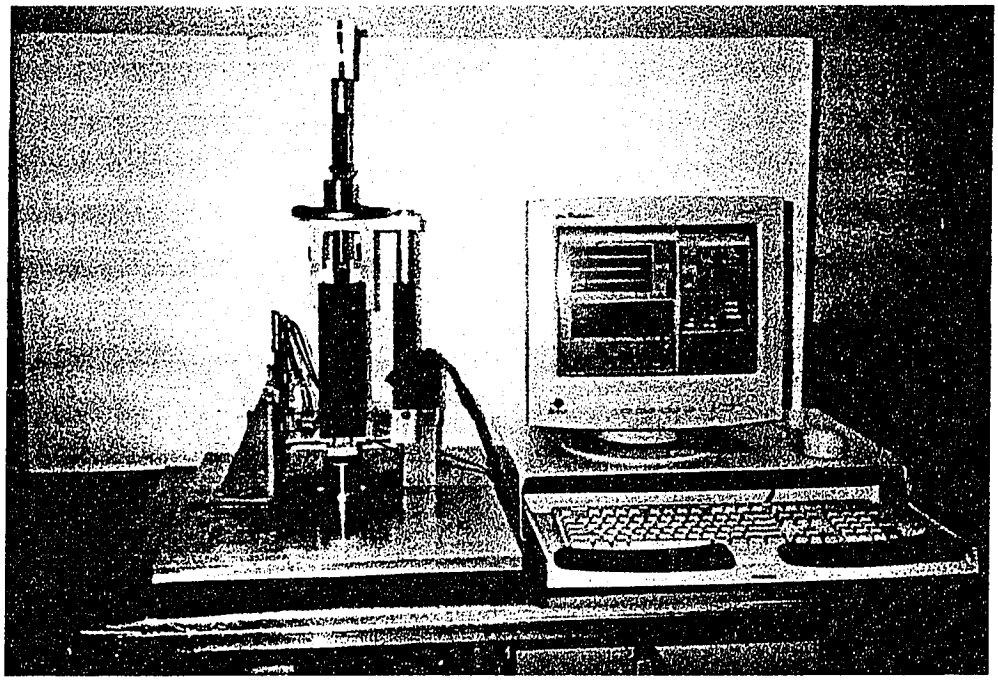

Fig. 3.6. The pin-on-disc sliding wear machine.

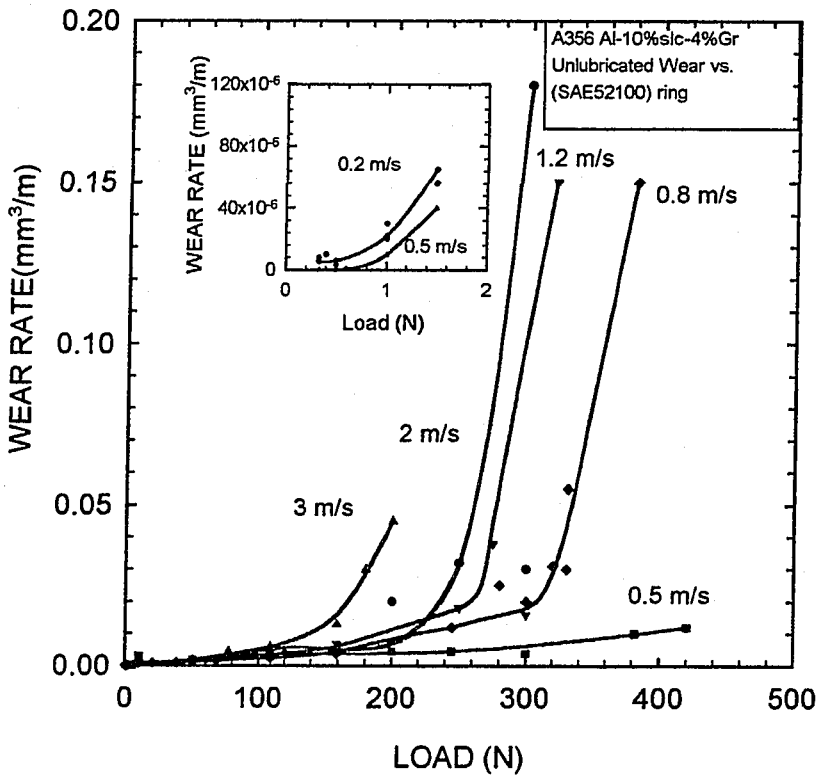

Fig. 4.1. (a) Wear rate versus applied load diagram at different sliding speeds for A356 Al-10%SiC-4%Gr. The insert shows the wear rates obtained in the ultra mild regime for loads between 0.33 to 1.5 N at sliding speeds of 0.2 m/s to 0.8 m/s.

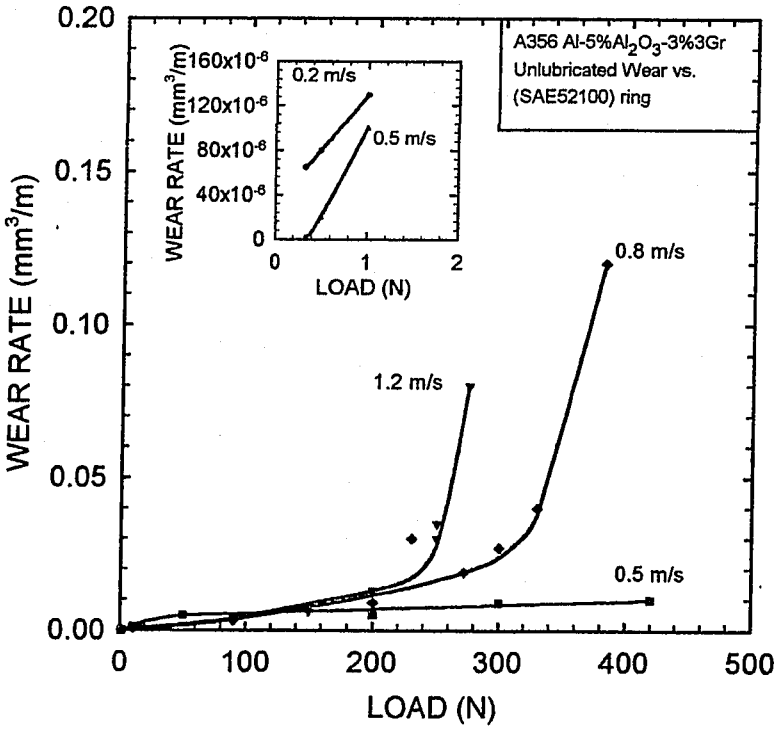

Fig. 4.1. (b) Wear rate versus applied load diagram at different sliding speeds for A356 Al-5%Al_2O_3-3%Gr.

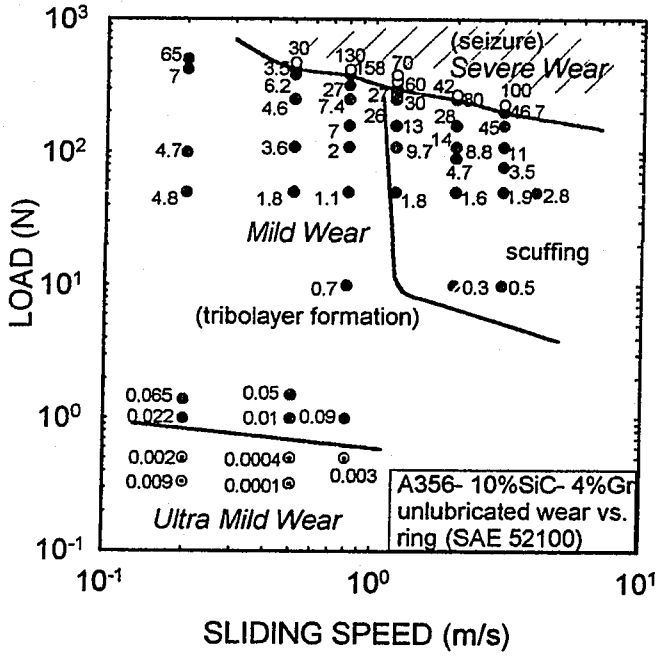

Fig. 4.2. (a) Wear map for the A356 Al-10%SiC-4%Gr composite worn against an SAE 52100 steel counterface. Three major wear regimes, namely, ultra mild, mild, and severe wear regimes are shown on the map. A scuffing sub-regime and a transient wear region between the mild and severe wear is also shown. Multiply the wear rates shown on the maps by 10^{-3} to find the measured wear rates in mm^3/m.

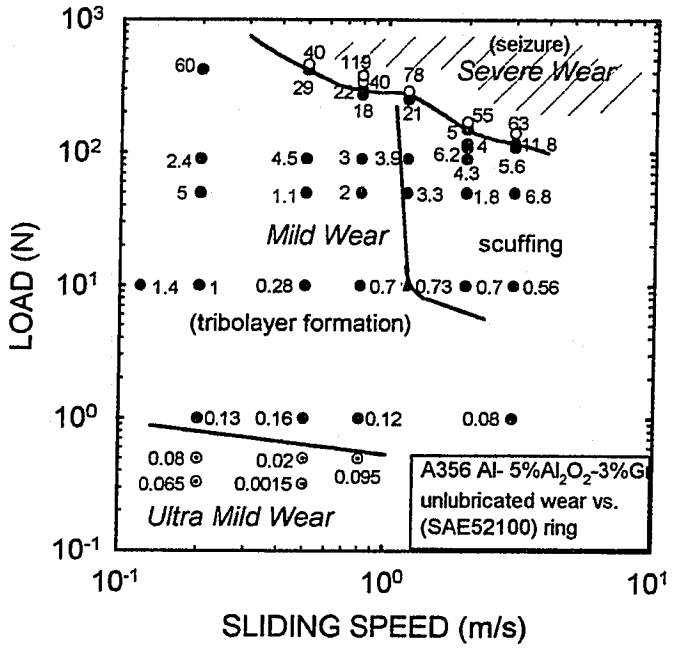

Fig. 4.2. (b) Wear map for the A356 Al- 5%Al_2O_3-3%Gr composite worn against an SAE 52100 steel counterface. Multiply the wear rates shown on the maps by 10^{-3} to find the measured wear rates in mm^3/m.

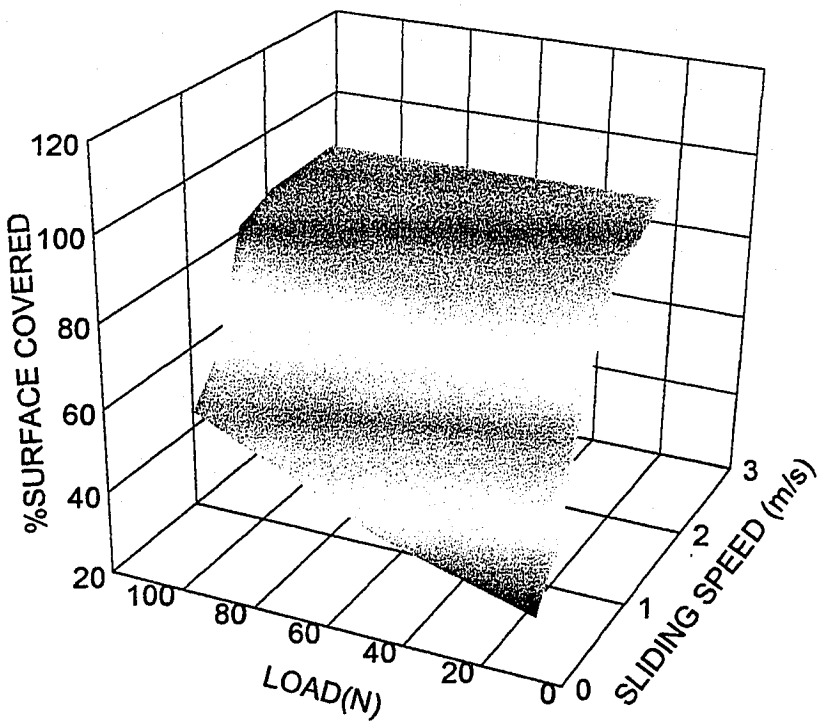

Fig. 4.3. (a) The increase of the percentage of the wear track covered by the tribo-layers with load and sliding speed for A356 Al-10%SiC-4%Gr.

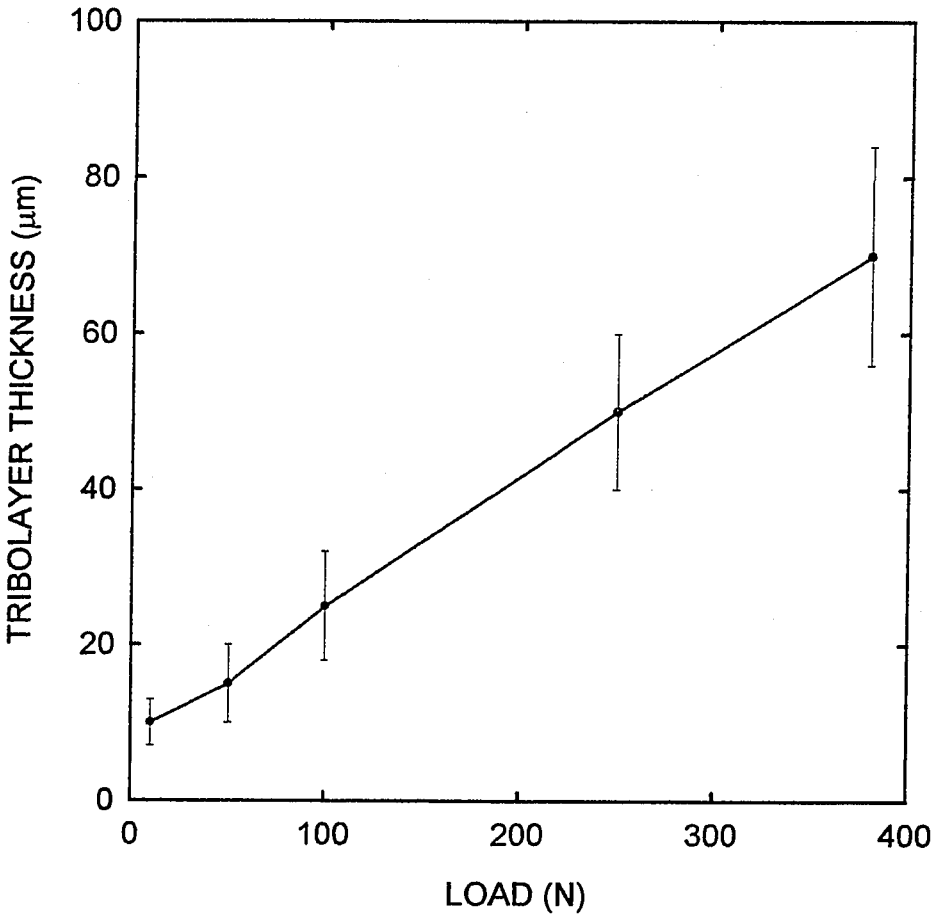

Fig. 4.3. (b) Variation of tribo-layer thickness with load at sliding speed of 0.8 m/s for A356 Al-10%SiC-4%Gr.

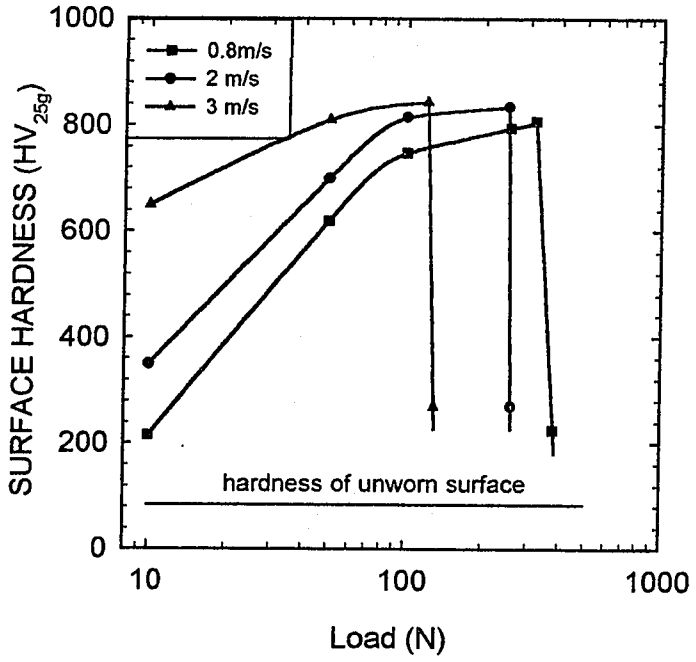

Fig. 4.3. (c) The increase of the hardness of the tribo-layers on A356 Al-10%SiC-4%Gr with load and sliding speed.

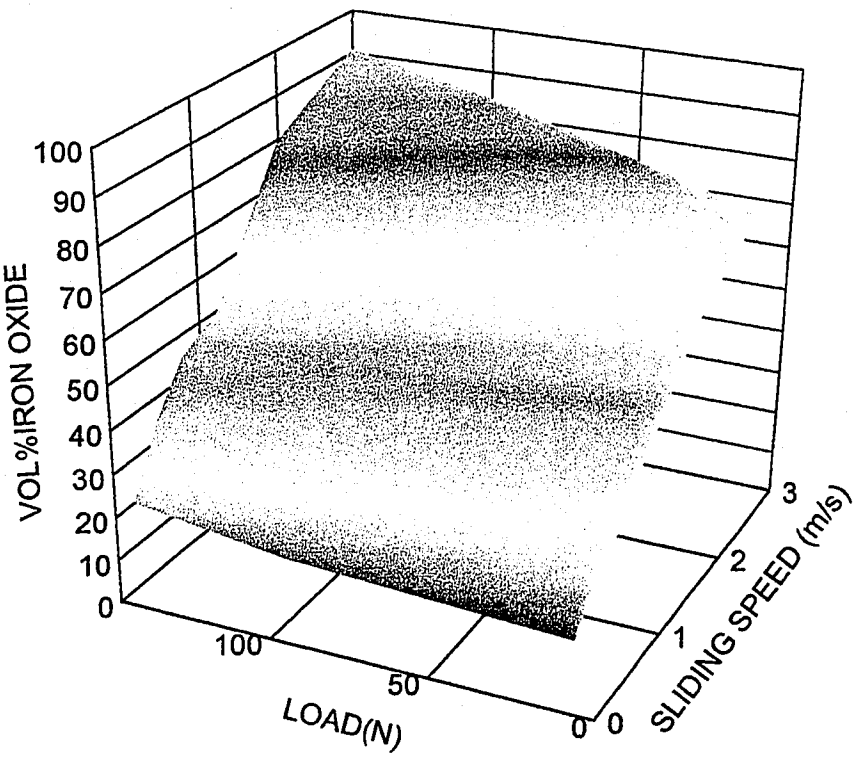

Fig. 4.3. (d) Variation of the concentration of iron oxide within the top 10% of the tribo-layer by increasing the load and sliding speed.

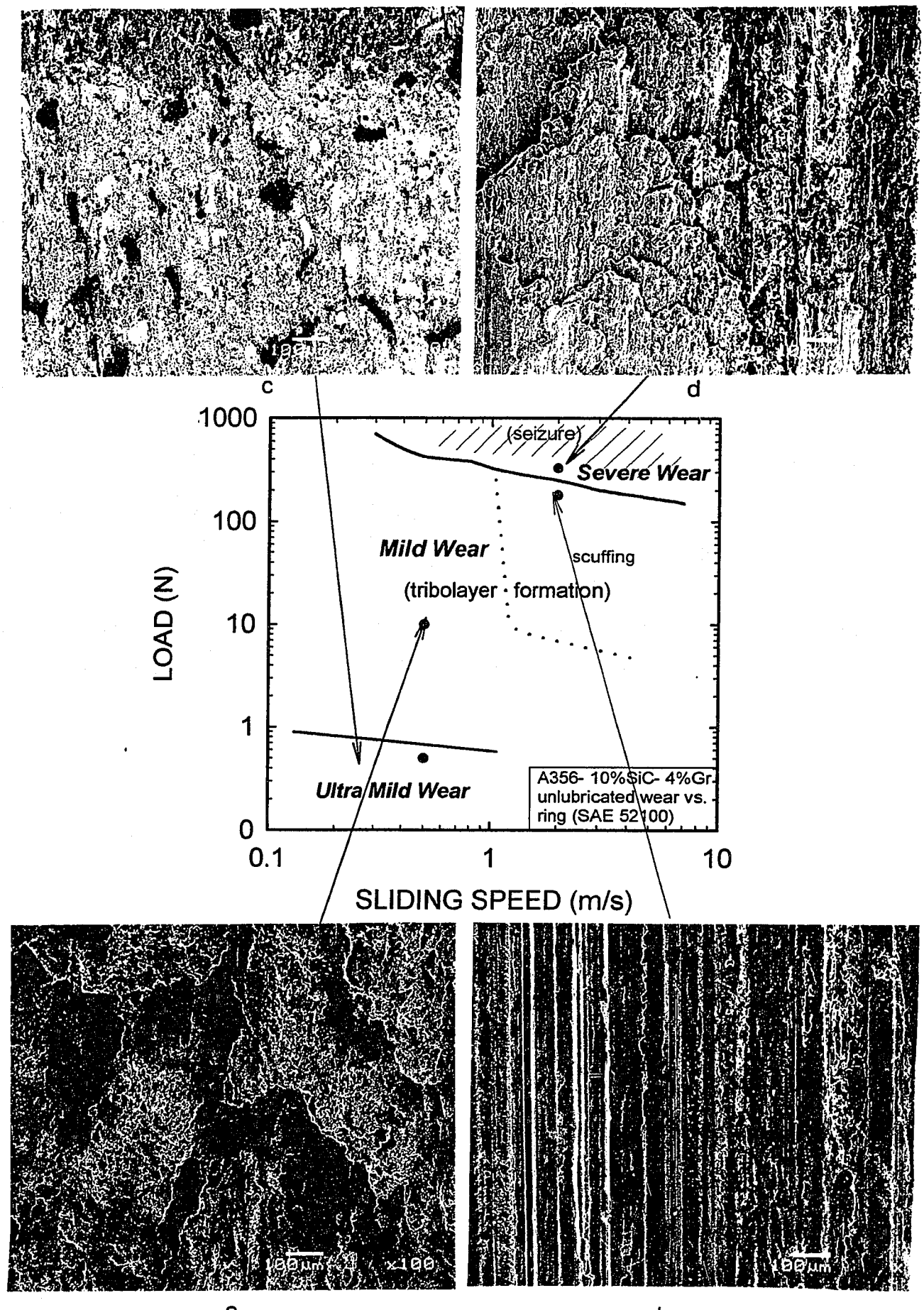
c
d
1000
100
10
1
0
LOAD (N)
(seizure)
Severe Wear
Mild Wear
(tribolayer formation)
scuffing
Ultra Mild Wear
A356- 10%SiC- 4%Gr.
unlubricated wear vs.
ring (SAE 52100)
0.1
1
10
SLIDING SPEED (m/s)
100µm
x100
100µm
a
b

Fig. 4.4

Fig. 4.4. Surface morphologies of A356 Al-10%SiC-4%Gr in three wear regimes marked on the wear map of the composite. (a) Secondary electron SEM micrograph of the worn surface at low sliding speed and load in the mild wear regime (10N, 0.5 m/s). The darker areas with flat surfaces are the tribo-layers. (b) the same as (a) but at high load and sliding speed (150N, 2 m/s). The wear track is entirely covered by the tribo-layers. (c) Back-scattered SEM micrograph in the ultra mild wear regime (0.5N, 0.5m/s). The upper top part shows the unworn surface. The worn surface is covered by a continuous layer of iron oxide (light coloured area). (d) Secondary electron SEM micrograph of the heavily worn surface in the severe wear regime where no tribo-layer is present (300 N, 2m/s).

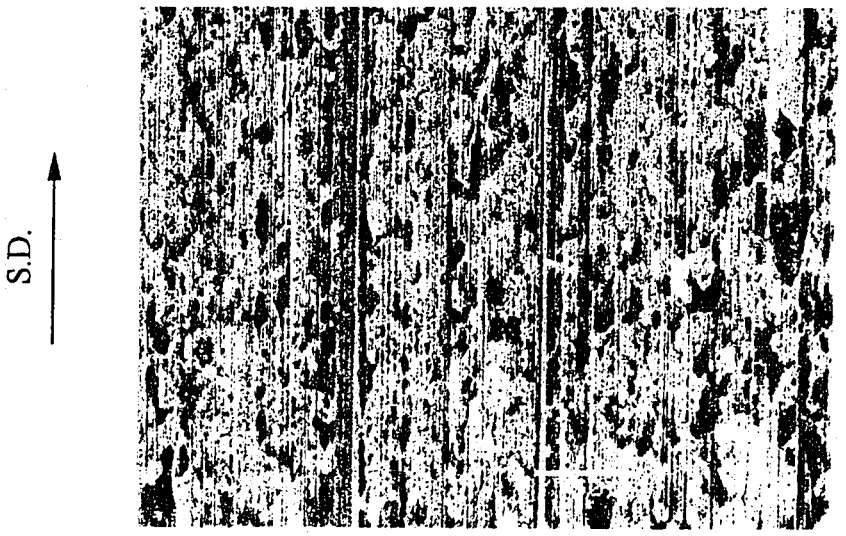

Fig. 4.5. The steel counterface exhibits long parallel scratches partially covered with iron oxide (at 0.5 N and 0.2 m/s).

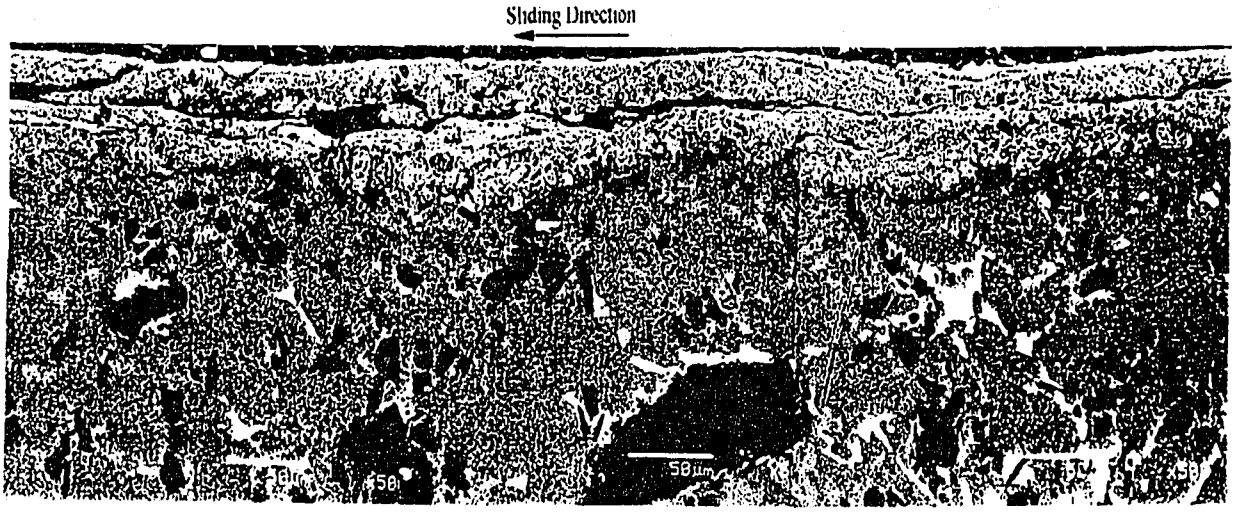

Fig. 4.6. (a) Back scattered SEM cross-sectional micrograph of the A356 Al-10%SiC-4%Gr sample worn at 159 N and 2.0 m/s, which shows a tribo-layer of about 30-50 µm thick, incorporating fragments of fractured SiC and $NiAl_3$ intermetallic particles mixed with iron oxide. Notice the thin layer of iron oxide (2-3 µm arrow) adjacent to the contact surface (light film) and graphite films (dark) within the tribo-layer.

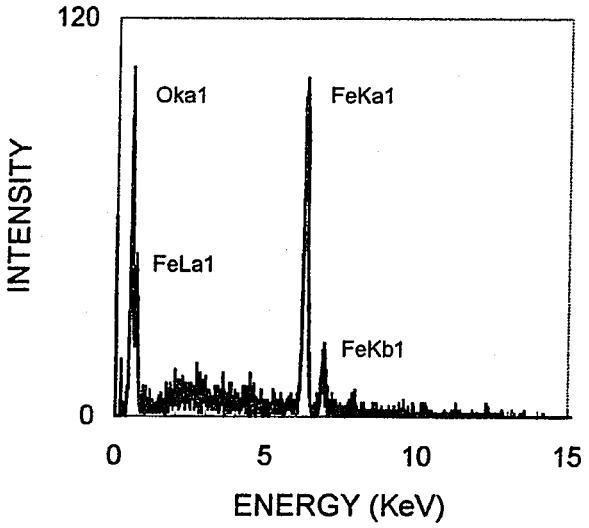

Fig. 4.6. (b) The EDS analysis of the oxide layer on the top surface of Fig. (a) confirms that it is comprised of Fe and O.

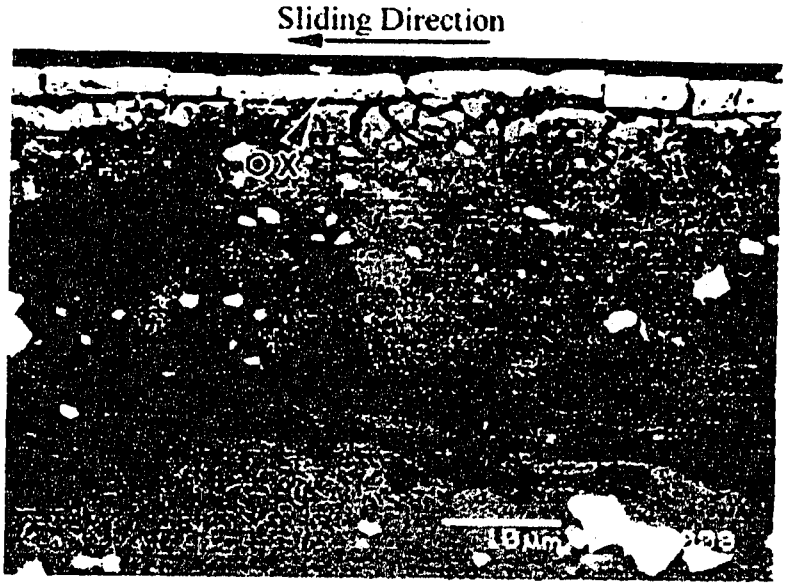

Fig. 4.7. Back scattered SEM micrograph of the cross-section of the A356 Al-10%SiC-4%Gr worn at 159 N and 2.0 m/s. The micrograph shows the iron oxide layer on the top surface (light coloured) of the tribo-layer. The sample was hot mounted by polymer.

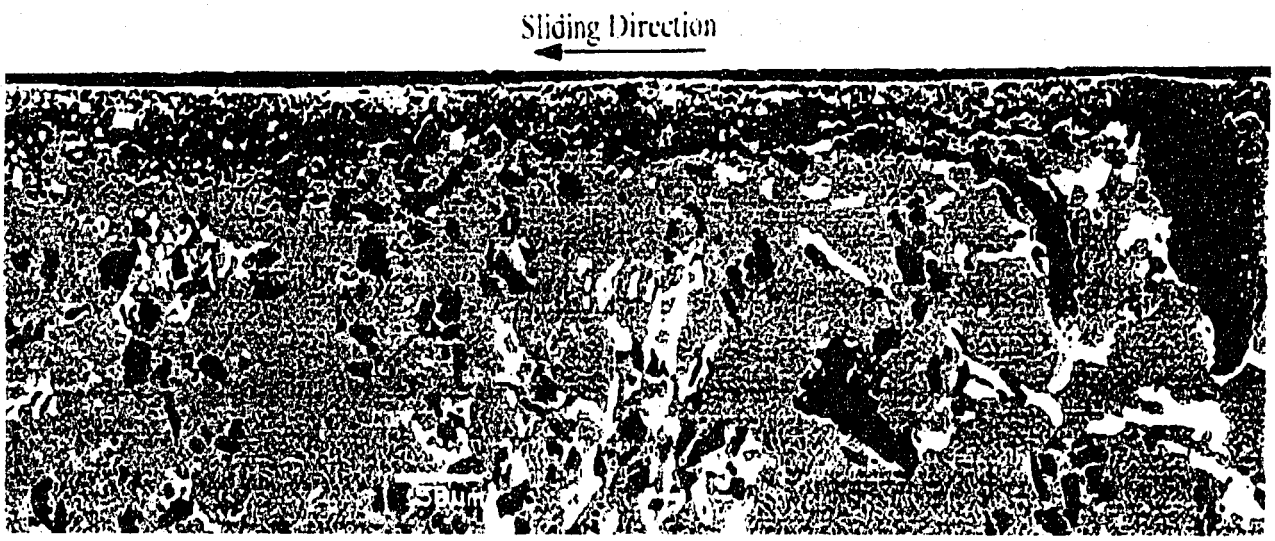

Fig. 4.8. (a) Back scattered SEM micrograph of the cross-section of the A356 Al-10%SiC-4%Gr sample worn at 159 N and 2.0 m/s. The cross-section shows how the graphite films were formed from the graphite particles beneath the contact surface.

Fig. 4.8. (b) A high magnification image of the tribo-layer shows the lamellar structure formed by several graphite films running parallel to each other.

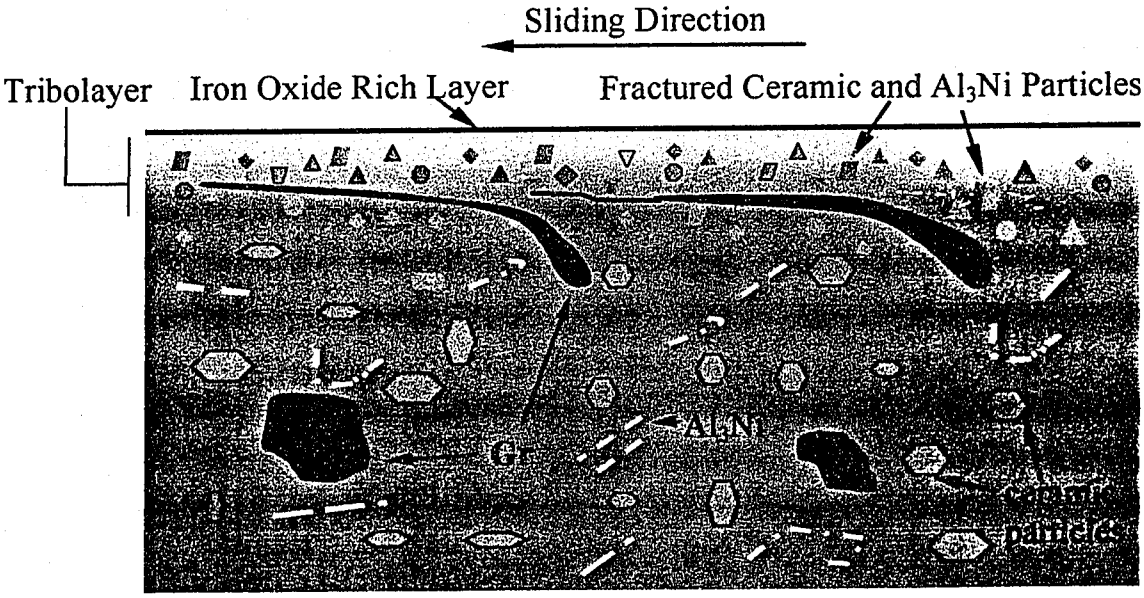

Fig. 4.9. A schematic representation of the main constituents of the tribo-layers in graphitic metal matrix composites. The topmost part is a layer rich in iron oxide. Fractured ceramic particulates and Al_3Ni intermetallics are mixed with an Al matrix. The graphite particles just beneath the contact surface are elongated in the sliding direction and embedded in the tribo-layer. The material under the tribo-layer remains relatively damage-free.

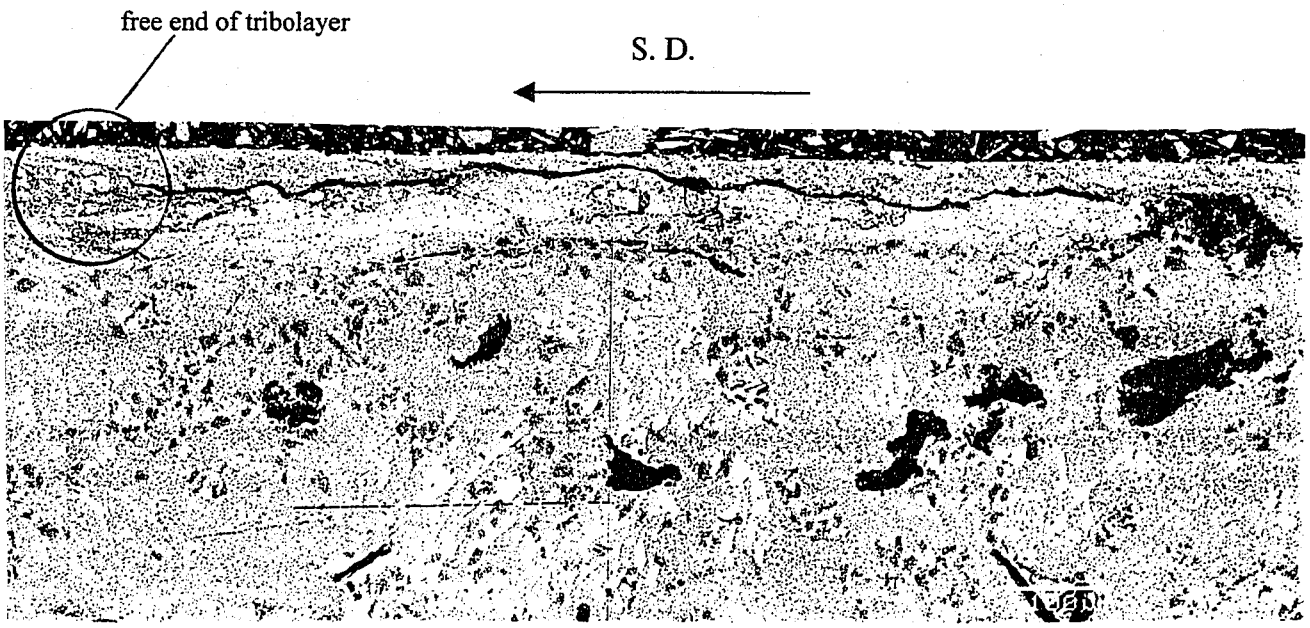

Fig. 4.10. The tribo-layer with no support at the end for the A356 Al-10%SiC-4%Gr composite worn at 200 N and 2.0 m/s.

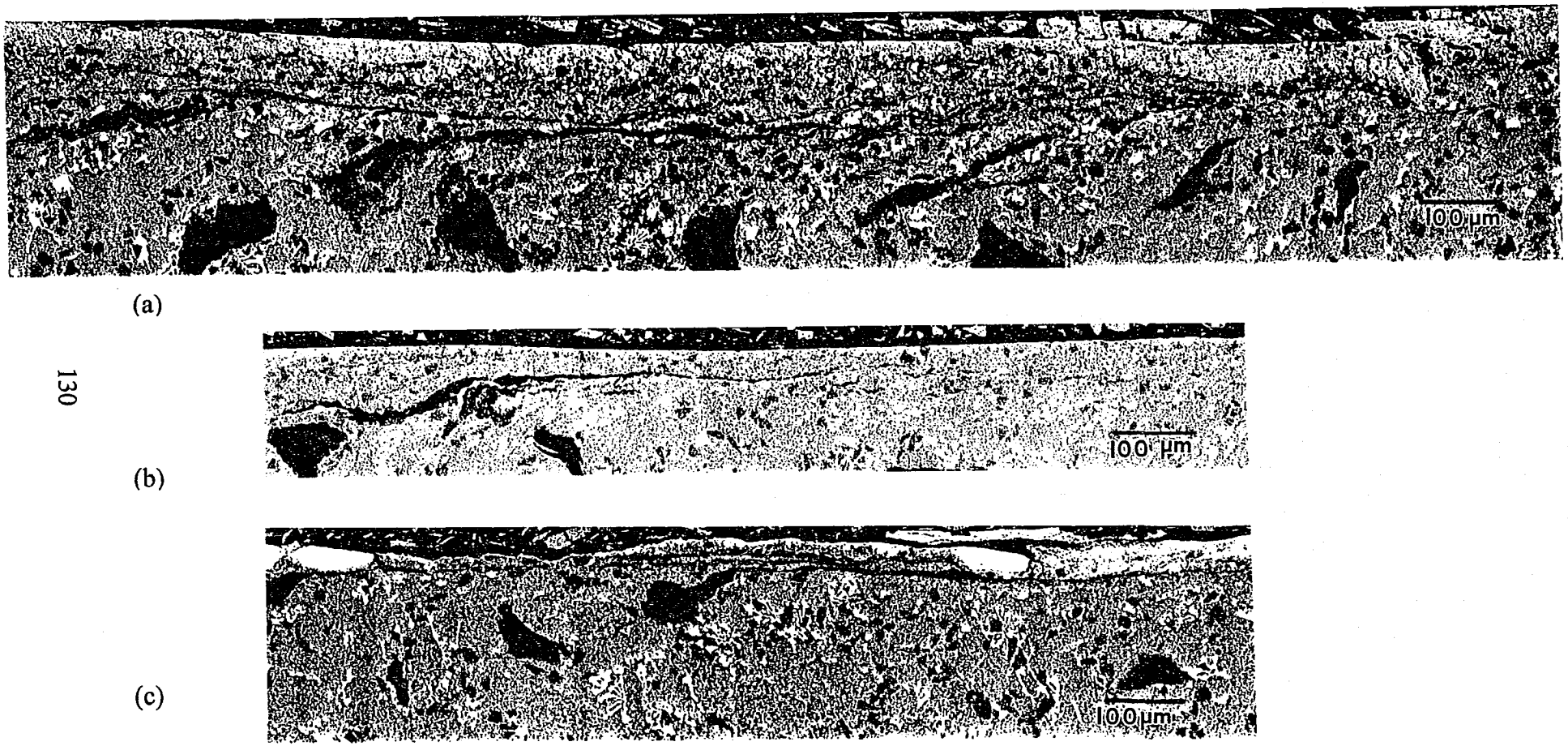

Fig. 4.11. The graphite film lengths remained constant at about 0.7 mm for loads of (a) 150 N, (b) 50 N, and (c) 20 N, at sliding velocity of 2m/s.

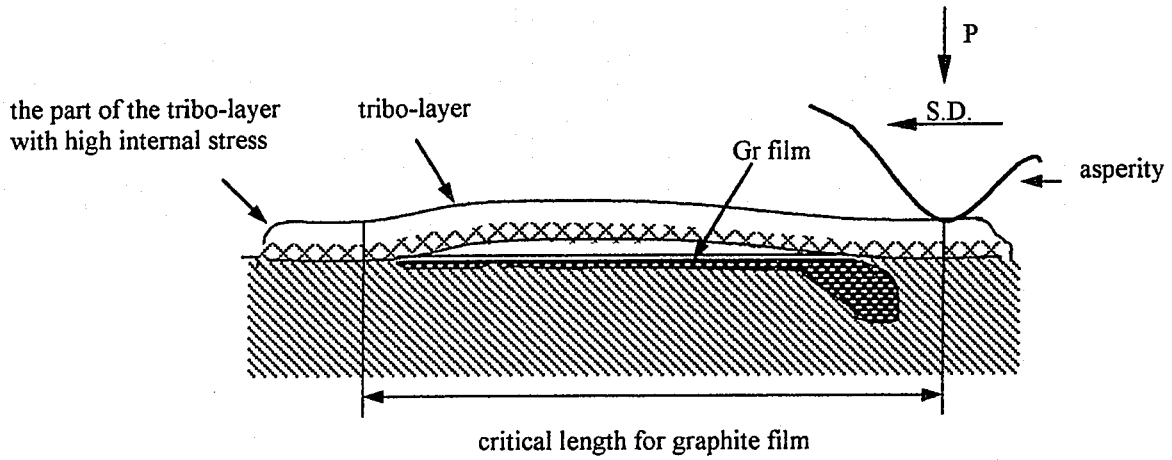

Fig. 4.12. Schematic presentation of buckling of the tribo-layer by the friction force of an asperity.

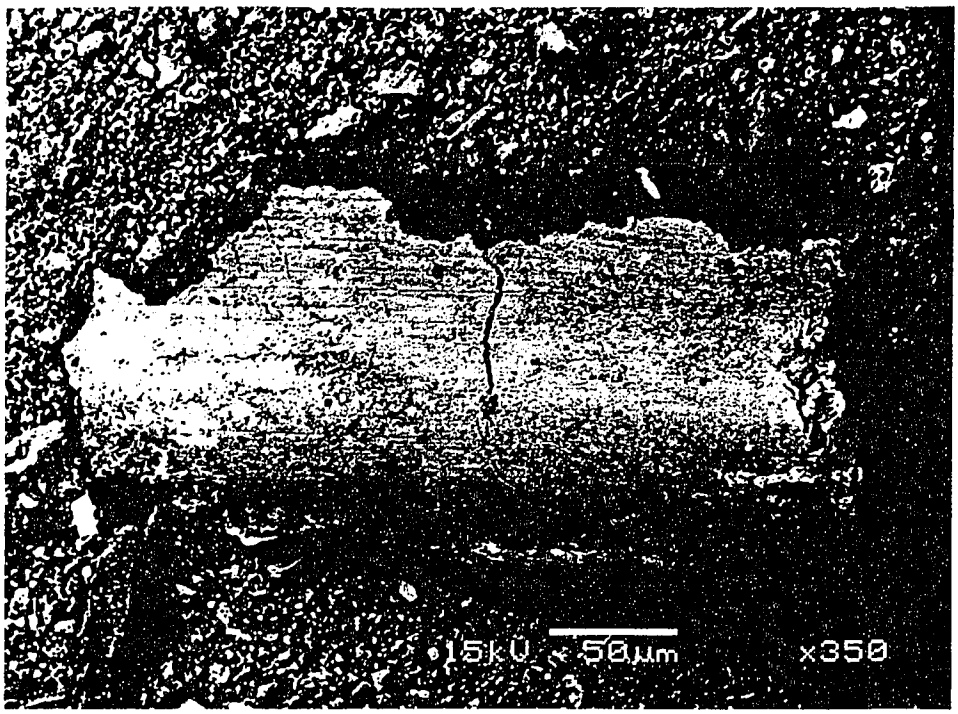

Fig. 4.13. (a) SEM micrograph of the debris shows that the maximum length of the delaminated tribo-layer is less than 0.2 mm.

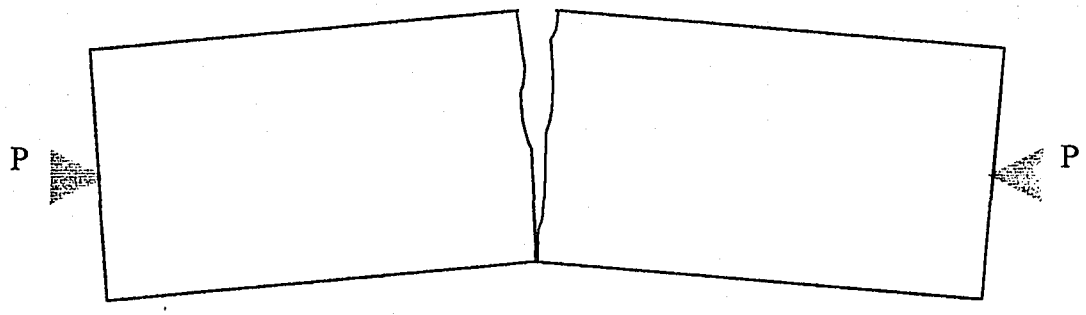

(b) buckled tribo-layer broken in two segments

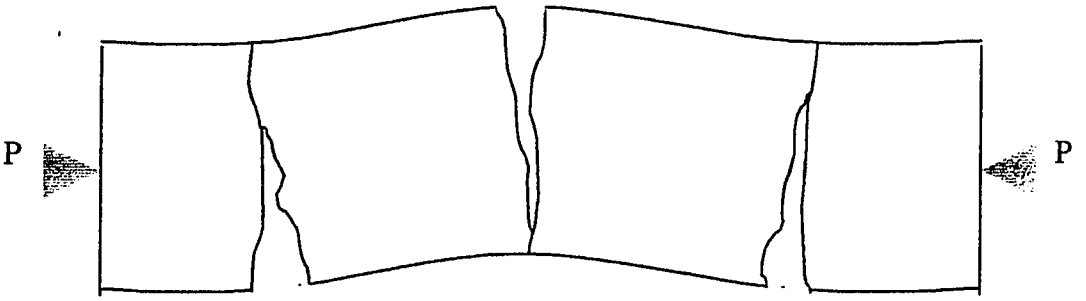

(c) buckled tribo-layer broken into four segments

Fig. 4.13. (continue) The buckling process may divide the tribo-layer into (b) 2 or (c) 4 segments.

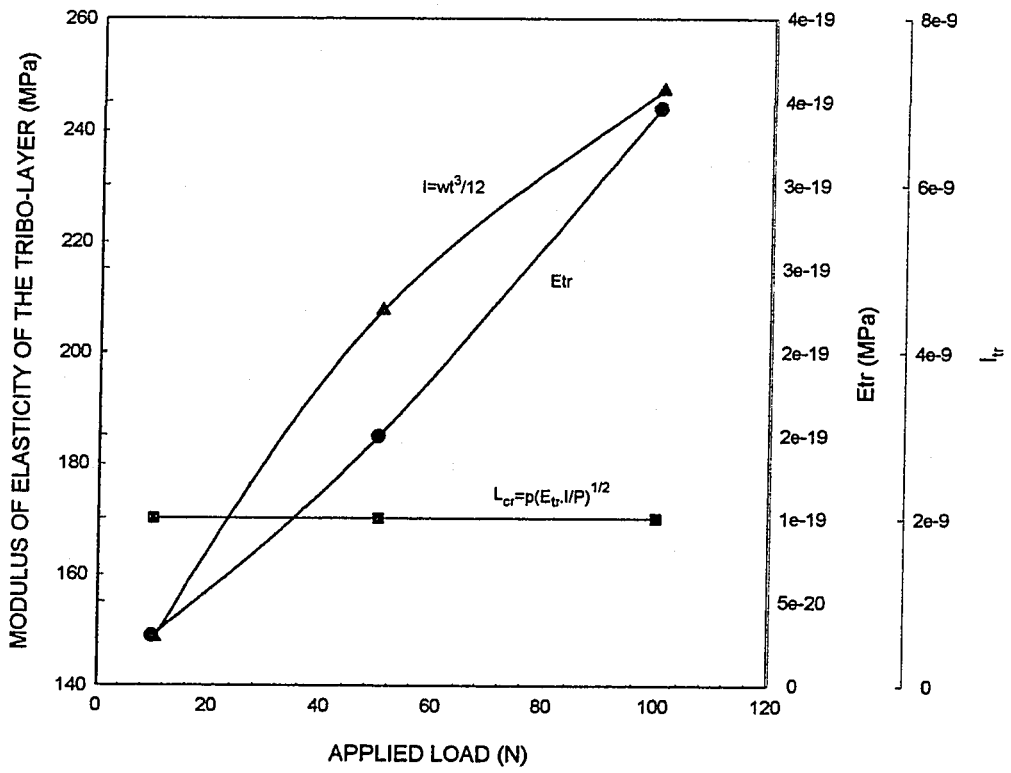

Fig. 4.14. Variation of E_{tr}, I_{tr}, and L_{cr} with the aplied load at 3 m/s for A356 Al-10%SiC-4%Gr

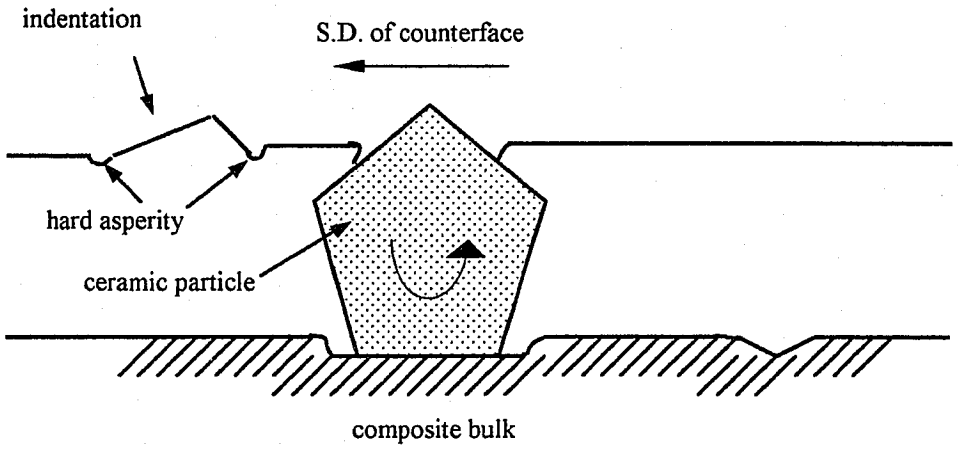

(a)

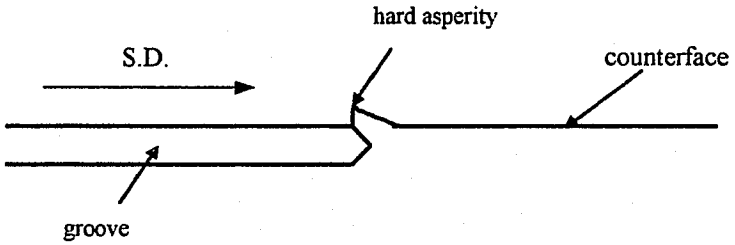

(b)

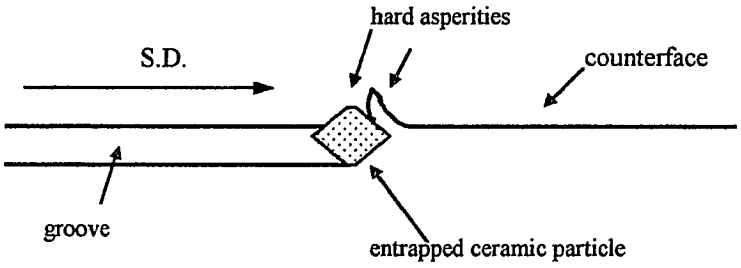

(c)

Fig. 4.15. (a) The hard particle may act as three body abrasives against the steel counterface and leave hard asperities on the steel counterface behind. (b) it cuts a longitudinal groove on the contact surface of the counterface and (c) may occasionally become entrapped at the end of a groove.

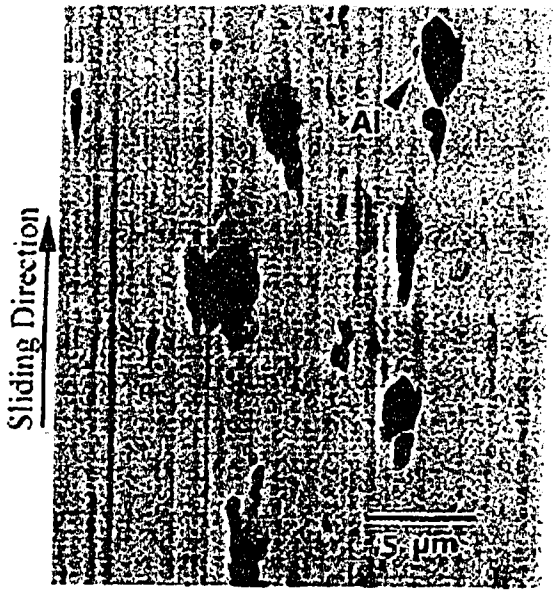

Fig. 4.16. (a) Back scattered SEM micrograph of the 52100 steel counterface worn at 50 N and 3.0 m/s showing the initial stage of aluminum transfer from the A356 Al-10%SiC-4%Gr to the contact surface of the steel..

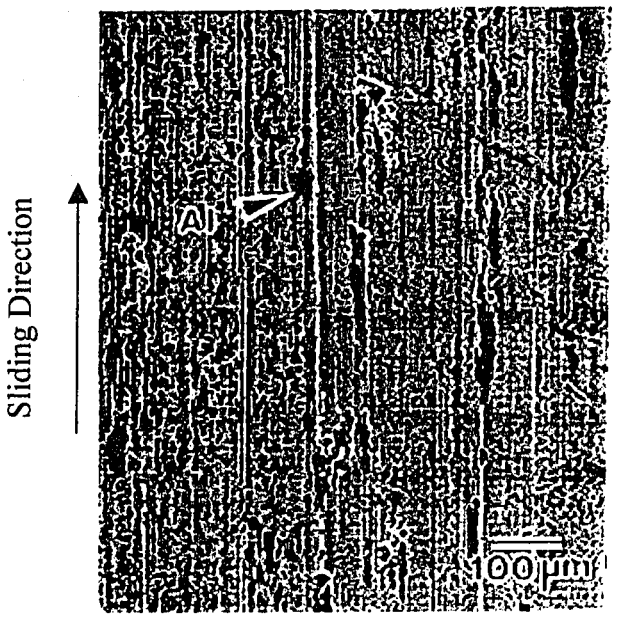

Fig. 4.16. (b) Secondary electron SEM micrograph of the worn 52100 steel counterface at a load of 10 N and a sliding speed of 3.0 m/s. The transferred aluminum particles first accumulate in the leading front of a hard asperity, then spread backward as their width and lengths increase.

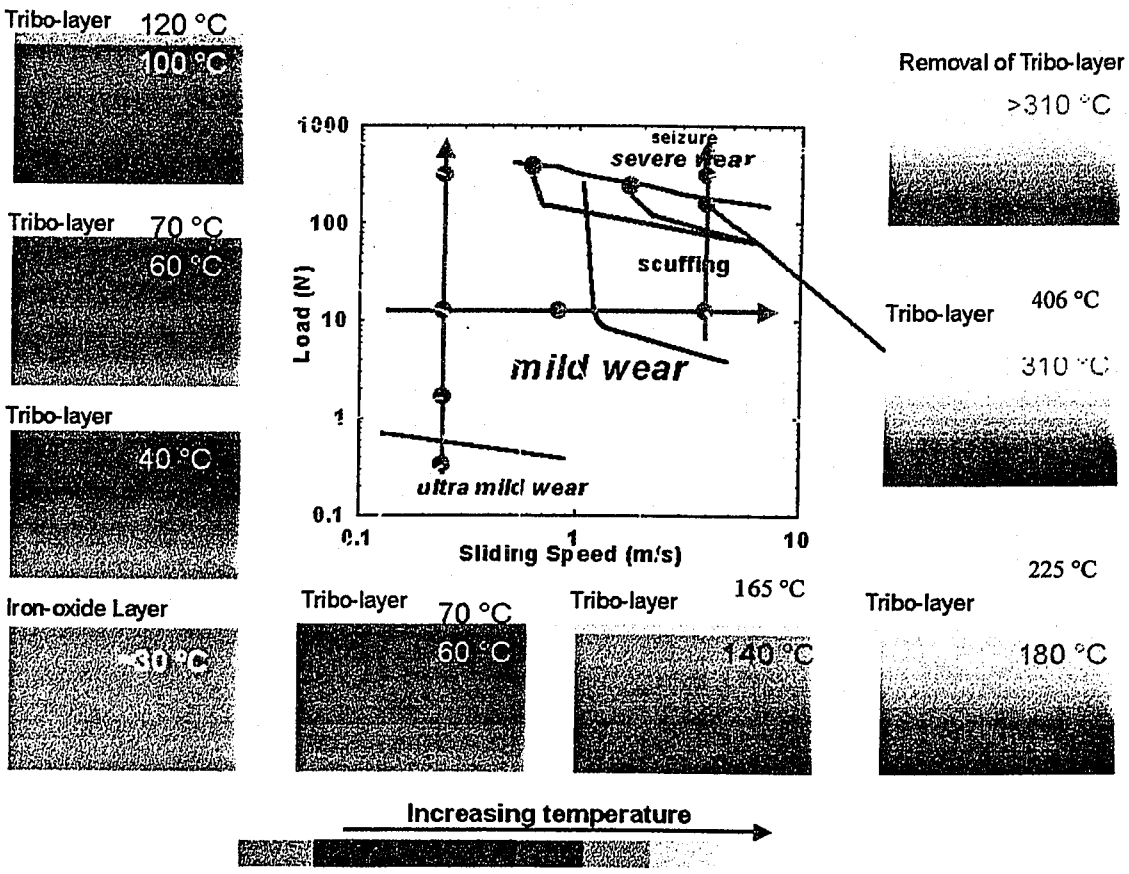

Fig. 4.17. The variation of temperature at various loading conditions for A356 Al-10%SiC-4%Gr. Constructed based on the measured bulk temperature and calculated tribo-layer temperature (see appendix II).

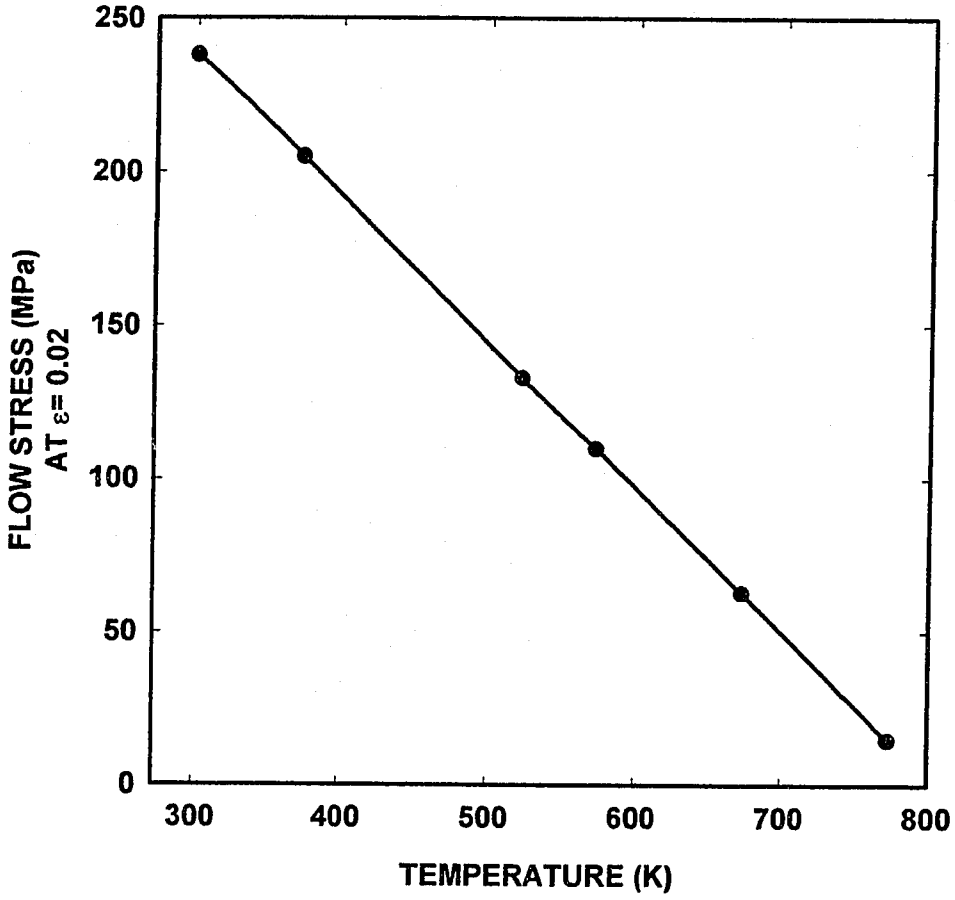

Fig. 4.18. The yield strength of the A356 Al-10%SiC-4%Gr composite vs. temperature.

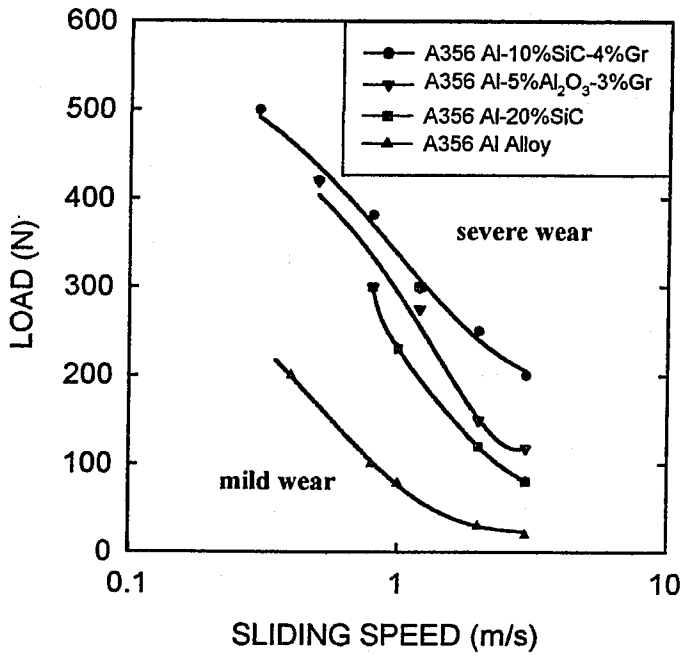

Fig. 4.19. Comparison of the mild to severe wear transition boundaries of the graphitic A356 Al-10%SiC-4%Gr and A356 Al-5%Al_2O_3-3%Gr with those of the non-graphitic composite A356 Al-20%SiC and the unreinforced matrix A356 Al alloy.

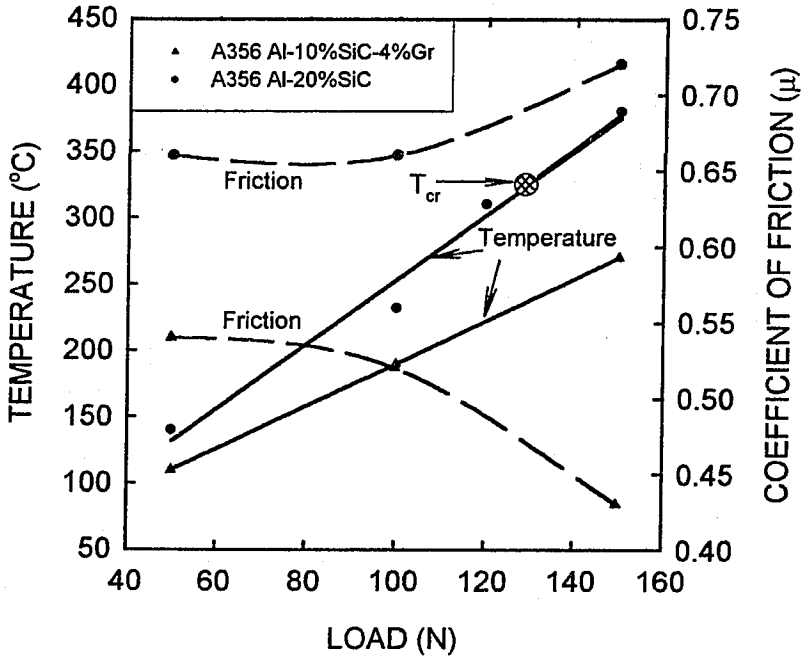

Fig. 4.20. The bulk temperatures and the coefficients of friction (dotted lines) of the graphitic A356 Al-10%SiC-4%Gr and non-graphitic A356 Al-20%SiC as a function of load at a sliding speed of 2.0 m/s. The coefficient of friction of A356 Al-20%SiC is higher for all the loading conditions. The difference in the coefficients of friction of the A356 Al-10%SiC-4%Gr and A356 Al-20%SiC increases by increasing the load. The bulk temperature of A356 Al-20%SiC is also higher and reaches the critical transition temperature T_c of 328° C at 130 N while A356 Al-10%SiC-4%Gr is still in the mild wear regime.

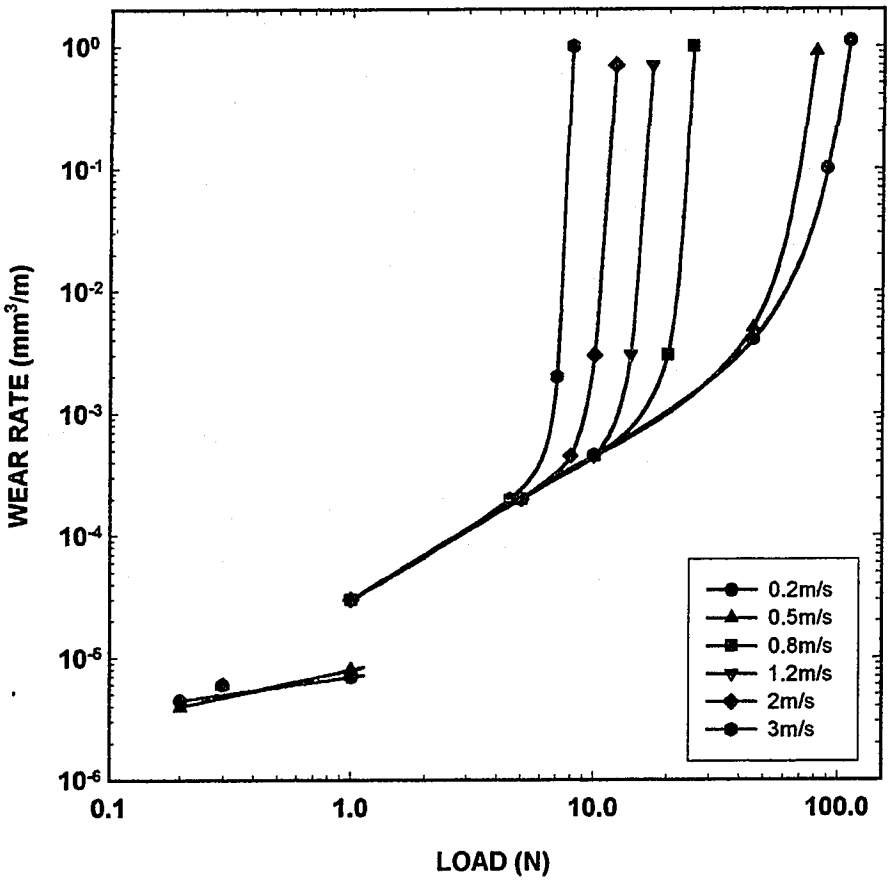

Fig. 5.1. Wear rate versus load curves at various sliding speeds, for grey cast iron. The variation of wear rate vs. load remains linear from 1N to 5 N for all sliding speeds.

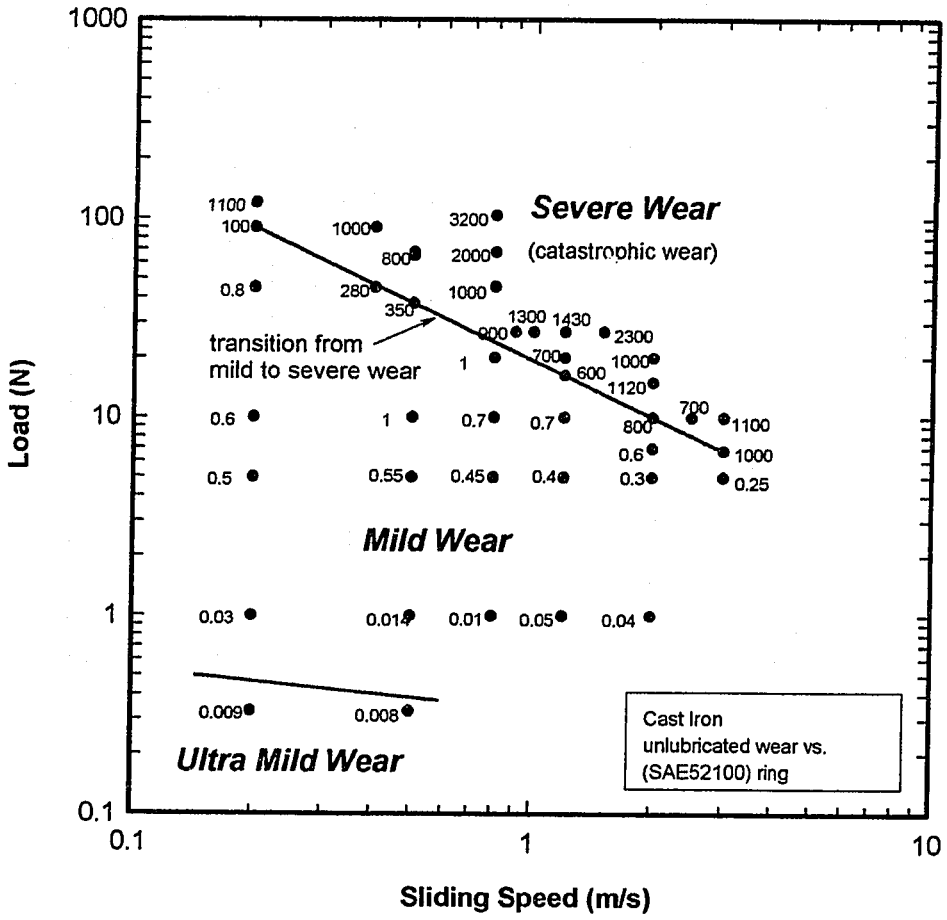

Fig. 5.2. The wear map constructed for the grey cast iron. Three major wear regimes: namely, ultra mild, mild and severe, are depicted on the map. Multiply the wear rates shown by 10^{-3} to find the measured wear rates in mm^3/m.

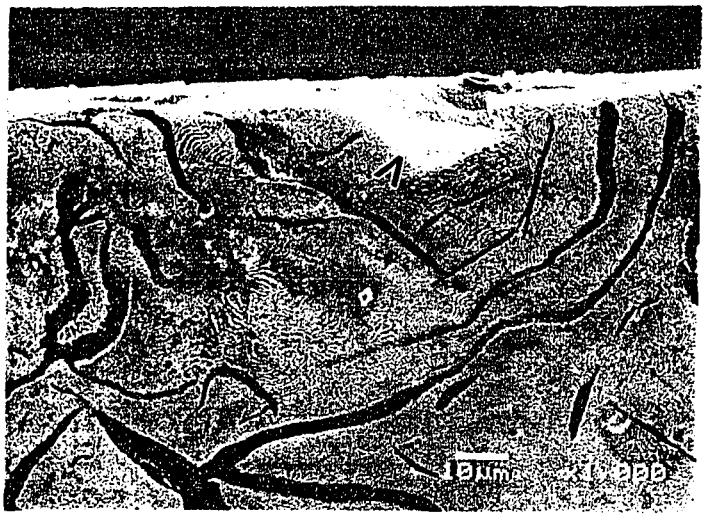

Fig. 5.3. (a) The morphology formed as a result of a failed neck on the cross section of the grey cast iron sample in the mild wear regime (arrow).

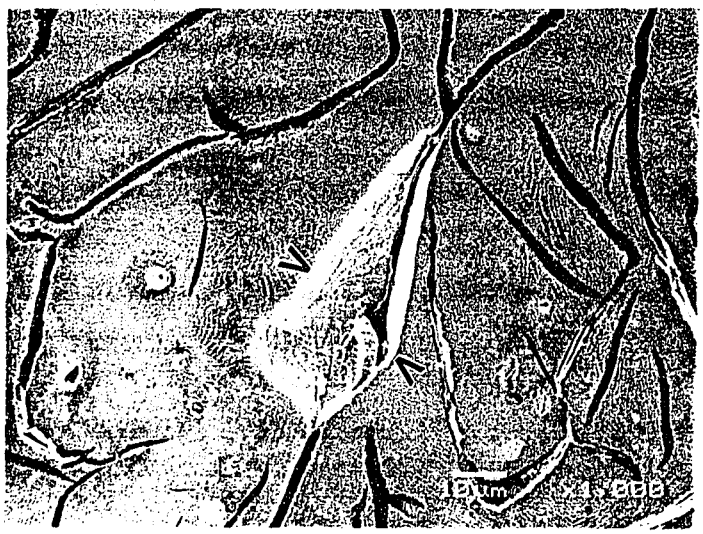

Fig. 5.3. (continue) (b) the morphology formed as a result of a failed neck on the polished surface marked by arrows (similar to the ultra mild regime).

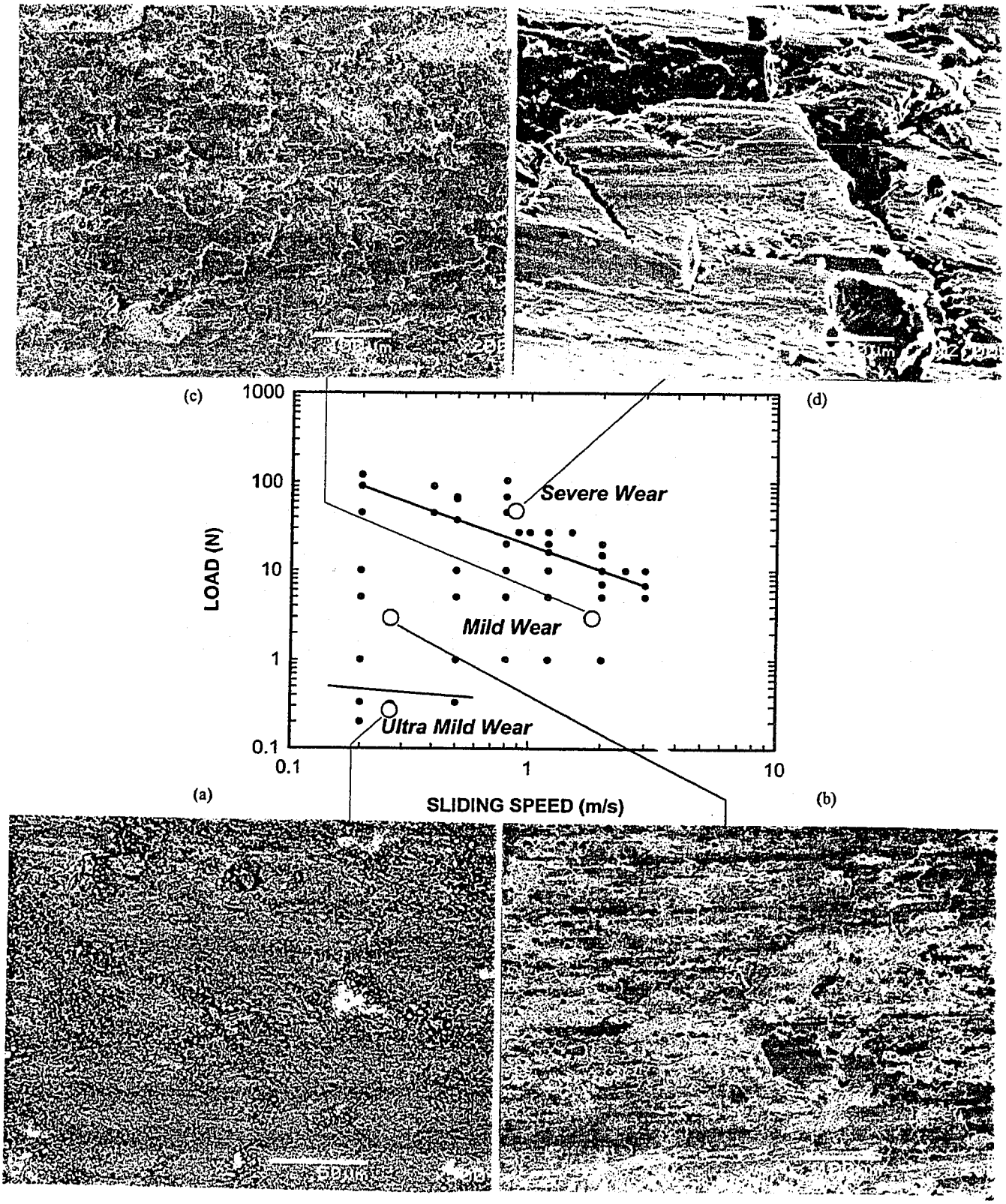
(c)
(d)
1000
100
10
1
0.1
LOAD (N)
Severe Wear
Mild Wear
Ultra Mild Wear
0.1
1
10
SLIDING SPEED (m/s)
(a)
(b)

Fig. 5.4.

Fig. 5.4. The surface morphologies of grey cast iron in (a) ultra mild regime, (b) mild regime at low loads and sliding speeds, (c) mild regime at high loads and sliding speeds and (d) severe wear regime.

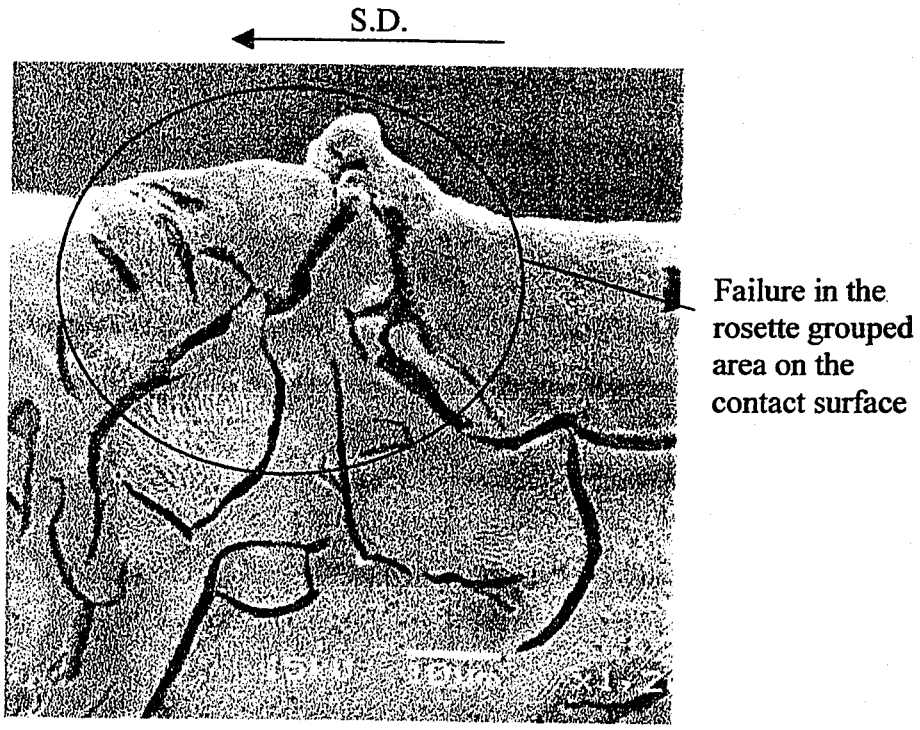

Fig. 5.5. Rosette grouped graphite flakes cause the cast iron to collapse readily at those points.

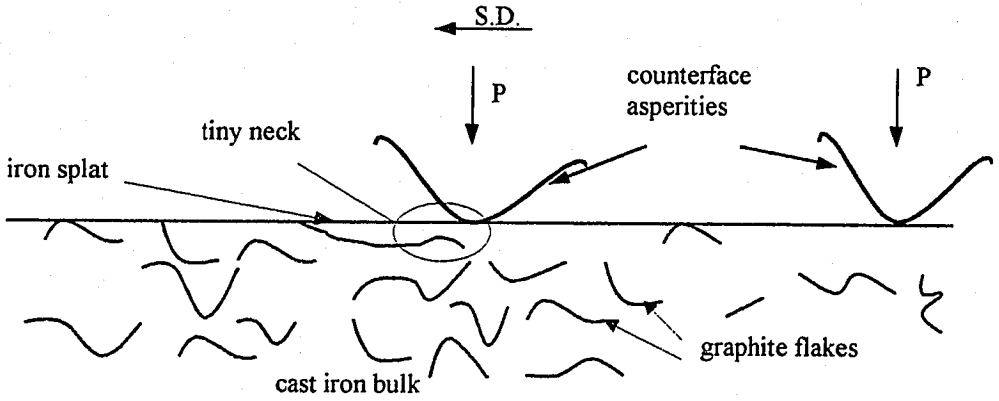
S.D.
P
counterface
asperities
P
tiny neck
iron splat
graphite flakes
cast iron bulk

(a)

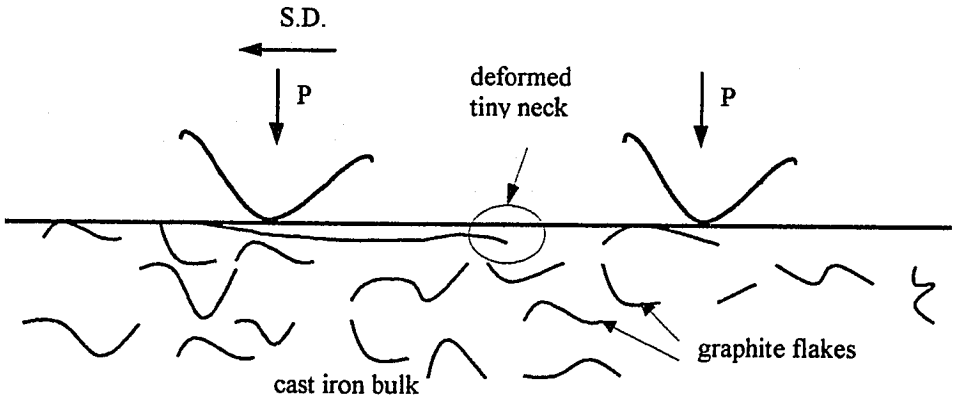
S.D.
P
deformed
tiny neck
P
graphite flakes
cast iron bulk

(b)

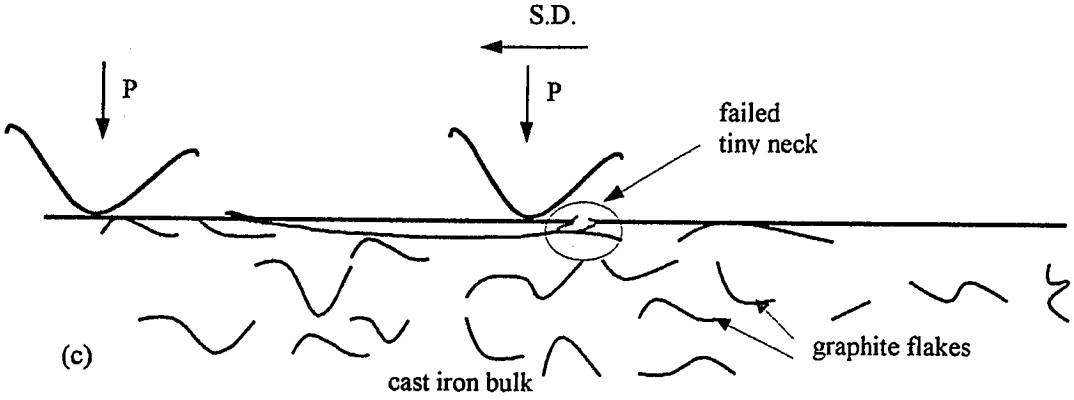
S.D.
P
P
failed
tiny neck
graphite flakes
cast iron bulk

(c)

Fig. 5.6

Fig. 5.6. (continue) Schematic presentation of failure of the necks (a to c) caused by tensile deformation resulting from friction forces.

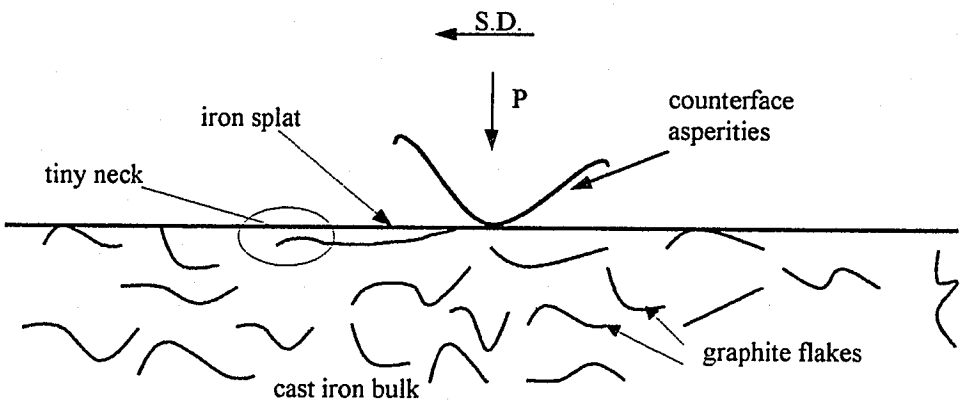

(a)

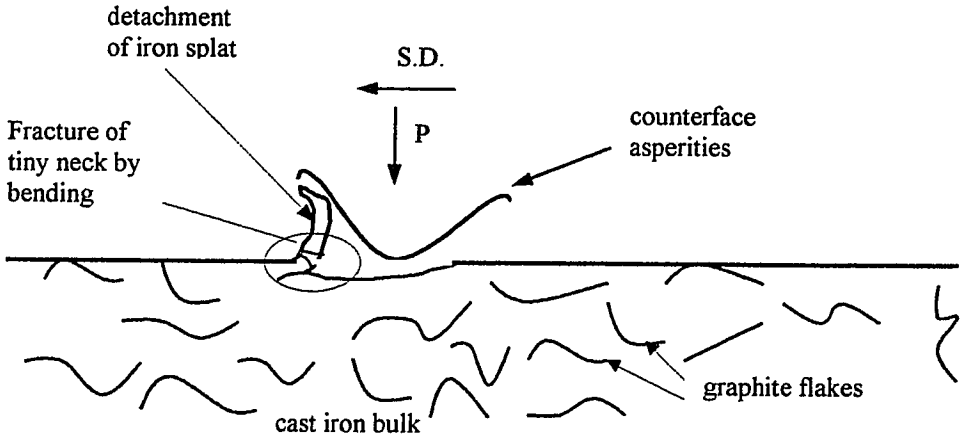

(b)

Fig. 5.7. Schematic presentation of failure of the necks (a and b) by bending of an iron splat over the neck.

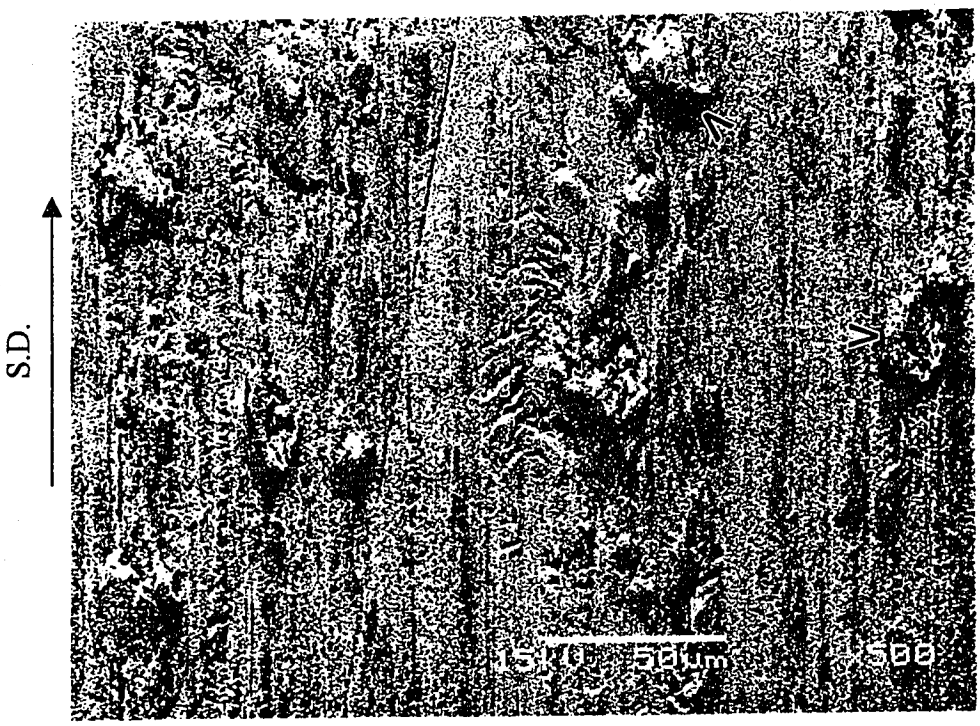

Fig. 5.8. The local transferred materials (grey cast iron) to the steel counterface grow up to 10 µm height, 40 µm long and 20 µm wide.

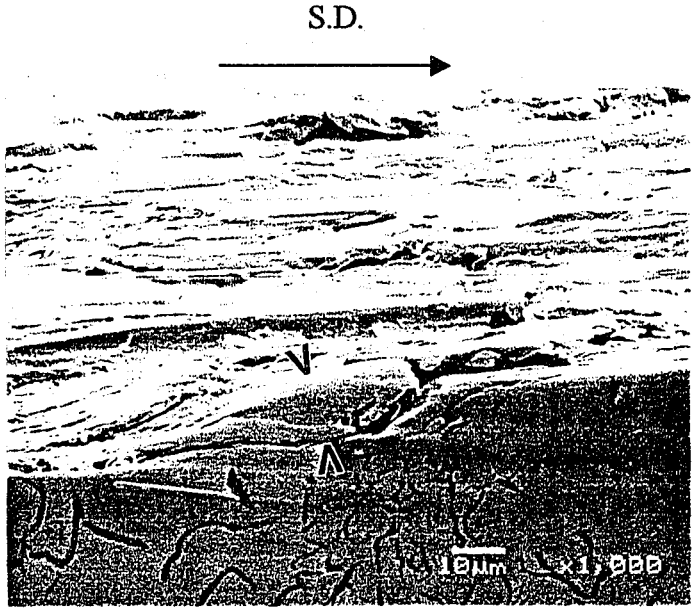

Fig. 5.9. Severe deformation at the worn surface of grey cast iron at 15.0 N 2.0 m/s (in the severe regime). A large fragment of cast iron on the edge (marked by arrow) is about to separate.

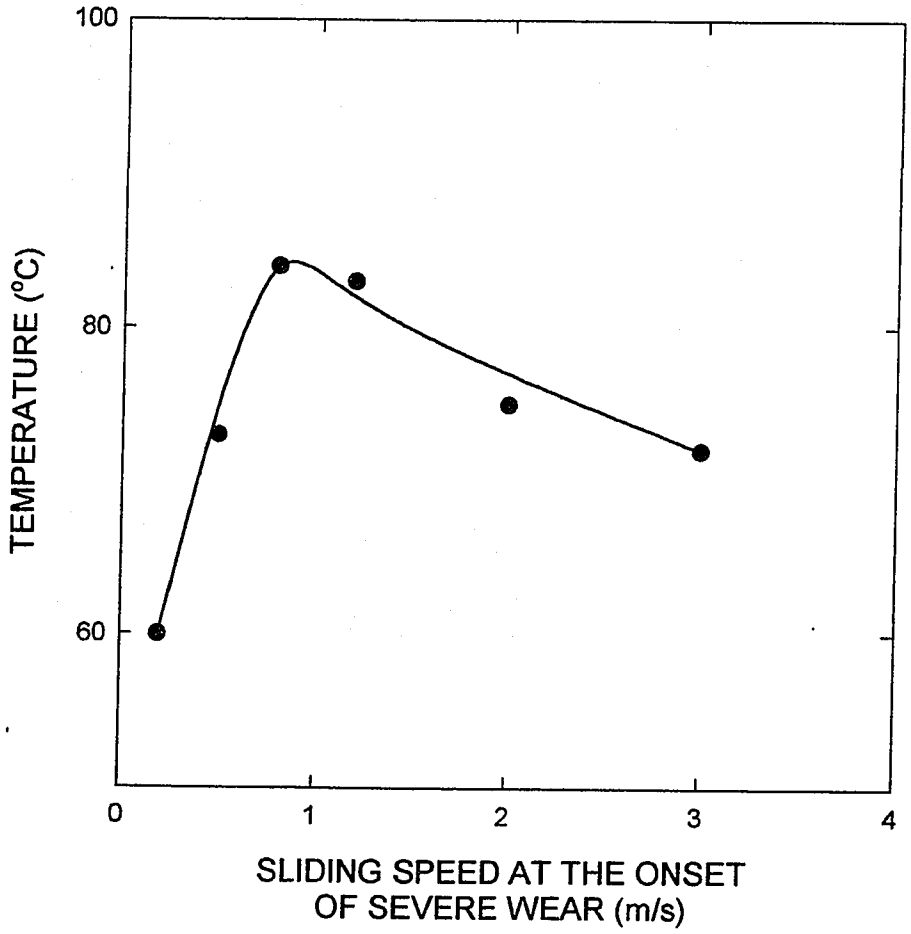

Fig. 5.10. The variation of temperature versus load at the onset of severe wear.

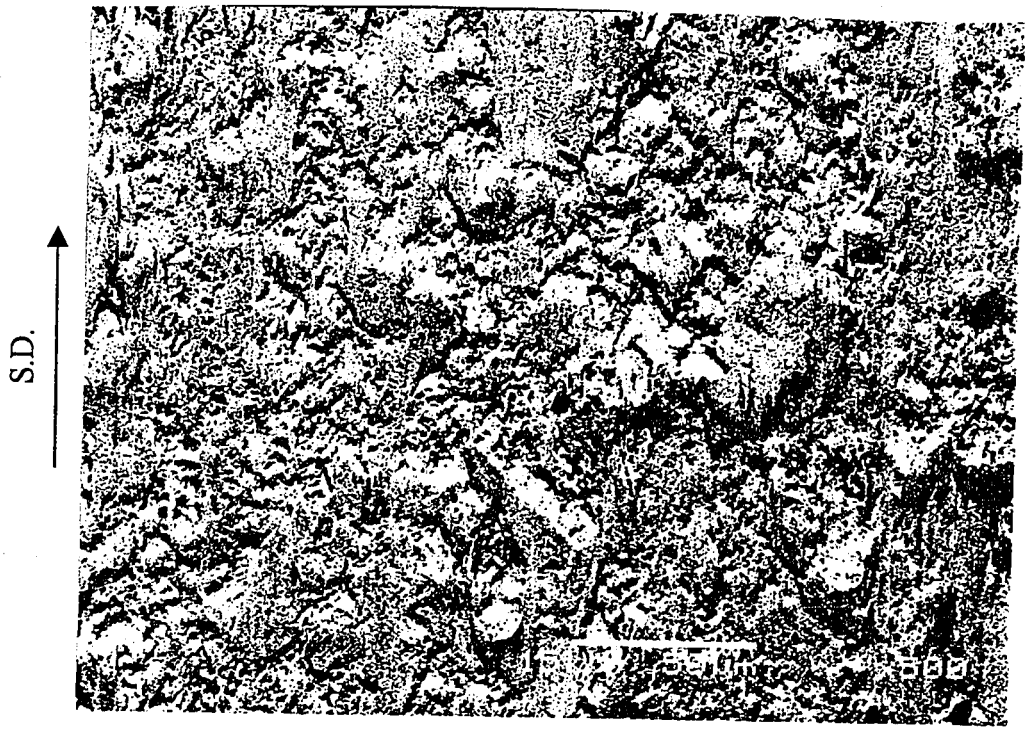

Fig. 5.11. The local material transfer process (in the severe wear regime) in dry sliding of grey cast iron against a steel counterface repeats itself, and covers all the counterface at a short sliding distance (5 m).

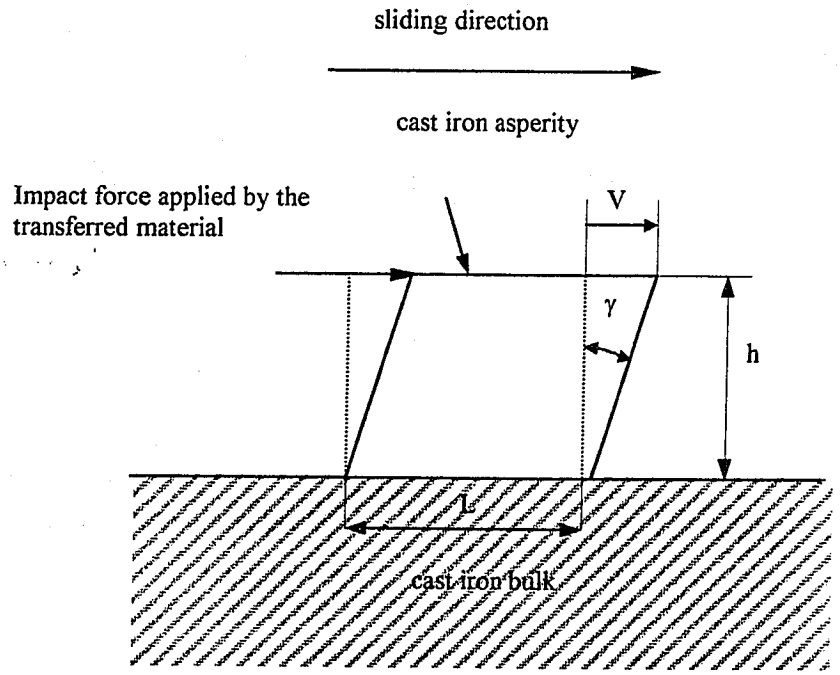

Fig. 5.12. A simple model of an asperity for estimating the strain rate in the severe wear regime for gray cast iron. where L is the width of asperity, V the sliding speed, γ the shear angle, and h the height of the asperity.

Fig. 5.13. The sharp edges of debris (marked by arrow) on grey cast iron in the severe regime indicate the brittle fracture of large asperities in this regime.

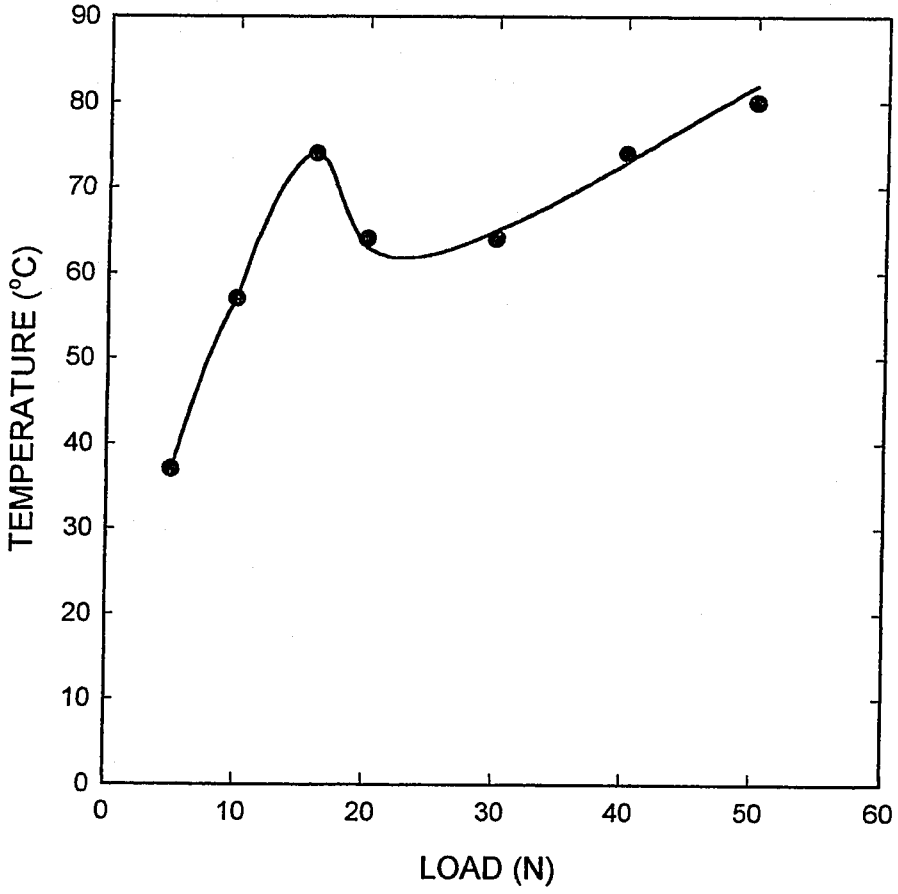

Fig. 5.14 The trend of temperature increase by increasing the load at 1.2 m/s shows that as soon as severe wear occurred, the bulk temperature dropped from 70 °C to 55 °C then increases with load with a different slope.

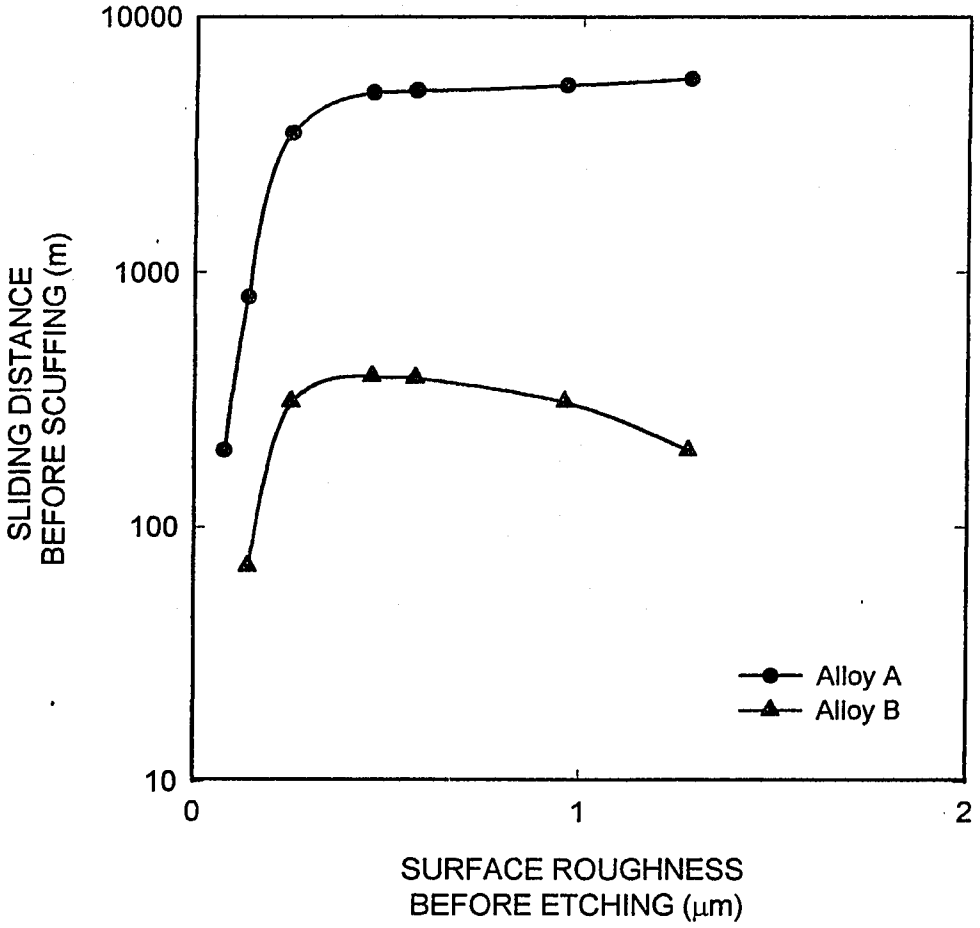

Fig. 6.1. The effect of surface roughness prior to etching on wear for Al-Si alloys A and B.

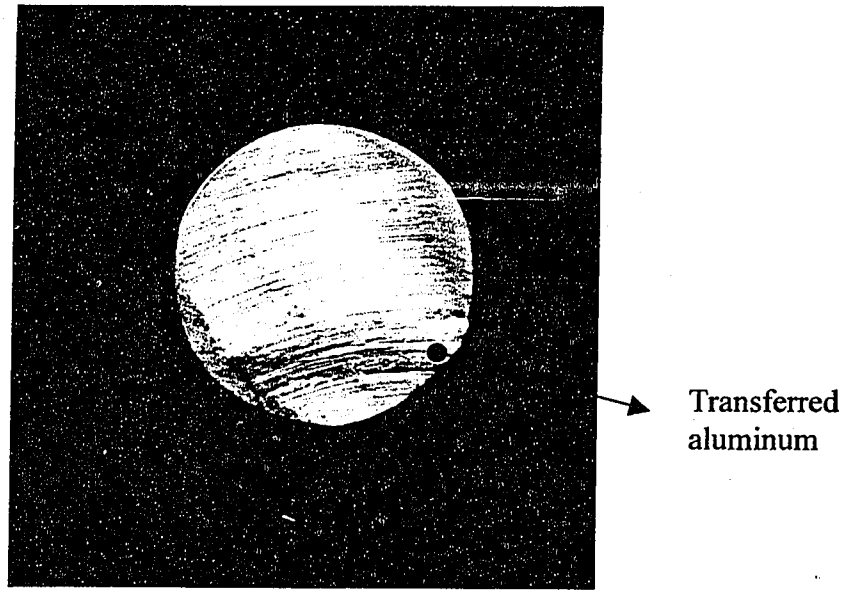

Fig. 6.2. Scuffing of Al-Si alloy B on the M2 tool steel counterface. The roughness of alloy B before the test was 0.4 μm when etched by 10% NaOH for 7 minutes. It shows the aluminum transferred to the counterface.

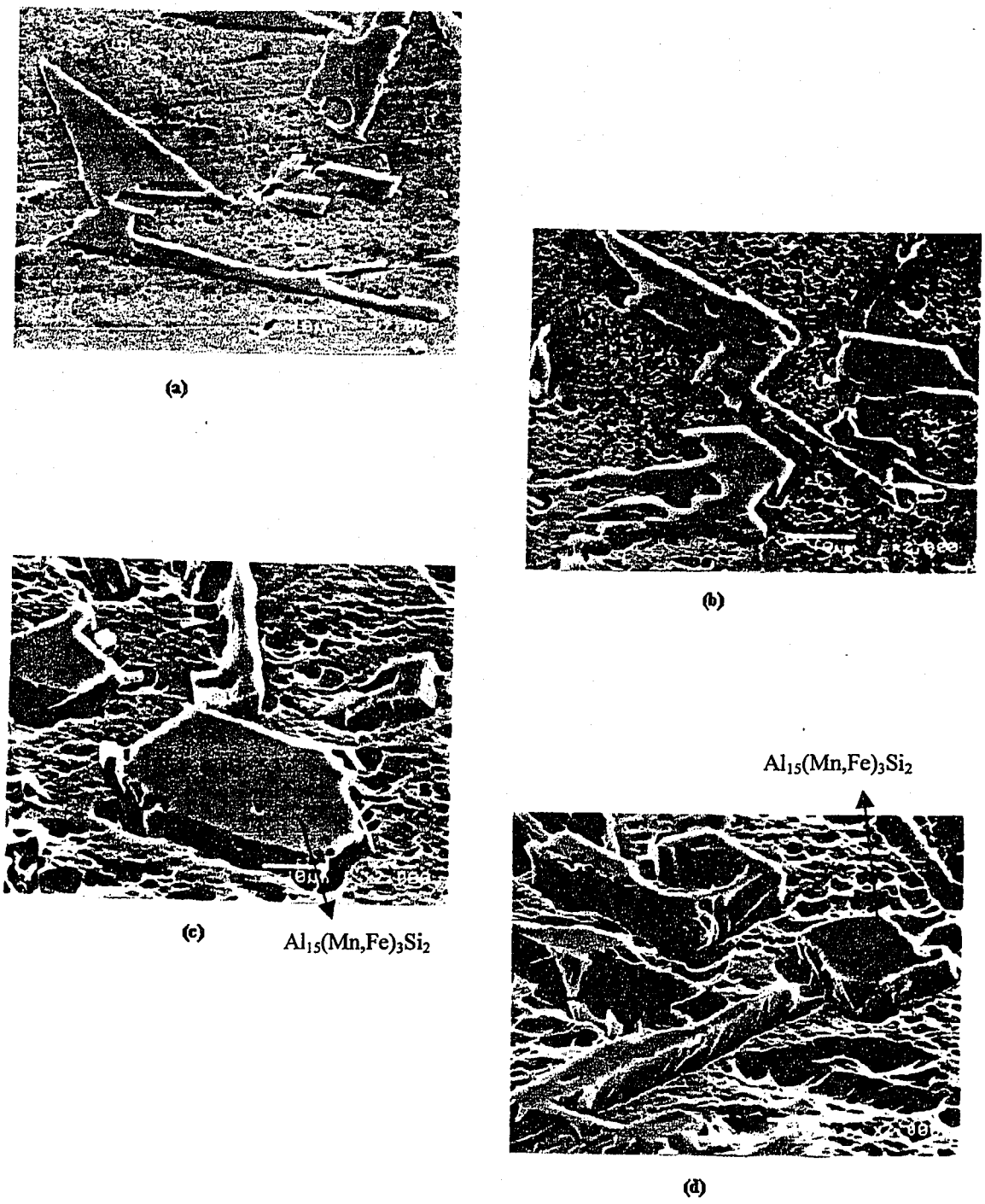

Fig. 6.3. SEM micrographs show the effect of caustic etching time on surface morphology of the two Al-Si alloys: Alloy A, (a) 1 minute (b) 4 minutes (c) 7 minutes (d) 9 minutes

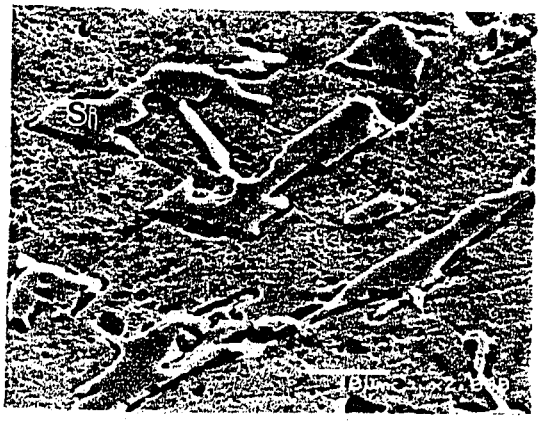

(e)

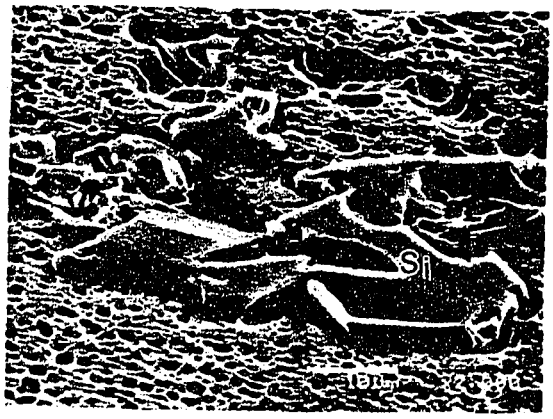

(f)

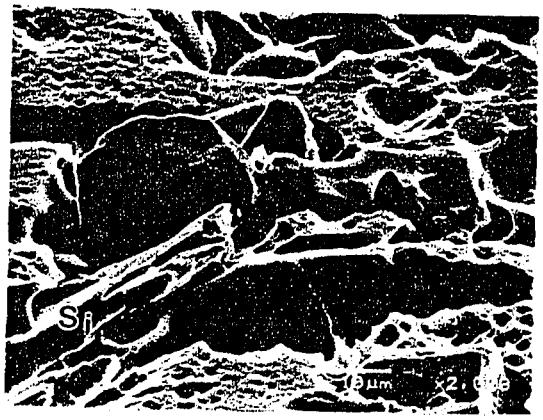

(g)

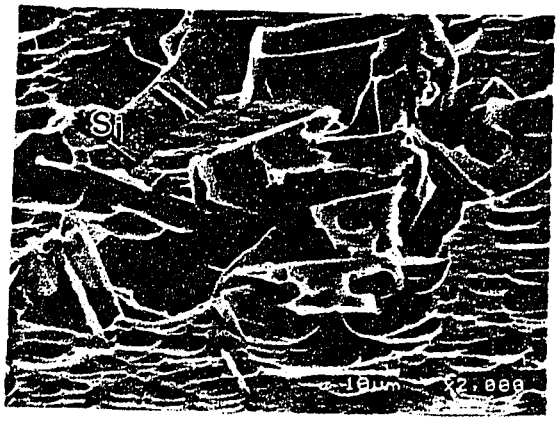

(h)

Fig. 6.3. (continued) SEM micrographs show the effect of caustic etching time on surface morphology of the two Al-Si alloys: Alloy B (e) 1 minute (f) 4 minutes (g) 7 minutes (h) 9 minutes.

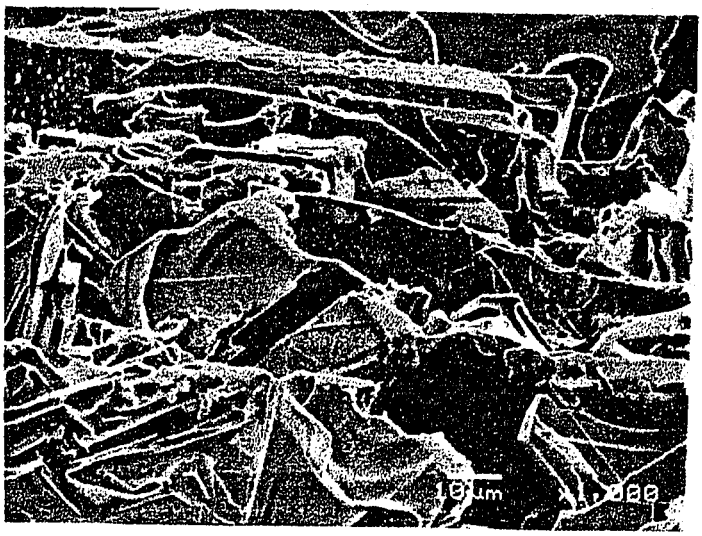

Fig. 6.4. SEM micrograph of the surface morphology of the surface etched by 50%HCl for 0.5 minutes, for alloy B.

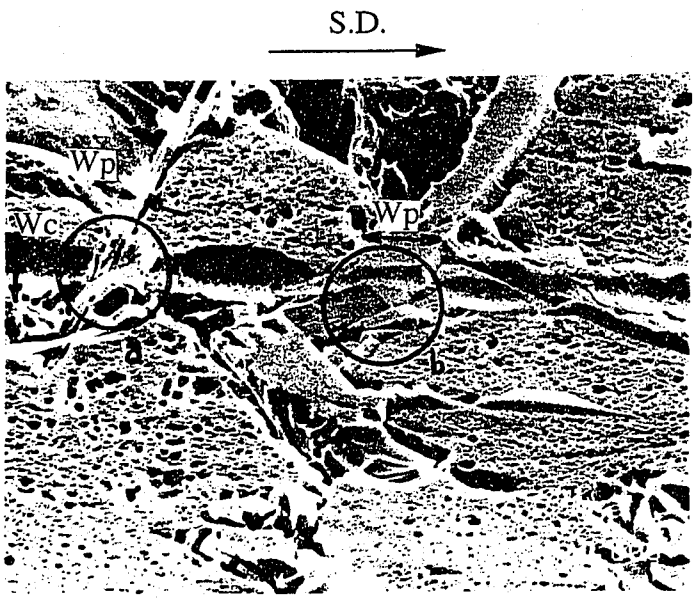

Fig. 6.5. SEM micrograph of the surface of the alloy A after a single pass scratch test. A fractured particle from the root (particle /matrix intersection) is marked as "a", where Wp/Wc= 1/10. When Wp/Wc=1 particle can support the load and resist scratching as in "b".

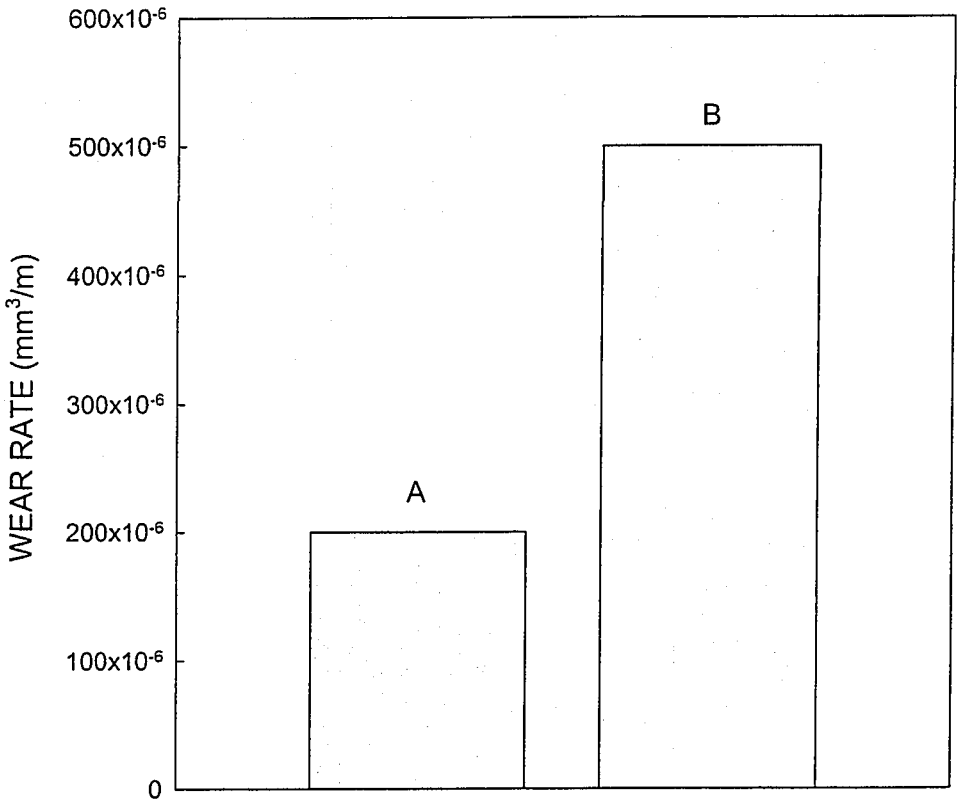

Fig. 6.6. (a) The wear rates of alloys A and B at 5N and 0.5 m/s, when the samples were made as discs and initially etched by 10%NaOH solution for 7 minutes.

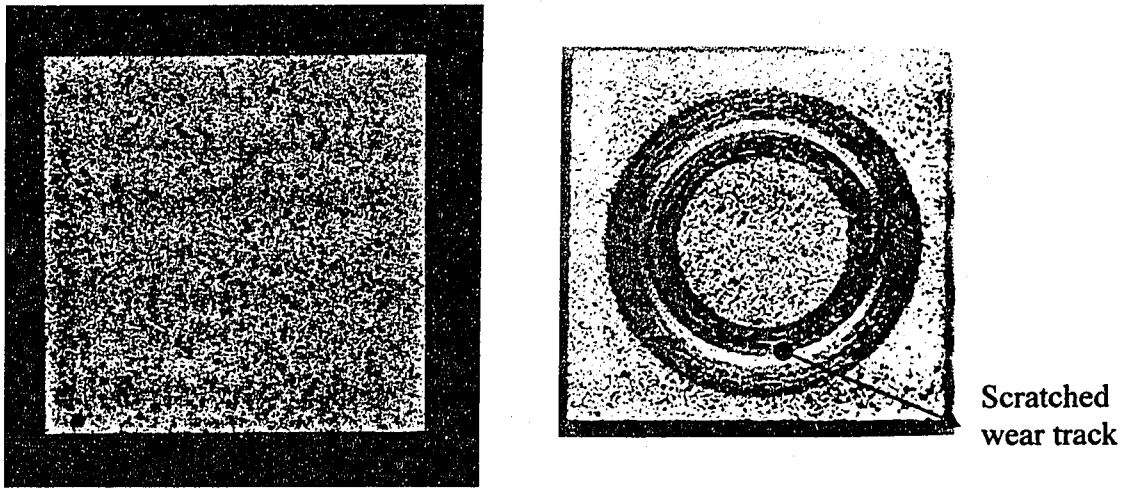

(b) (c)

Fig. 6.6. (b) The unworn sample of alloy B (c) as a result of scuffing the worn surface was scratched and ploughed.

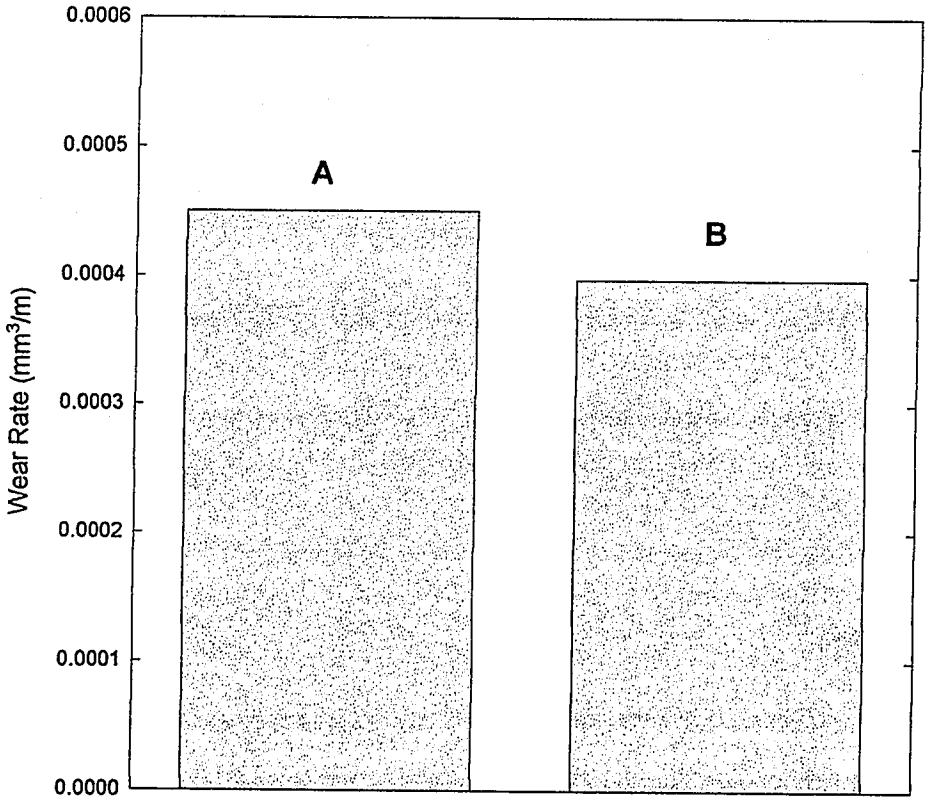

Fig. 6.7. (a) The wear rates of alloys A and B at 5N and 0.5 m/s, where they were tested as the pin and initially etched by 10%NaOH solution for 7 minutes.

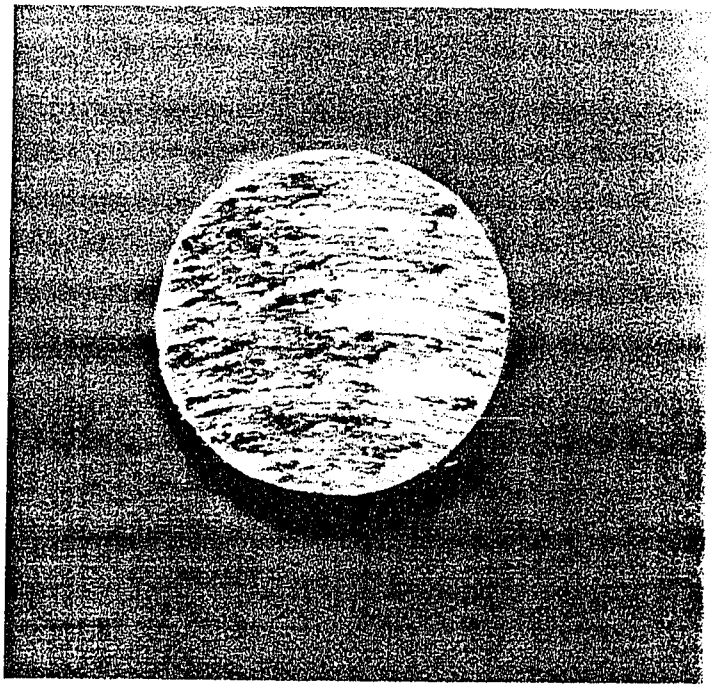

Fig. 6.7. (b) The worn surface of a pin made of alloy A after 5000m sliding distance.

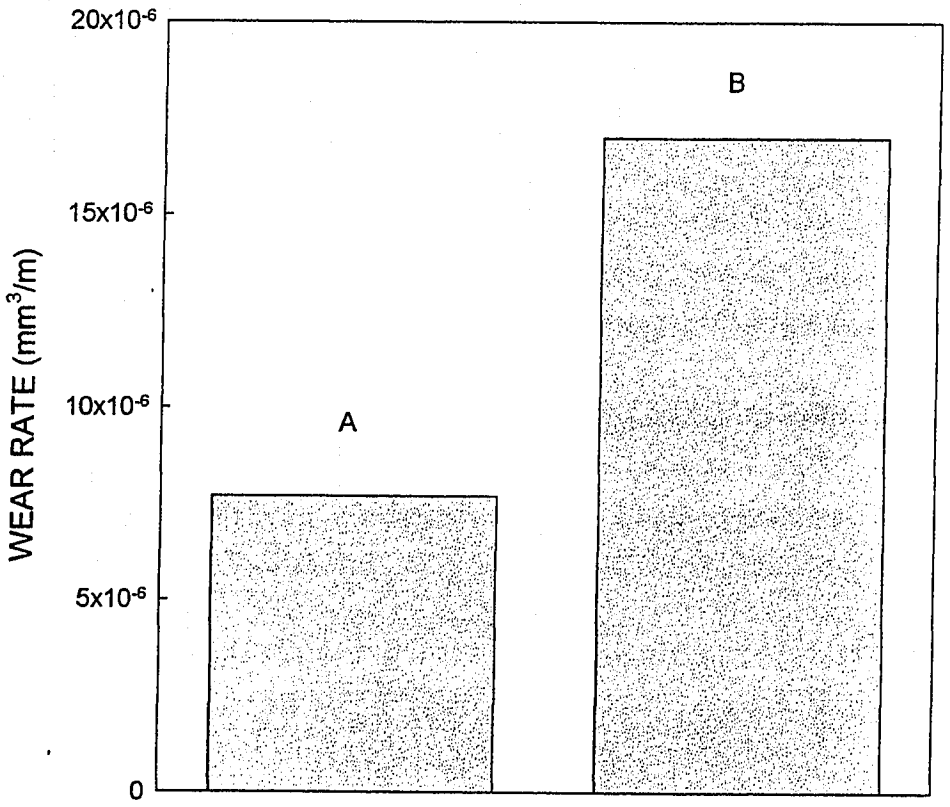

Fig. 6.8. The wear rates of alloys A and B at 5N and 0.5 m/s, where they were initially etched by 50% HCl solution for 0.5 minutes.

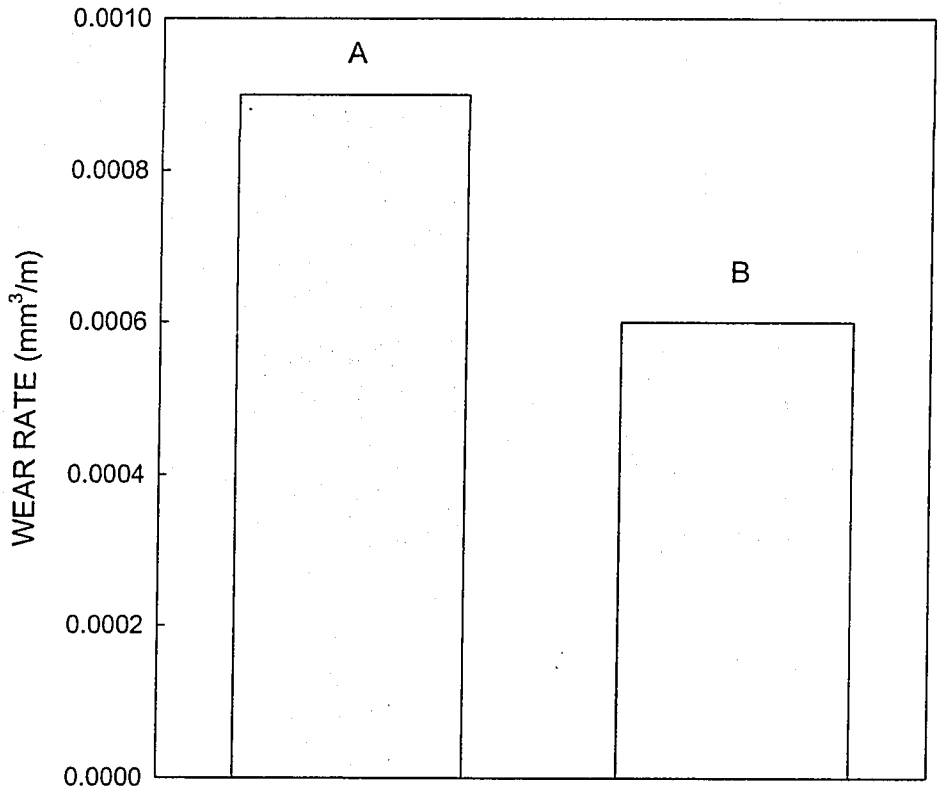

Fig. 6.9. The wear rates of alloys A and B at 5N and 0.5 m/s, where they were initially polished only.

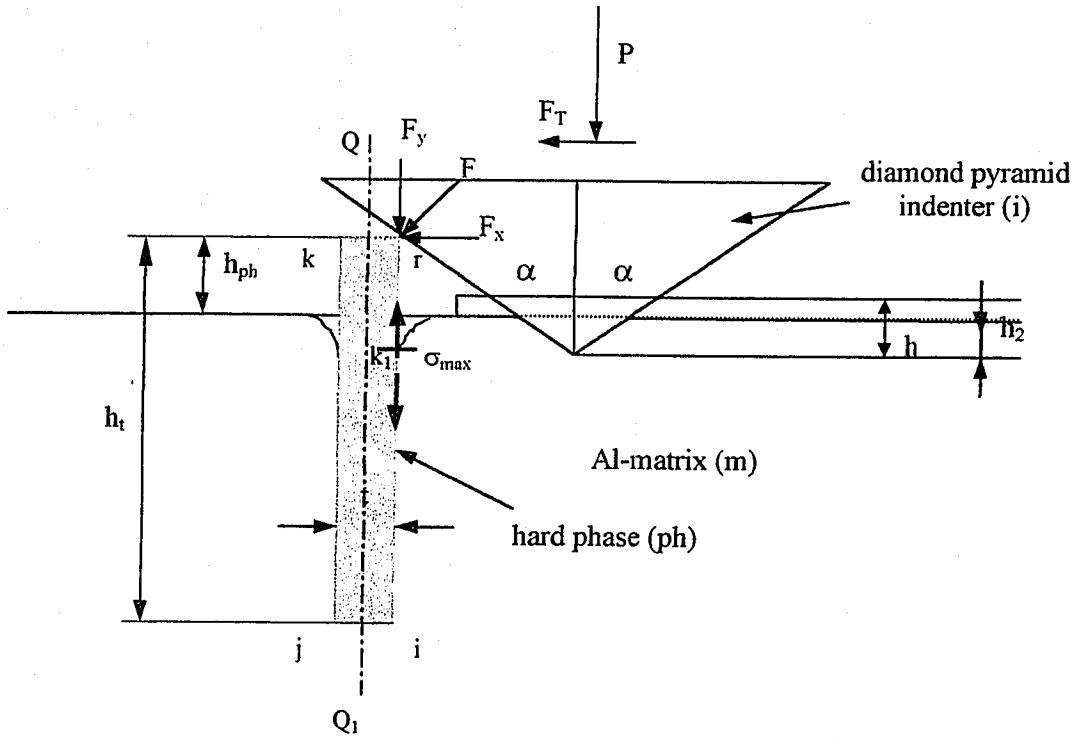

Fig. 6.10. (a) Simplified model of scratch test of an etched surface, consisting of a ductile matrix (m), a hard phase (ph), and a pyramid indenter; (i) with the tip angle 2α, the indenter directly touches the hard phase at r.

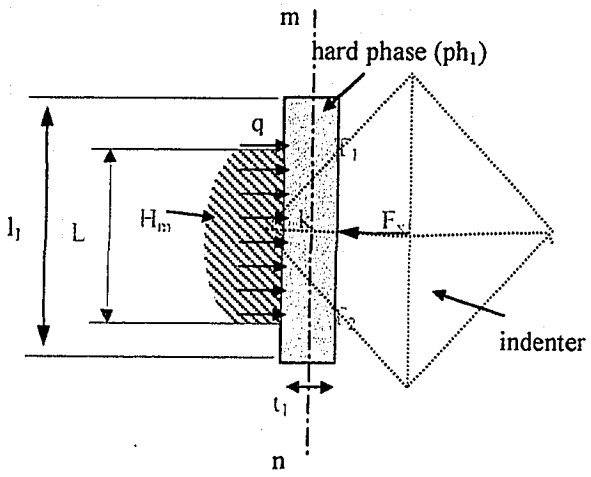

Fig. 6.10. (b) Schematic of the top view of model (6.10.a).

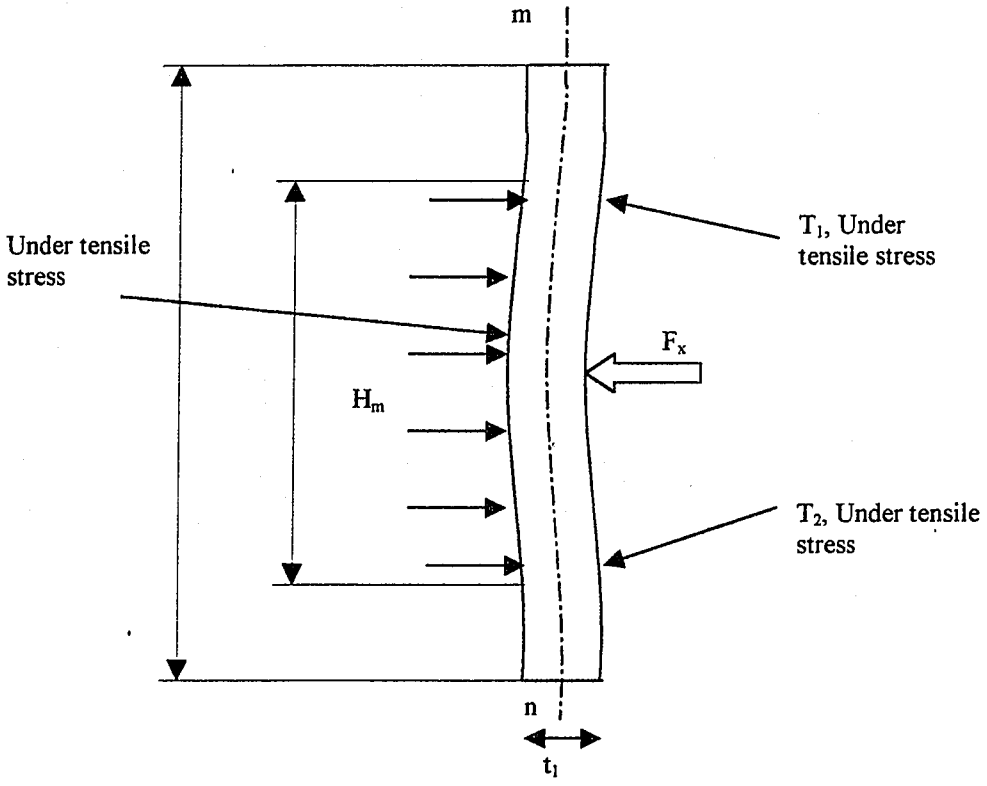

Fig. 6.10. (c) Schematic of locations under tensile stress as a result of bending of a hard phase.

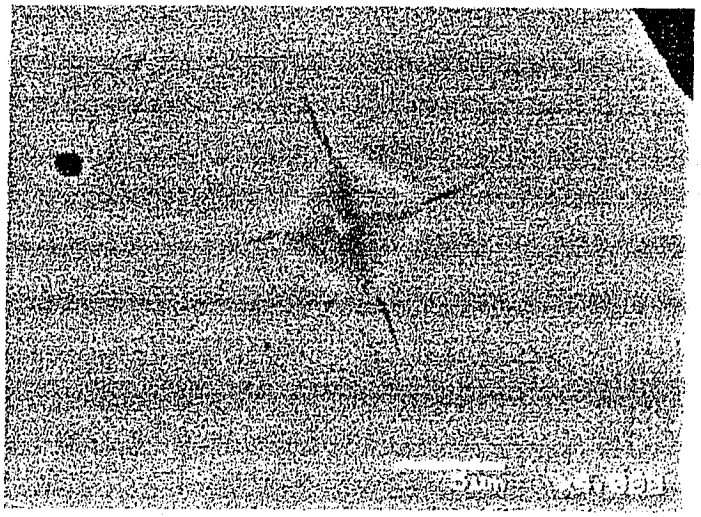

Fig. 6.11. The median cracks along the diagonals of the indentation made by a Vickers indenter at a normal load of 25g on the $(Fe,Mn)_3Al_{15}Si_2$ phase in alloy A.

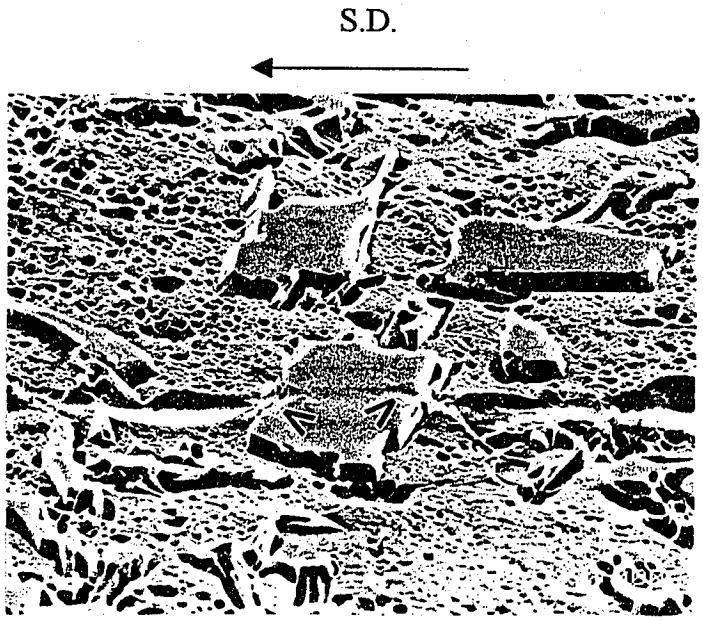

Fig. 6.12. (a) At loads low enough to have only elastic interaction on the top of the hard phase, the damage was limited to the edges (marked by arrows).

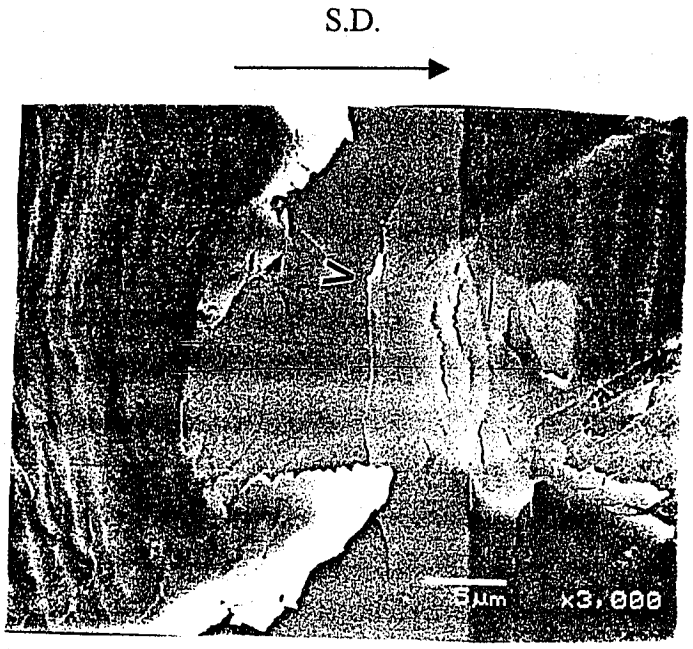

Fig. 6.12. (b) The indenter caused plastic deformation on the top of the hard phase and left several cracks normal to the grooving direction.

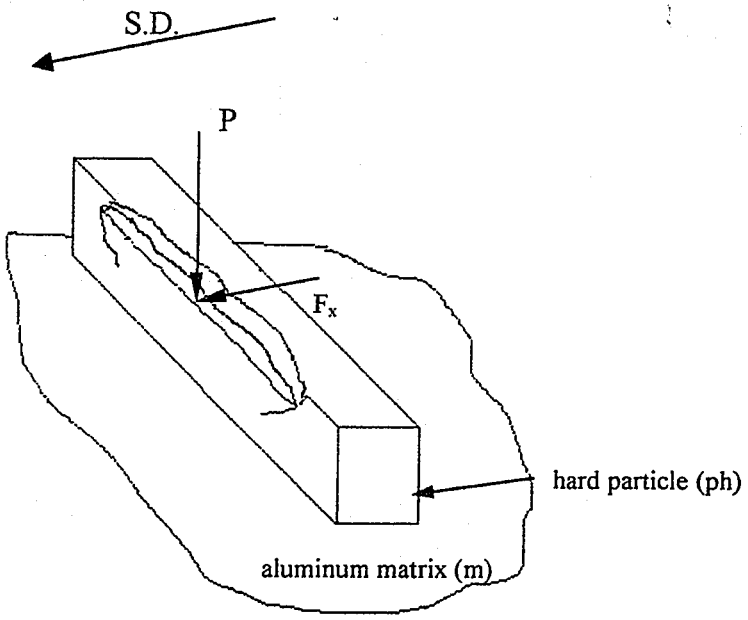

Fig. 6.13. (a) As a result of the sliding contact of a hard asperity on the top of a hard phase, cracks form easier at the trailing edges.

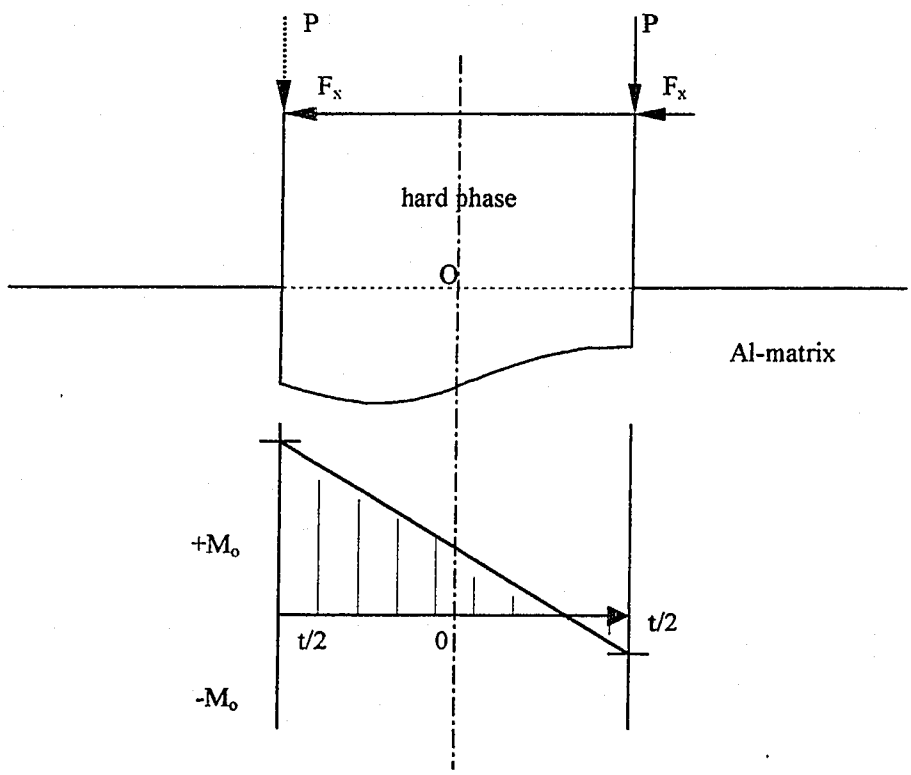

Fig. 6.13. (b) Very high tensile stresses develop at "trailing" edges due to the normal load and the frictional force exerted by the sliding asperities of the counterface when they leave the hard phase.

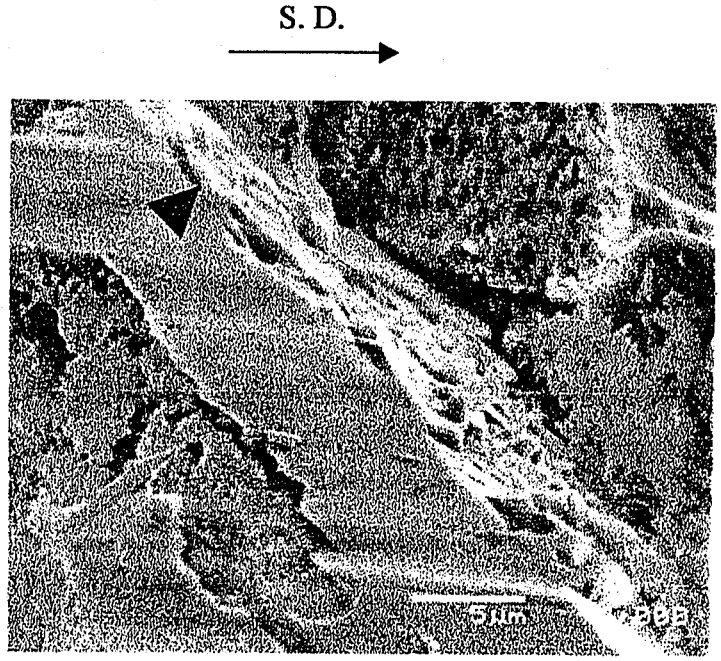

Fig. 6.14. (a) SEM micrograph an $Al_{15}(Fe,Mn)_3Si_2$ particle in alloy A tested at 5N and 0.5 m/s. Fracture of the hard particle at the edge of the particle (marked by arrow) is shown.

Fig. 6.14. (b) The size of debris resulting from in Fig. 6.14.(a) is a fraction of a micron.

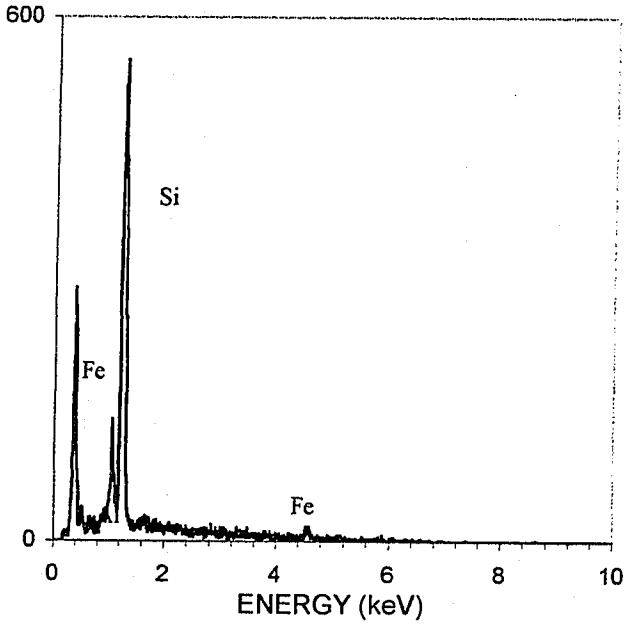

Fig. 6.14. (c) EDS microanalysis of debris in part (b) shows that it is mainly silicon and silicon rich phases.

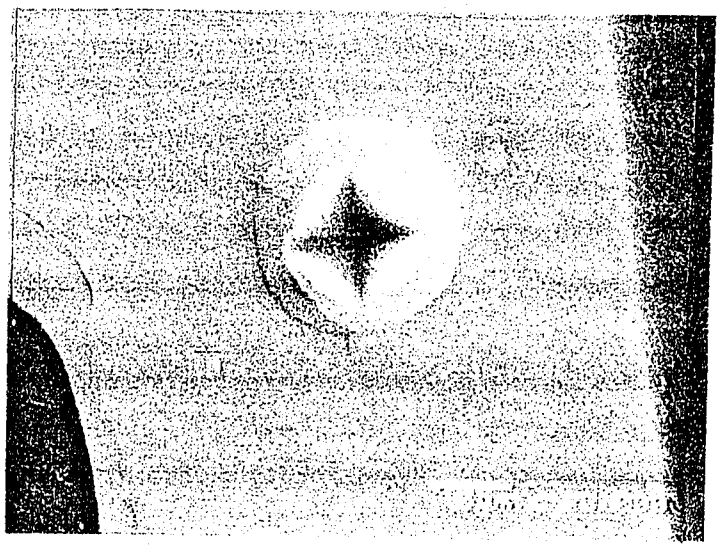

Fig. 6.15. (a) A lateral crack formed as a result of the indentation process (under 25 g normal load) on $Al_{15}(Fe,Mn)_3Si_2$ phase.

Fig. 6.15. (b) Lateral crack caused chipping of a part of a silicon phase at the trailing edge (arrow), during the scratch test process under 5 g normal load.

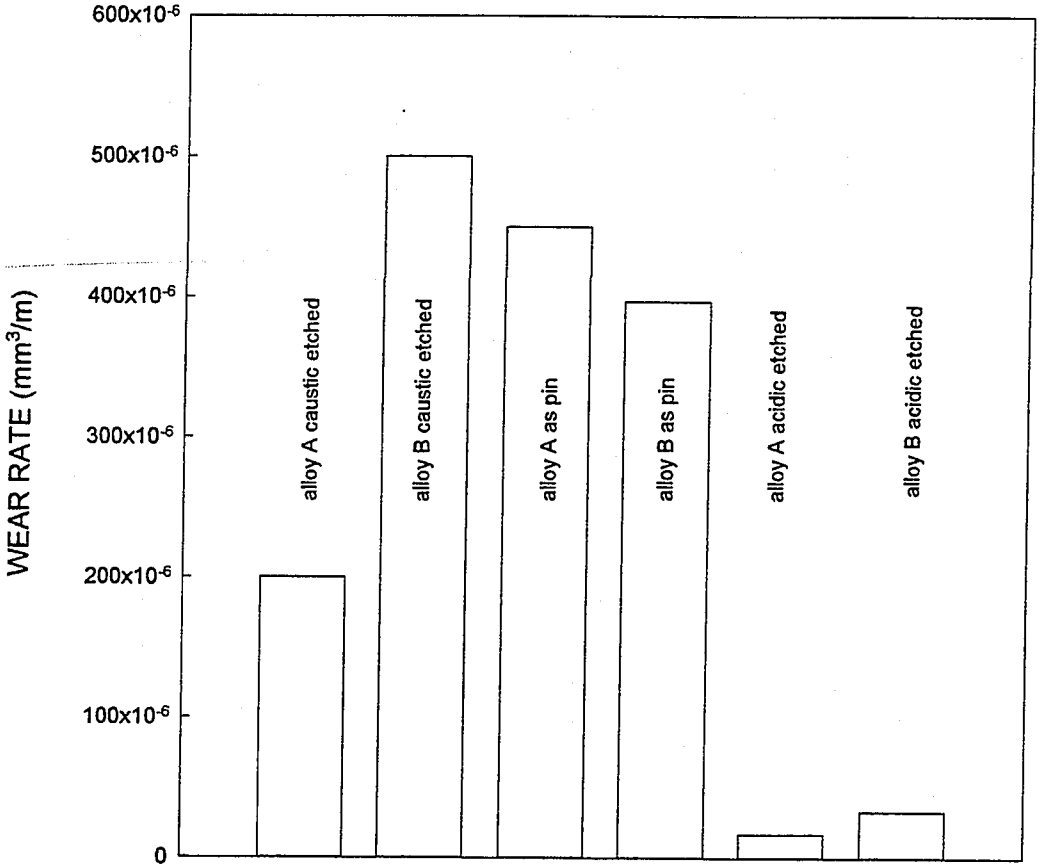

Fig. 6.16. The wear rate of the two Al-Si alloys tested using different configurations of sample and counterface.

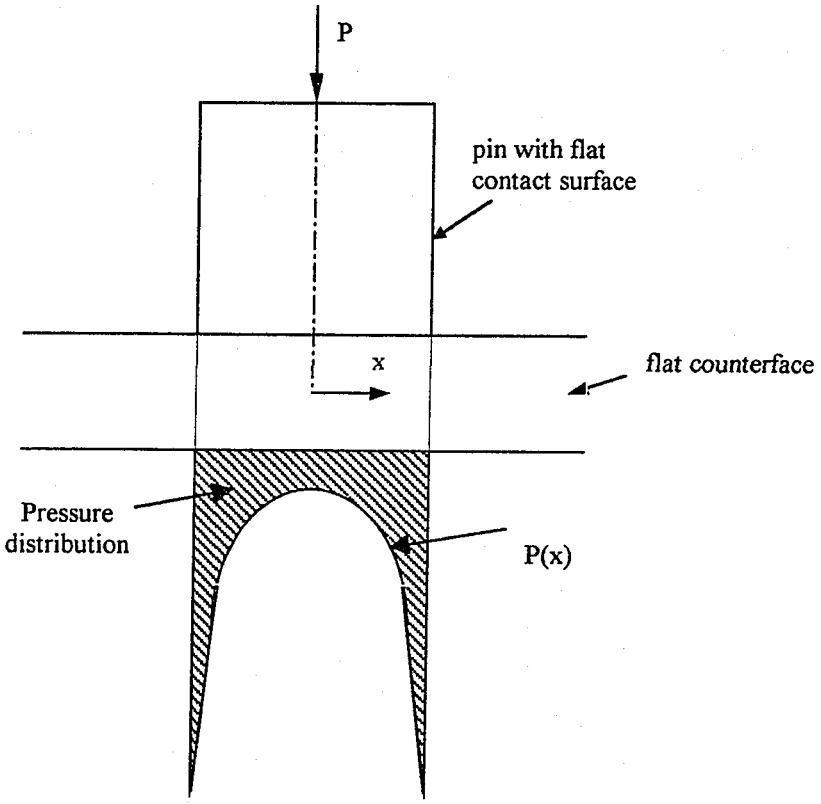

Fig. 6.17. The distribution of pressure at the contact area of a flat pin with a flat surface.

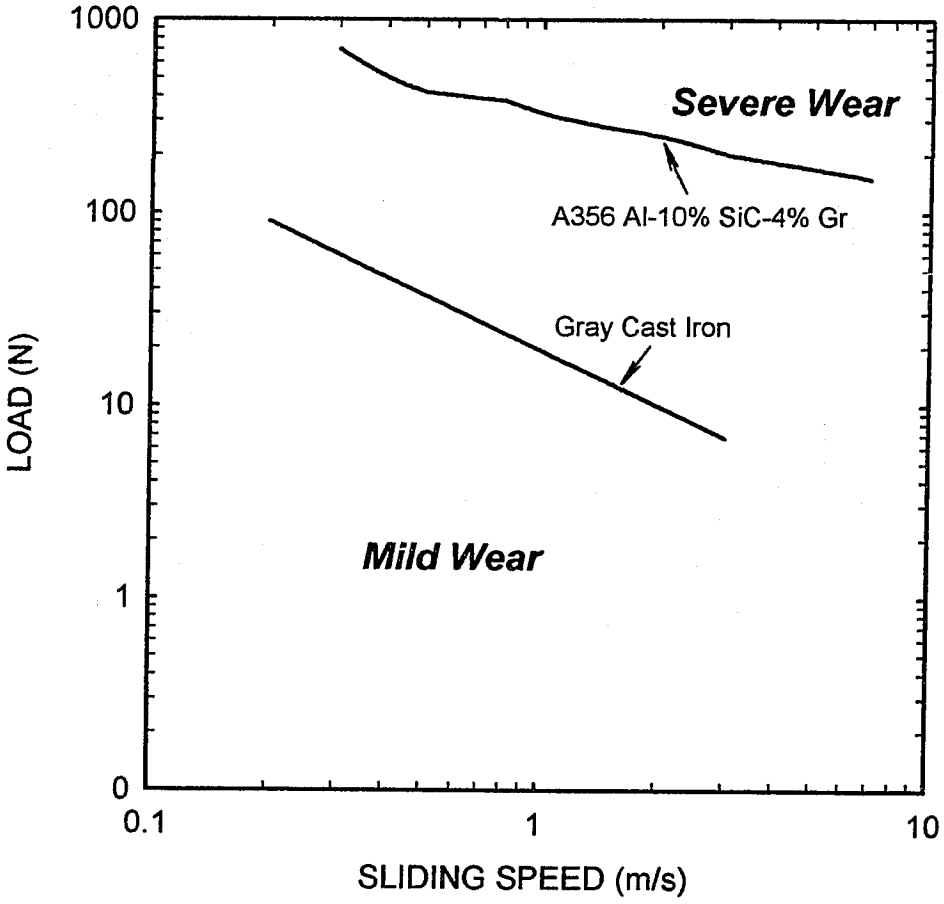

Fig. 7.1. For all sliding speeds, transition to severe wear for A356 Al-10% SiC-4%Gr occurs at loads about 20 times higher than that of cast iron.

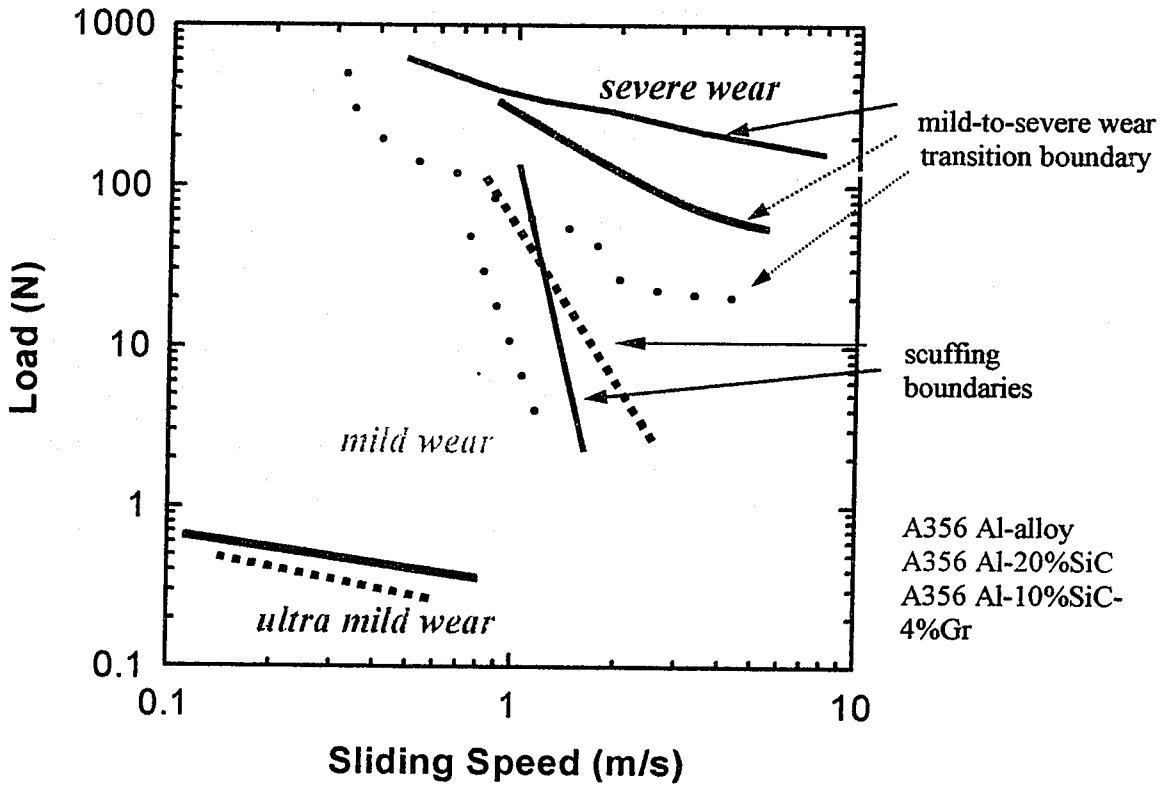

Fig. 7.2. The effect of additives such as hard particle (SiC) and graphite particle to A356 aluminum alloy on the extend of the mild wear regime.

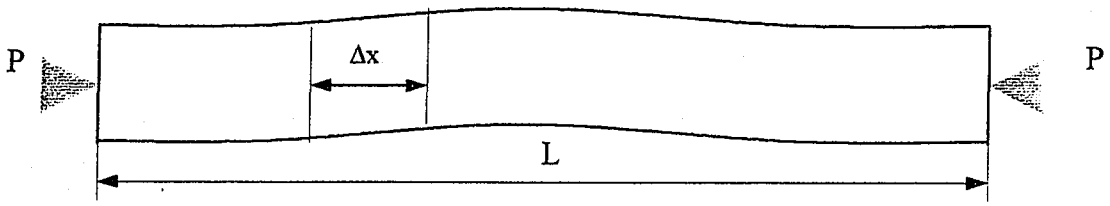

Fig. A.1 Free body diagram of an element of the tribo-layer constrained from both ends.

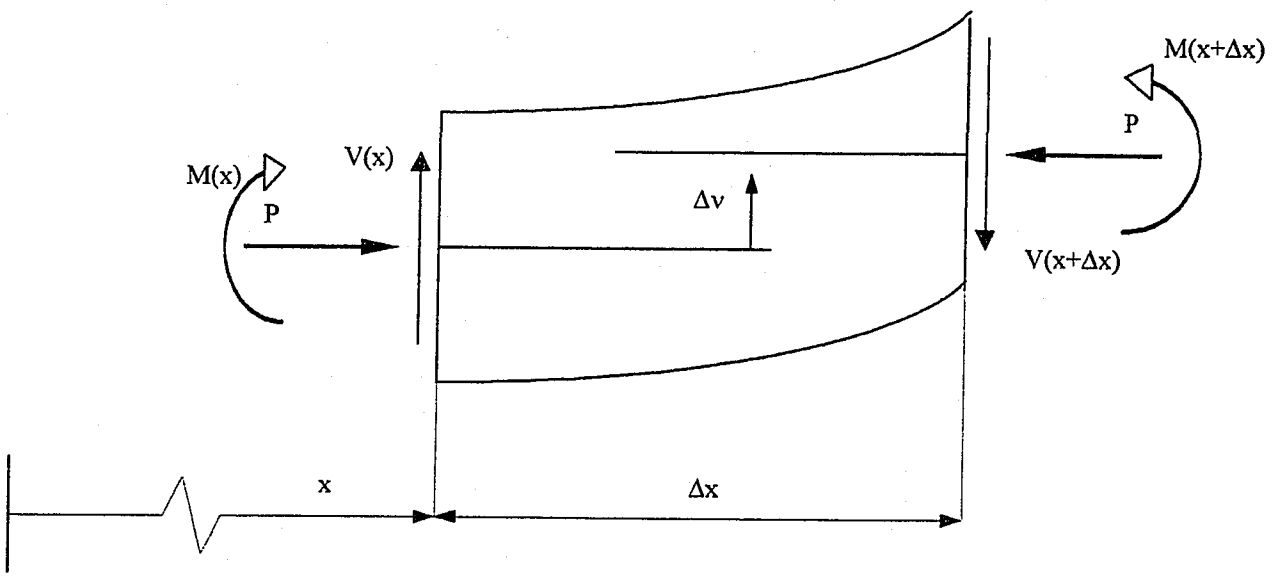

Fig. A.2. Free body diagram of an element of the tribo-layer loaded by a force P equal to the force applied by an asperity in contact with the tribo-layer.

VITA AUCTORIS

The author received his Bachelor of Materials Engineering from Shiraz University, Shiraz, Iran in 1988. He graduated from Isfahan University of Technology, Isfahan, Iran in 1991 with the degree of Master of Science in Materials Engineering. Immediately thereafter, he was accepted as a faculty member into the Department of Materials Engineering of Isfahan University of Technology. In 1999 he began his study toward his PhD degree in Materials Engineering at the University of Windsor and obtained his degree in 2002.